Adaptive and Responsive Design Under Uncertainty for Resource-Constrained Small Satellites

by

Michael G. Fifield

B.S., Georgia Institute of Technology (2015)
S.M., Massachusetts Institute of Technology (2019)

Submitted to the Department of Aeronautics and Astronautics
in partial fulfillment of the requirements for the degree of

Doctor of Science in Aeronautics and Astronautics

at the

MASSACHUSETTS INSTITUTE OF TECHNOLOGY

June 2023

Certified by: David W. Miller
Jerome C. Hunsaker Professor of Aeronautics and Astronautics
Thesis Supervisor

Rebecca A. Masterson
Principal Research Scientist
Thesis Committee Member

Olivier L. de Weck
Apollo Program Professor of Astronautics and Engineering Systems
Thesis Committee Member

Richard P. Welle
Senior Scientist, Aerospace Corporation
Thesis Committee Member

Accepted by: Jonathan P. How
R. C. Maclaurin Professor of Aeronautics and Astronautics
Chair, Graduate Program Committee

Adaptive and Responsive Design Under Uncertainty for Resource-Constrained Small Satellites

by

Michael G. Fifield

Submitted to the Department of Aeronautics and Astronautics
on May 8, 2023, in partial fulfillment of the
requirements for the degree of
Doctor of Science in Aeronautics and Astronautics

Abstract

The space environment that satellites face is uncertain and challenging for survival and operation. Traditionally, satellite design methods mitigate the effects of uncertainty through the use of ample margin. However, robust designs often sacrifice significant nominal performance in exchange for this reduced sensitivity to uncertainty. Small satellites in particular are limited in size, weight, and power (SWaP) and do not have the luxury of resources for ample design margin. They can ill-afford the performance sacrifice of robust design. As SmallSats continue to decrease in size - even down to the hundreds of grams - the need grows for design techniques that offer resilience under uncertainty without the inevitable sacrifice of performance that comes with robust design.

In this thesis, a methodology is presented to mitigate the effects of uncertainty in the space environment with the ability to adapt the satellite's behavior during operation. Compensation for uncertainty on-orbit allows for dynamic allocation of margin on an as-needed basis, reducing the performance loss while improving the ability to maintain operation. The methodology covers two phases. First, design prior to operation enables provisioning of resources to plan for and provide the capability for passive and active dynamic mitigation of *predicted* uncertainty. Second, reprogramming of dynamic behavior in operation allows for optimal mitigation *actual* uncertainty. The resultant designs balance improved resilience in the face of uncertainty with minimal overdesign and sacrifice of performance.

The methodology is applied to a novel SmallSat concept, WaferSat - a SWaP-constrained satellite etched on a 300 g silicon wafer using microelectromechanical systems (MEMS) production. Optimization of active and passive dynamic compensation is utilized to mitigate effects of thermal uncertainty with limited sacrifice of payload power. Multiple design families - with the same available payload power (isoper-

forming) and confidence of operating temperature constraint satisfaction (isofeasible) are identified utilizing different combinations of responsive and adaptive mitigation techniques.

Application of the methodology is expanded to a second system, DiskSat, a similar larger, more thermally complex system. A detailed comparison of the continuum between responsiveness and adaptability is made, demonstrating the Pareto-set of isoperforming and isofeasible designs between two mitigation methods. Design for the balance of active and passive uncertainty mitigation over multiple constraints is explored, highlighting implementation considerations.

Thesis Supervisor: David W. Miller
Title: Jerome C. Hunsaker Professor of Aeronautics and Astronautics

Acknowledgments

There are many who I would like to thank, and try as I might, I cannot truly find the words. First, I would like to thank my advisor, Prof. David Miller for his guidance and mentorship. Dave, you have truly been with me every step of the way, through thick and thin. When I faltered, you reminded me why it is the 'man in the arena' who counts. I have learned much from you and I will miss our weekly research meetings; I guess I will just have to bug you in your office at JPL.

I would also like to thank my committee members, Dr. Rebecca Masterson, Prof. Olivier de Weck, and Dr. Richard Welle. Without the insights and acumen of the committee, this work would not have been possible. Becky, you have provided so much support as a co-advisor and PI. Thank you for always being there. Thank you also to my thesis readers, Dr. Brian Cohen and Dr. Michel Ingham.

I am extremely grateful for generous and continuous funding through MIT Lincoln Laboratory and the MIT AeroAstro Department. I would like to especially thank the many members of the LL WaferSat team with whom I have worked over the years.

To my fellow grad students of the Space Systems Lab, thanks. Alex, I will miss all of the left and right-handed loops. Evan and Alex, here's to the SSL Swim Team and SpinAp testing. Oliver and Keenan, we have all left quite the mark on the Rumpus Room (though I am not sure where all of the ducks came from). Charlotte, Tonio, Will, Hailee, Rosemary, and Daniel you have all been great labmates and I will miss Labsgiving. To Mike and the AeroAstro IM hockey team, we will always be 2021-2022 champs and heroes of D-league.

Finally, thank you Mom, Dad, and Jennifer for all of your love and support.

Contents

1 Introduction **31**

1.1 WaferSat: Integrated Satellites-on-a-Chip 32

1.1.1 SmallSat Trends 32

1.1.2 MEMS Integration 33

1.2 High Aspect Ratio: A Novel Satellite Design Regime 34

1.2.1 Scaling of Surface Area, Volume, and Mass 35

1.2.2 Subsystem Design Implications of $\mathcal{AR}$ 36

1.3 Margin for Robustness or Lack Thereof 40

1.4 SmallSats, the Space Environment, & Design Difficulty 42

1.5 Research Statement & Thesis Structure 43

2 Literature Review **45**

2.1 Pico Satellite Design 45

2.1.1 History of Chip-Scale Satellites 46

2.1.2 The Thermal-Power Challenge of Small, High $\mathcal{R}$ Satellites . . 48

2.2 Coupled Systems and Sensitivity 50

2.2.1 Sensitivity Analysis 50

2.2.2 Design Decision Rules 51

2.3 Robust Optimization 52

2.3.1 Robust Solutions Sacrifice Nominal Performance 52

2.3.2 Adaptive Approaches to Robustness 55

2.3.3 Spacecraft Thermal Adaptive Approaches 57

2.4 Technical Gap and Research Objective 59

3 Design for Performance, Robustness, Responsiveness, & Adaptability 65

3.1 Nomenclature & Relationships 65

3.1.1 Defining Variable Sets 66

3.1.2 Processing Variables Sets 67

3.1.3 Outputs & Resultant Qualities 68

3.2 A Simplified WaferSat Example Problem 69

3.2.1 Design Variables & Parameters 69

3.2.2 Power Maximization & Thermal Constraints 71

3.3 Nominal Optimization 73

3.3.1 Optimization for a Certain World 73

3.3.2 Active Constraint Set 75

3.3.3 WaferSat Example: Nominal Optimal Design is not Robust . . 77

3.4 Static Robust Optimization 81

3.4.1 Static Tailoring for Static Robustness 81

3.4.2 WaferSat Example: Optimizing for Static Robustness 84

3.4.3 Nominal Performance & Static Robustness: Pick One 87

3.5 Responsive Robust Optimization 88

3.5.1 Responsive Tailoring 88

3.5.2 Phase Change Materials: Responsive Heat Storage 90

3.5.3 WaferSat Example: Application of PCM 90

3.6 Adaptive Optimization 94

3.6.1 Design for Adaptability & Adapting to Uncertainty 94

3.6.2 WaferSat Example: Adaptive Electrochromics 96

3.7 The Costs of Static Robustness, Responsive Robustness, Adaptability 102

3.8 Summary 103

4 WaferSat **105**

4.1 Problem Definition 105

4.1.1 Parameters & Static Design Variables 106

4.1.2 Constrained Optimization 107

4.1.3 Thermal & Power Modeling 109

4.2 Modeling Parametric Uncertainty 114

4.2.1 Local Albedo 114

4.2.2 Earth IR 116

4.2.3 High $\mathcal{R}$ Sensitivity to Local Uncertainty 118

4.3 Nominal & Robust Optimization 119

4.3.1 The Nominal Optimal Design is Not Robust 120

4.3.2 The Robust Design is Not Nominal Optimal 122

4.4 Responsive & Adaptive Mitigations 125

4.4.1 Phase Change Materials 126

4.4.2 Thermal View Factor Control 129

4.4.3 Electrochromics 131

4.5 Comparing Isoperforming and Isofeasible Solutions 134

4.5.1 Design 1: PCM-Dominant 136

4.5.2 Design 2: Electrochromics-Dominant 139

4.5.3 Design 3: Thermal View Factor-Dominant 143

4.5.4 Summarizing Designs 147

4.6 Modeled Uncertainty Error 149

5 DiskSat **153**

5.1 $\mathcal{A}R$ Scaling Revisited 154

5.2 Defining the Problem 155

5.2.1 Multi-Node Thermal Modeling: Axial 1D Gradient 155

5.2.2 New Parameters for DiskSat 156

5.2.3 Internal Facing Electrochromics for Adaptive Heat Flow . . . 157

5.3 Responsive Robustness vs. Adaptability 159

5.3.1 A continuum from most adaptive to most responsive 160

5.3.2 Balancing Adaptive Authority 163

5.4 Seasonal robustness: variation in β angle 165

5.5 Analysis of Radial Gradients 169

6 Conclusion and Future Work **173**

6.1 Thesis Contributions 174

6.2 Future Work 176

A Thermal Model Validation Cases **179**

A.1 Modeling Thermally Isolated Solar Arrays 179

A.2 Modeling a Silicon Wafer in LEO 182

B A Deep Space SmallSat **185**

B.1 $\mathscr{R}$ Scaling Reprise 186

B.1.1 Thermal Optimality Further from the Sun 186

B.1.2 Power Optimality Further from the Sun 189

B.2 Thermally Adapting in Deep Space 191

B.2.1 Thermal Variability on a Schedule: Inner vs. Outer Cruise . . 191

B.2.2 Thermal Spatial Zones 193

B.2.3 Power Modes and Mission Sequencing 195

List of Figures

1-1 MEMS-produced, µm-scale, mechanical silicon gear mechanism by Sandia National Laboratories [7] 33

1-2 Comparison of estimated cost relative to effective aperture diameter of various femtosat swarm patterns [12] 34

1-3 Surface area vs. volume scaling for specified shapes and aspect ratios 37

1-4 Estimated temperature ranges over one orbit for various aspect ratios of blank silicon wafer in 400 km orbit, nadir-facing orientation 38

1-5 Comparison of orbit average power vs. bus mass trends for disk form factor and traditional s/c [14] 39

1-6 Two examples of Pareto fronts with uncertain metrics, expressed as a min/max range (left) and bounding boxes (right). 41

2-1 A MEMS PicoSatellite being loaded into a spring-loaded deployer on the OPAL spacecraft [29] 47

2-2 Plot of optimal communications antenna decisions in various areas of design space [43] 52

2-3 1D example comparing a robust but non-nominally optimal solution (A) and a nominally optimal but non robust solution (B) [46] 53

3-1 A zero β angle, 400 km altitude, circular orbit. WaferSat is depicted at a true anomaly, ν referenced to the closest position to the Sun. . . 70

3-2 Simplified representation of WaferSat surfaces 71

3-3 Nominal Optimization; optimizer does not consider uncertain outcomes. After the optimization process is complete, the optimized design may be subjected to models of uncertainty to evaluate performance under uncertainty to reveal a lack of robustness. 75

3-4 Quasi-steady state single-node temperatures of nominal optimal design with no uncertainty. Note that the temperature constraints are met at equality. 77

3-5 One performance SoTW with no uncertainty 78

3-6 The effective emissivity, ε_{Neff} of the nadir-facing surface resulting from Gaussian uncertainty in static coatings 79

3-7 Distribution of nominal power performance outcomes under no uncertainty (black), and under modeled uncertainty (blue). Performance varies widely and degrades with the addition of uncertainty. 80

3-8 Feasibility results over the distribution of outcomes are sent back to the optimizer as new constraints, guiding the optimizer towards designs that are performance optimal *with* sufficient static margin 82

3-9 Static Robust design with static margin against the active temperature constraints in the zero uncertainty scenario 84

3-10 Distribution of nominal outcomes and statically robust outcomes under modeled uncertainty 87

3-11 Responsive robust single-node temperatures in the zero uncertainty case. Isotemperature regions during cooling and heating through the phase transition point lengthen the effective thermal time constants. . 92

3-12 Liquid mass ratio during phase transition during cooling at dusk . . . 93

3-13 A histogram of responsive robust power performance outcomes under the modeled uncertainty. 94

3-14 Two-stage optimization: adaptive tailoring of dynamic variables to govern and constrain adaptive behavior, tuning optimization to determine optimal tuned response to uncertain SoTW 95

3-15 Diagram of nadir surface and thermal properties 97

3-16 A comparison of the unmitigated and electrochromic adaptive distributions of ε_{Neff} 99

3-17 A comparison of emissivity outcomes for the unmitigated case in blue and inactive electrochromics in gray. The inactive electrochromics are held at a value of 0.5 for all time. 100

3-18 Distribution of adaptive optimal solution using electrochromic-mitigated ε_{Neff} 101

3-19 A comparison of histograms of performance outcomes under uncertainty for each individual mitigation method 103

4-1 Diagram of disk to sphere for Equation 4.9 (not to scale for Wafer-Earth system) 112

4-2 Comparison of view of Earth albedo from LEO spacecraft. Left: realistic local albedo distributions. Right: effective average constant [94] . 115

4-3 Distribution of local albedo using measured data from NASA CERES project 116

4-4 Estimated distribution of local Earth black body temperatures encountered by a satellite in LEO based on measured data from NOAA [96] and CERES projects [94] 117

4-5 Scaled comparison of high and low $\mathcal{R}$ wafers 118

4-6 Mean temperatures (solid lines) over one orbit with 2σ variance (dashed lines) for a high $\mathcal{R}$ and low $\mathcal{R}$ blank Si wafer under local albedo and Earth IR uncertainty. 119

4-7 Nominal Optimal Solution, zero margin 120

4-8 Nominal Optimal Solution under modeled uncertainty 121

4-9 Standard rate of variance convergence error with Monte Carlo sample size. Population size $N = 10^4$ correlates to $< 2\%$ variance error. . . . 123

4-10 Nominal Optimal Solution under modeled uncertainty 124

4-11 Silicon Nitride Paraffin Microcapsules [99] 127

4-12 WaferSat LVLH roll, thermal view factors, and net heat flows at $\theta = 0$ 130

4-13 Net heat flows as function of LVLH roll angle and True Anomaly, $\beta = 0$ 131

4-14 Measurements of EclipseVED electrochromic emissivity as function of wavelength in: low emissive (blue) and high emissive (red) states [102] 132

4-15 Planck's curve for the bounding temperature requirements with Wien's Law peak irradiance wavelengths. 133

4-16 WaferSat surface design with allocation of nadir area to electrochromics (purple). 135

4-17 Design 1 distribution of outcomes in T_{max} and T_{max} constraint space with GMM 2σ error ellipse and NLPCA first principal axis of variance 138

4-18 Design 2 distribution of outcomes in temperature constraint space. . . 140

4-19 Design 2 PCM partial freeze scenario. 141

4-20 Temperature and electrochromics response for the adaptive mitigation of a selected uncertain outcome. 142

4-21 Design 3 distribution of outcomes in temperature constraint space. . . 144

4-22 Temperature and LVLH roll response for the adaptive mitigation of a selected uncertain outcome. 145

4-23 A comparison of the relative level of utilization of the responsive and adaptive mitigations for three isoperforming and isofeasible designs . 147

4-24 A comparison of temperature constraint spaces for designs 1, 2, 3 . . 148

4-25 Temperature extreme variance of statically tailored robust solution for 3 levels of uncertainty model variance. Feasbility decreases quickly as uncertainty model variance increases. 150

4-26 Temperature extreme variance of Design 1: PCM-dominant for 3 levels of uncertainty model variance. Degradation of feasibility occurs at slower rate than in static robust design. 151

5-1 A 1 meter diameter DiskSat next to a 1.5 U CubeSat. The internals of a CubeSat are contained in a module in the center of the disk. [108] 153

5-2 Thermal quasi-steady state of 3.5 kg DiskSat compared to thermal equilibrium. Modeled as a single-node in 400 km altitude circular orbit, β angle of 0. 155

5-3 Zenith, mid, and nadir nodes. All internal-facing surfaces are coated with electrochromic surface. Arrows represent the following parallel heat paths: high conductive coupling between exterior facesheets (black), low conductive coupling from exterior facesheets to mid-node (green), and internal radiative heat transfer between exterior facesheets and mid-node (purple). 156

5-4 Internal face electrochromic regulation of mid-node temperatures through adaption of radiative heat flows. 159

5-5 Continuum from most adaptive to fully responsive robust. Tailorable excess responsive robust margin cases: (a) cold-limited 2-σ feasible; (b) balanced 2-σ+ feasible; (c) hot-limited 2-σ feasible 161

5-6 Comparison of tailored margin in three cases: minimum temperature constraint, maximum temperature constraint, balanced. 162

5-7 Retailoring of PCM temperature of fusion to balance required electrochromic range 164

5-8 Variation of power and mid-node extreme temperatures with β angle 166

5-9 Power generation for various β angles 168

5-10 Surface of DiskSat with non-homogeneous thermo-optical surfaces. Temperature is evaluated at the annular nodes. 170

5-11 Temperatures of facesheets: DiskSat solar array-covered edge node (green), DiskSat center area directly above avionics (blue). 172

A-1 Visualization of orbit from [37], shown from two viewing angles. . . . 180

A-2 A comparison of the modeled results against the literature results. Models are in close agreement. 181

A-3 Comparison of thesis MATLAB model to Thermal Desktop and results of 4 inch Si wafer in LEO from [39] 183

A-4 Angles defining satellite tangency and start of eclipse from [39] 183

B-1 Steady State temperatures at 9.5 AU vs. disk radius for a fixed volume system. 187

B-2 Surface areas: total surface area and relative contributions of face areas and side wall area 188

B-3 Heat Flows vs. disk radius. Solid line represents absorbed heats, dashed lines represent radiation. 189

B-4 Mean electrical power contours and steady state temperatures for scaling of disk with various solar array fill factors 190

B-5 Pareto fronts of electrical power capability vs. steady state temperature for several disk radii 191

B-6 1-meter radius disk steady state temperature extremes at perihelion and aphelion with electrochromic and view factor adaptability 193

B-7 Bus steady state temperature for given internal power dissipation and contours of percent internal heat capture rate. 194

B-8 Propellant tank steady state temperature for local heater power with contours of tank size (propellant mass in kg) 195

List of Tables

2.1 Summary of identified research gaps and corresponding thesis contributions 61

3.1 Nomenclature Relationships 66

3.2 Summary of expected values and probabilities of success 100

4.1 Constant parameters used throughout the WaferSat problem 106

4.2 Set of static design variables, $\mathbf{v}_s$ 107

4.3 General spacecraft subsystem temperature requirements [44, 89] . . . 108

4.4 Incident Heat Source Terms 110

4.5 Summary of heat and radiation subscripts and symbols. The symbol $*$ refers to either any base letter or subscript. 111

4.6 Thermal Radiation Terms 112

4.7 Summary of nominal and robust designs 123

4.8 Summary of PCA properties for Nominal and Static Robust Designs . 125

4.9 PCM dynamic design variables 127

4.10 Summary of key static and dynamic variables of three isoperforming and isofeasible designs. 136

5.1 Constant parameters used throughout the DiskSat problem 157

A.1 Summary of parameters for solar array thermal modeling from [37] . . 180

A.2 Summary of parameters for solar array thermal modeling from [39] . . 182

Nomenclature

Optimization

Bilevel Optimization	Optimization utilizing two loops where one is nested within the other
Constraint Margin	Slackness in an inequality constraint
Design Phase	Time period in which static design variables, a priori design variables, and Tailoring occur.
Dynamic Robustness	Ability of a system to maintain feasibility and performance under uncertainty through variation of dynamic design variables in operation
Fixed Recourse	Adjustment of design variables in operation that follows a predetermined, passive response to uncertainty
Gradient Optimization	Algorithms for optimization that utilize calculation or estimates of the Jacobian to propose continuous solutions.
Heuristic Optimization	Algorithms for optimization that utilize discrete so-

	lution proposals and evaluations. Examples include genetic algorithms, simulated annealing, particle swarm optimization
Isofeasiblity	Refers to the set of designs that each deliver the same statistical guarantee of constraint feasibility over a modeled uncertainty set
Isoperformance	Refers to the set of designs over which a measure of performance is invariant
Nominal Optimal	Designs that provide the best performance under the certain, no uncertainty case only
Operational Phase	Time period in which system is assumed to be in orbit. Dynamic design variable response is fixed; adaptive design variables may be tuned or retuned as needed.
Sequential Optimization	Optimization with two or more loops where each occurs successively. See Tailoring then Tuning.
Static Robustness	Ability of a system to maintain feasibility and performance under uncertainty through margin or insensitivity to sources of uncertainty

Processes

Adaptive Tailoring	Design of the a priori tuning variables that govern the Adaptive Design Variables. See fixed recourse
Dynamic Tailoring	Design of the a priori tuning variables that govern the Dynamic Design Variables. See fixed recourse

Static Tailoring	Design of a set static variables for robustness in either performance or feasibility
Tailoring	A process to adjust design variables in the design phase (pre-operationally) for optimal performance or feasibility
Tailoring then Tuning	Sequentially optimized approach where the first Tailoring loop provides static and dynamic robustness and the second Tuning loop provides adapatability to modeled uncertainty
Tailoring for Tuning	Bilevel optimized approach where the outer Tailoring loop optimizes static and dynamic robustness as well as the a priori tuning variables to govern adaptability. The inner Tuning loop optimizes for the adaptive and dynamic design variables in operation under uncertainty.
Tuning	A process to optimally, actively adjust variables during operation to compensate for the effects of uncertainty

Uncertainty

Adaptability	Ability of a system to maintain feasibility and performance under uncertainty though acitve, dynamic adjustment of system during operation. See Adaptive Design Variables
Robustness	Ability of a system to maintain feasibility and performance under uncertainty. See Static Robustess and Dynamic Robustness

State of the World	A single instantiation of uncertain parameters, drawn from the modeled uncertainty sets

Variables

Adaptive Variable	A variable that can be actively modified as-needed during system operation
Certain Parameter	A design constant with no uncertainty
Dynamic Design Variable	A design variable that must be set before operation and governs either adaptive or response design variables
Responsive Variable	A variable that can be passively adjusts during system operation following a fixed function; not actively managed, see fixed recourse
Static Design Variable	A variable that is selected in the design phase and held constant during system operation
Uncertain Parameter	A design constant with modeled parametric uncertainty

Acronyms

AI&T Assembly, Integration, and Test

CONOPS Concept of Operations

GMM Gaussian Mixture Modeling

LEO Low Earth Orbit

LVLH Local Vertical Local Horizontal

MDO Multi-disciplinary Optimization

MEMS Microelectromechanical Systems

MORDM Many Objective Decision Making

PCA Principal Components Analysis

PCB Printed Circuit Board

PCM Phase Change Material

RHU Radioisotope Heater Unit

SA Simulated Annealing

SoTW State of the World

SWaP Size, Weight, and Power

SWaP-C Size, Weight, and Power, and Cost

TCS Thermal Control System

Symbols

α	Visible light wavelength absorptivity and emissivity; note that for a common wavelength, λ: $\alpha_\lambda = \varepsilon_\lambda$
ε	Infrared wavelength emissivity and absorptivity; note that for a common wavelength, λ: $\alpha_\lambda = \varepsilon_\lambda$
γ	Attitude angle from Wafer top side normal to Earth-Sun vector
σ	Steffan-Boltzmann constant
β_{SA}	Solar array physical fill factor
$(\cdot)_{1-2}$	Denotes radiation from surface/body 1 to surface/body 2
$(\cdot)_{B-E}$	Denotes s/c nominal nadir surface to Earth direction
$(\cdot)_{B-S}$	Denotes s/c nominal nadir surface to sun direction
$(\cdot)_D$	Denotes DiskSat general large surface area-related term
$(\cdot)_E$	Denotes Earth-related term
$(\cdot)_{SA}$	Denotes zenith solar array surface-related term

$(\cdot)_{SN}$	Denotes nadir solar array surface-related term
$(\cdot)_{T-E}$	Denotes s/c nominal zenith surface to Earth direction
$(\cdot)_{T-S}$	Denotes s/c nominal zenith surface to sun direction
$(\cdot)_n$	Denotes nadir-related term
$(\cdot)_s$	Denotes free space-related term
$(\cdot)_{sol}$	Denotes sun-related term
$(\cdot)_w$	Denotes side wall surface of wafer or disk term
$(\cdot)_{waf}$	Denotes WaferSat general large surface area-related term
$(\cdot)_z$	Denotes zenith-related term
A_E	Mean Earth albedo
E_{sol}	Solar irradiance flux density
H_t°	Latent heat of vaporization
I_E	Mean Earth IR flux density
c_p	Specific heat capacity at constant pressure

Chapter 1

Introduction

The space environment that satellites face is uncertain and challenging for survival and operation. Traditionally, to mitigate the effects of uncertainty - in both the design process and operation - spacecraft design involves large allocation of margin across the system to ensure compliance with requirements and constraints in the worst-case uncertain outcomes. However, this approach often involves large contingencies and margins that are arbitrary functions of the stage of development [1]. Such application of margin is by design conservative, and it has been noted that this method for allocation often creates overlap and excess margin, especially at the conceptual stage [2]. This approach to providing guarantees of feasibility results in overdesign, sacrificing capability and performance. For spacecraft systems that are more severely constrained - either by limitations of size or due to an extreme environment - overdesign may not be feasible. As spacecraft systems continue to shrink in size, methods are required to ensure feasibilty, while limiting the sacrifice of performance. To illustrate this, the next section will describe some small satellites and their associated design challenges.

1.1 WaferSat: Integrated Satellites-on-a-Chip

Richard Feynman once famously said that "there is plenty of room at the bottom" during a lecture in 1959 [3]. He was speaking of the prospect of miniaturization - in particular, that the ability to view and manipulate objects at extremely small scale could allow for greater complexity in a smaller amount of physical space. His ultimate vision for miniaturization included the rearrangement of atoms at will. While we have not reached this stage, many advancements in microelectromechanical systems (MEMS) miniaturization have enabled manufacturing of electrical and mechanical systems at ever decreasing sizes, with the current state of the art at 10 nm die sizes [4]. If applied to satellite production and integration, continued miniaturization presents a potentially disruptive change to the traditional paradigms that define satellite designs.

1.1.1 SmallSat Trends

In recent years, there has been a rapid growth of small satellite missions, particularly at the 1 kg to 10 kg mass-scale. A prolific example of this is the CubeSat, which has demonstrated useful functionality at low size, weight, and power (SWaP). While often sacrificing capability in comparison to larger satellites, missions that adopt small satellites can take advantage of lower launch and manufacturing costs, shorter development cycle times, and greater potential for rideshare launch opportunities. In fact, many missions to date have successfully supported scientific payloads [5] and even operated outside of Earth orbit [6].

While the cost and time advantages of CubeSats from a launch and development standpoint are notable, the continued reliance on manual assembly, integration, and test [8] presents a new challenge: the high volume production to supply the many satellites needed for large distributed systems. A solution is to leverage the existing global semiconductor and mobile device-manufacturing infrastructure and the related manufacturing methods to build tightly integrated electronic systems for the high

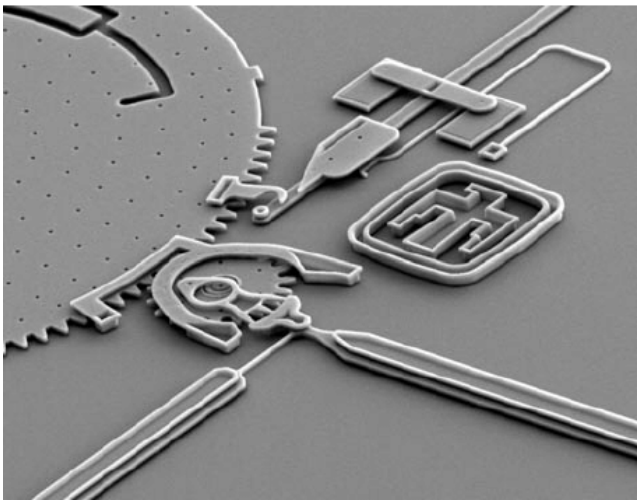

Figure 1-1: MEMS-produced, µm-scale, mechanical silicon gear mechanism by Sandia National Laboratories [7]

volume production of even smaller yet capable satellites i.e. lower mass without sacrificing useful capability and functionality. A potential solution is to incorporate silicon-based production methods that utilize MEMS manufacturing, originally pioneered in the electronics industry to mass produce integrated circuits. MEMS micromachining processes have expanded to apply to increasingly complex systems at small scale as demonstrated in Figure 1-1. Advancement in MEMS techniques can be applied to many subsystems of small satellites such as sensors, microfluidics and propulsion, and actuators [9].

1.1.2 MEMS Integration

Satellite integration is a traditionally laborious process involving manual assembly. MEMS production for satellites offers an attractive alternative. The automated, low touch-labor processes reduce human-in-the-loop interactions, streamlining the integration and reducing potential errors. Highly efficent, rapid MEMS production applied to satellite assembly could enable mass production and the fielding of proliferated constellations. Such constellations could leverage large numbers of MEMS wafer-satellites (WaferSats) to form large effective-aperture diameter imaging

systems [10, 11]. The Rayleigh Criterion indicates that the angular resolution of an imaging system is linearly proportional to the diameter of a system for a given imaging wavelength. Formation-flight patterns of WaferSat-like chipsat subapertures are predicted to have a much lower estimated cost relative to the size of the effective synthetic aperture [12] as shown in Figure 1-2. All studied 500-member swarm patterns have a significantly lower scaling of cost to effective diameter than monolithic aperture systems as diameter becomes large. Thus, proliferated swarms of WaferSats can open up the possibility of cost-effective, extremely large aperture imaging systems.

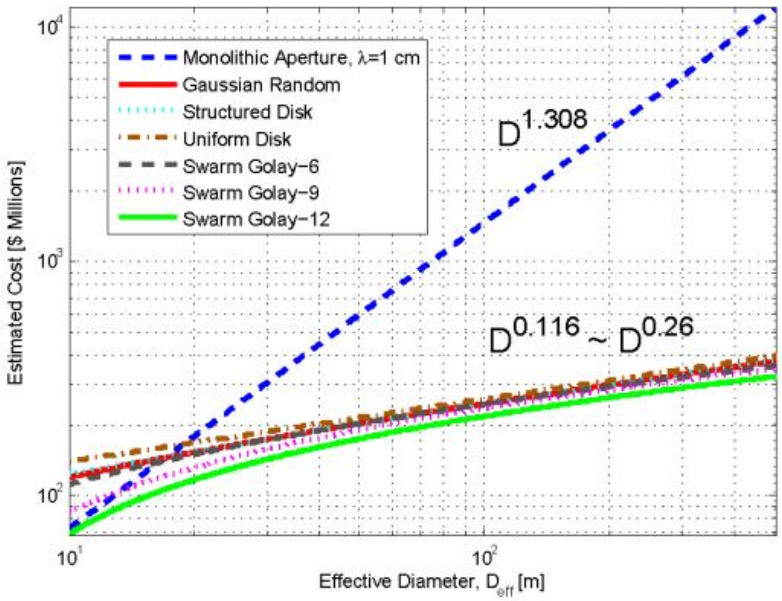

Figure 1-2: Comparison of estimated cost relative to effective aperture diameter of various femtosat swarm patterns [12]

1.2 High Aspect Ratio: A Novel Satellite Design Regime

MEMS production necessitates the processing of silicon substrate wafers of specific sizes and dimensions. There are various standard diameters and thicknesses, but the current state of the art utilizes wafers that are hundreds of millimeters in diameter

and less than a millimeter thick.

The flat form factor of standardized silicon wafer sizes can be expressed as an aspect ratio (Æ), or a non-dimensional ratio of the diameter, D to the thickness, t.

$$\text{Æ} = \frac{D_{wafer}}{t_{wafer}} \tag{1.1}$$

In particular, Æ is related to the ratio of spacecraft surface area to volume. Whereas a cube-shape ($\text{Æ} \approx 1$) has low surface area to volume, a flat wafer ($\text{Æ} \approx 100$) has extremely high surface area to volume ratio.

1.2.1 Scaling of Surface Area, Volume, and Mass

The surface area and volume scaling can be compared for a cube and a disk of specified Æ. For a cube, the volume and surface area are

$$\begin{aligned} V_c &= s^3 \\ A_c &= 6s^2 \end{aligned} \tag{1.2}$$

Correspondingly, for a disk, they are

$$\begin{aligned} V_d &= \pi r^2 t \\ A_d &= 2\pi r^2 \left(1 + \frac{2}{\text{Æ}}\right) \end{aligned} \tag{1.3}$$

where s is the side length, r is the radius, and t is the thickness.

Although the shapes of a cube and disk are different, a similitude can be generated by matching the scaling of surface area and volume. The resulting system of equations matching surface areas and volumes of the cube and disk shapes (Equations 1.2

and 1.3 respectively) is

$$\begin{aligned} s^3 &= \pi r^2 t \\ 6s^2 &= 2\pi r^2 \left(1 + \frac{2}{Æ}\right) \end{aligned} \tag{1.4}$$

By solving the system of equations in 1.4 for the $Æ$, a similar scaling is generated with roots given in Equation 1.5. A WaferSat with $Æ$ matching these roots would exactly match the surface area to volume scaling of a cube. Note that the negative value for $Æ$ is a degenerate root, therefore, there are two real physical values for which $Æ$ causes a realistic similitude between surface area and scaling of a disk and cube.

$$Æ_{similar} = \{-8.683, 0.404, 2.279\} \tag{1.5}$$

Figure 1-3 shows the scaling of surface area to volume of various shapes and aspect ratios. Note that a sphere has the lowest theoretical ratio of surface area to volume for a uniform solid. The cube represents a uniform solid cube or that of a disk with either of the two positive roots of Equation 1.5. There are two reference points along the cube curve: a standard 1U CubeSat shape, and a 1Q PocketQube shape [13]. A WaferSat of a standard 200 mm diameter and with uniform pure silicon density and total mass of 150 g has an $Æ$ of 97.59. Note that this $Æ$ is far higher than the values in Equation 1.5 that create a similar scaling with a cube. Furthermore, the value of the ratio of surface area to volume of the $Æ = 97.6$ disk is more than an order of magnitude higher than that of a cube (or low aspect ratio disk), suggesting a significantly different $Æ$ regime than that of other small satellite standards (and that of other large satellites).

1.2.2 Subsystem Design Implications of $Æ$

The ratio of surface area to volume has many implications in the design and scaling of spacecraft subsystems such as thermal, power, moment of inertia, and structures.

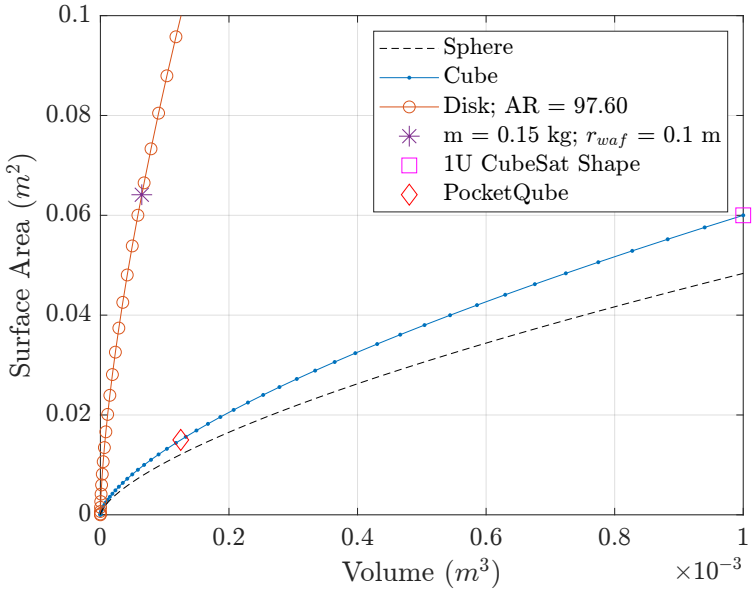

Figure 1-3: Surface area vs. volume scaling for specified shapes and aspect ratios

The dominant mode of heat exchange for spacecraft with the external environment is through radiation. For a uniform solid, volume and mass will be directly proportional to the heat capacity. Therefore the extreme temperatures and rates of thermal equilibration will increase in magnitude as the ratio of surface area to volume increases. This is observable in the rearranged 1D heat equation (Equation 1.6). The time rate of change of heat (dominated by radiation) is proportional to surface areas. Therefore for large surface areas, the time rate of change of heat, Q, is large. A low volume, v, yields low heat capacity for a given uniform solid of density, ρ and specific heat capacity, c_p. The time rate of change of temperature, T is expected to be high when surface area to volume is high and the system will converge on thermal extremes rapidly.

$$\frac{\partial T}{\partial t} = \frac{\partial Q}{\partial t}\frac{1}{\rho v c_p} \tag{1.6}$$

Figure 1-4 shows the estimated quasi-steady state temperature ranges of blank silicon wafers[1] in a 400 km altitude low Earth orbit (LEO) with one surface always

[1]These measurements assume emissometer-measured thermal surface properties of a blank Si wafer measured at MIT LL. $\alpha_{vis} = 0.73$ and $\varepsilon_{IR} = 0.70$

Earth-facing. The difference in rate of thermal change between the high and low $\mathcal{AR}$ disks is stark. The extreme temperatures that are attained for the high $\mathcal{AR}$ disks suggests that the thermal subsystem will be pushed significantly closer to design limits of survivability compared to the cases that scale similarly to cube-shapes. The $\mathcal{AR} = 100$ case (solid orange line) is shown with the corresponding theoretical zero-mass equilibrium temperatures (dashed orange). At the extremes, the transient temperatures nearly reach equilibration.

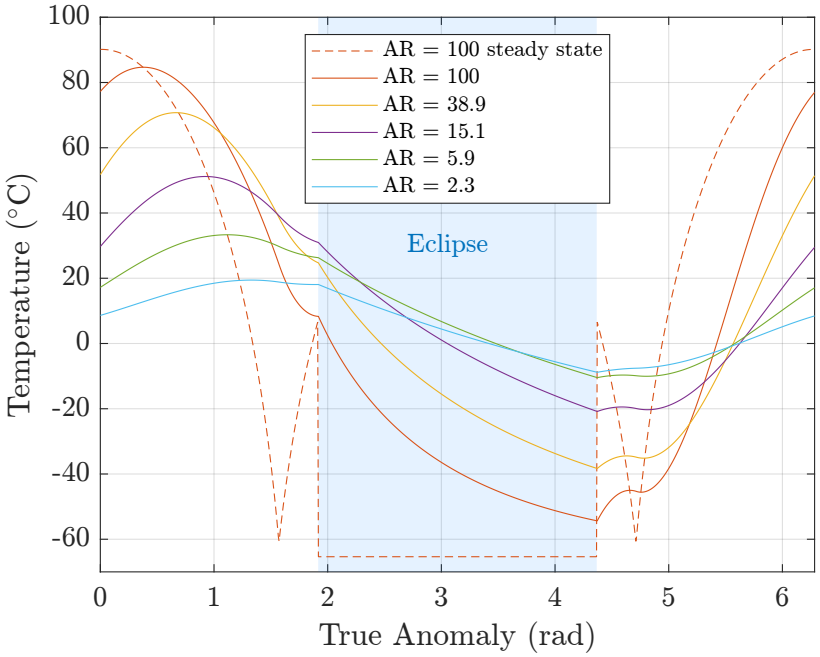

Figure 1-4: Estimated temperature ranges over one orbit for various aspect ratios of blank silicon wafer in 400 km orbit, nadir-facing orientation

The high $\mathcal{AR}$ form factor does have some benefits, particularly to power generation for solar cell-based systems. A large surface area presents a large potential area of solar exposure relative to the system mass, resulting in a large mass-specific power capability. Another high $\mathcal{AR}$ satellite system in development at the Aerospace Corporation is DiskSat, a SmallSatellite built into a sandwich composite panel one meter in diameter and one inch thick. Scaling analysis performed by Welle et al. [14] for high $\mathcal{AR}$ DiskSat shows the increased specific power. In Figure 1-5, the estimated

orbit average power is compared to the system mass for several spacecraft shapes. High $\mathcal{AR}$ DiskSats are shown to have a much higher mass-specific orbit-average power even when compared to traditional satellites with deployable solar arrays.

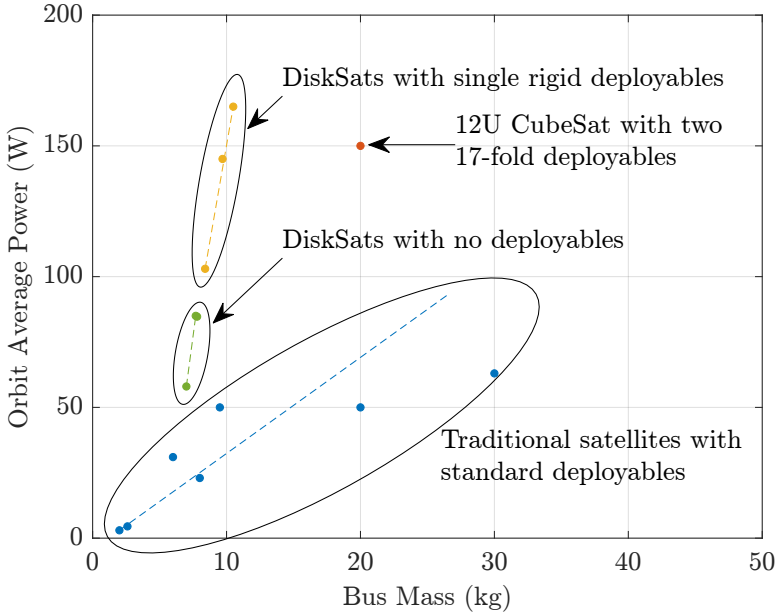

Figure 1-5: Comparison of orbit average power vs. bus mass trends for disk form factor and traditional s/c [14]

High $\mathcal{AR}$ has impacts across other subsystems. Since components are typically populated on the surfaces of the wafer, handling is often restricted to the edges. In an edge pinned launch configuration, the scaling of static maximum stress scales as $\sigma_{max} \propto \mathcal{AR}^2$. Dynamic structural modes scale approximately as $\omega \propto\tilde{} \mathcal{AR}^{-1}$ (the scaling is slightly less due to the numerical roots from Mindlin circular plate theory [15]). Therefore, as $\mathcal{AR}$ increases, static stresses increase and dynamic modes decrease, increasing the challenge of structural survival in the launch configuration (noting also that silicon is a brittle material). Out of plane moments of inertia scale as $I \propto \mathcal{AR}^2$, increasing the required torques to reorient the system at a given rate. Furthermore, the high $\mathcal{AR}$ yields unique rarefied gas effects [16] and solar pressure disturbances [17] since higher $\mathcal{AR}$ WaferSats will act as a sail. Drastic scaling with $\mathcal{AR}$ move the design regime of WaferSats outside of the norms for large satellite design, presenting unique design challenges.

1.3 Margin for Robustness or Lack Thereof

During the design process, analysis is used to predict outcomes in operation. Though it would be simpler to operate on the assumption that all information is perfectly known, in practice, some elements of the system may be unknown. This uncertainty manifests in several ways. Parametric uncertainty refers to a lack of accurate knowledge of the value of a quantity, whereas non-parametric uncertainty refers to a more complex lack of knowledge (e.g., due to an error or inaccuracy in modeling). Uncertainty may be further classified as either epistemic or aleatoric. Epistemic, or systematic, uncertainty refers to a lack of information that could in theory be measured, but is otherwise unknown. As such, it is considered to be reducible [18]. In contrast, aleatoric uncertainty is stochastic. Aleatoric uncertainty can be characterized as a distribution, but due to its stochastic nature, it is irreducible; at each attempt at measurement, the value will be different. The type of uncertainty that the work of this thesis will focus on is aleatoric, parametric uncertainty. Specifically, the sources of uncertainty (to be described in greater detail in § 4.2) will refer to uncertainty from the environment. As such theses sources of uncertainty are stochastic and beyond the control of the satellite designer. The presence is nevertheless ever present and requires mitigation.

A traditional method to counter the effects of uncertainty in spacecraft design is to budget for margin and contingency. Approaches within NASA utilize parameterized data from past missions to prescribe contingencies and margin as functions of design maturity [1]. These margin allocation schemes are built on the assumption that uncertainty decreases with time and that application of liberally applied margins across the system provides a strong bulwark against the effects of uncertainty. While effective in providing performance guarantees for large systems, this conservatism often leads to over-design.

When optimizing in the absence of uncertainty, the Pareto optimal set of designs appear as individual points. However, when evaluated under uncertainty, each non-

dominated design - once considered to be a single, deterministic outcome - becomes a distribution of distinct outcomes. In her thesis on Reconfigurable Constellations (ReCon), Lowey demonstrated that the Pareto front is not a simple curve, but has a width representing the uncertain maximum and minimum performance range. This is shown in Figure 1-6a where the non-dominated points are shown with a set of green maximum and minimum expected performance lines. Interestingly, the higher performance solutions also have a wider range of performance values. Uebelhart used a similar method of bounding boxes (similar to uncertainty bars) over multiple metrics on the Pareto front. As shown in Figure 1-6b, Uebelhart's analysis further showed that due to variation in the sizes of bounding boxes, some nominally dominated designs near the Pareto front can actually provide more reliable performance than some nominally non-dominated designs [19]. Such designs that are nominally inferior in performance are more robust under realistic, uncertain conditions.

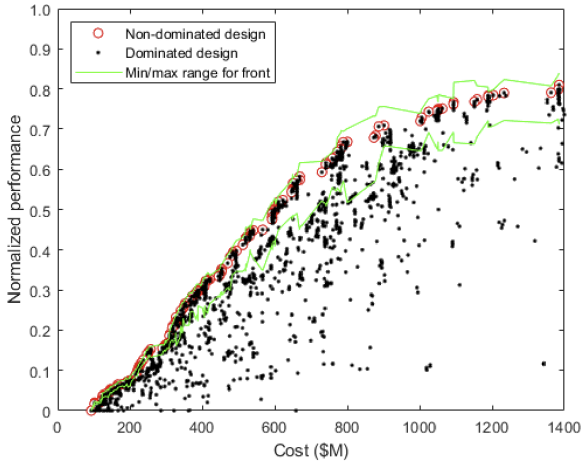

(a) The non-dominated designs may exhibit an uncertain range of maximum and minimum performance under uncertainty [20]

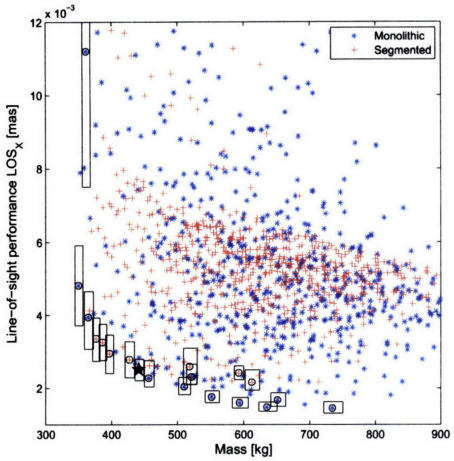

(b) Some nominally dominated designs may actually provide *greater* reliability (smaller bounding box) under uncertainty than nominally non-dominated designs [19]

Figure 1-6: Two examples of Pareto fronts with uncertain metrics, expressed as a min/max range (left) and bounding boxes (right).

As noted by the work of Lowey and Uebelhart, it may sometimes be worthwhile to select a design that is nominally off of the Pareto front (but near to it) if such

designs exhibit lower sensitivity to uncertainty. This filtering for lower susceptibility to uncertainty can produce greater robustness of designs in uncertain conditions. However, the selection of design that are nominally dominated indicates a reduction in nominal performance; this is the 'price of robustness' [21]. Seldom are the best performing designs also naturally robust. If robustness is desired, nominal performance must often be traded. However, if designs are made to dynamically respond to uncertainty, the deleterious effects could be compensated. Rather than designing for all worst case outcomes simultaneously, designs could adjust to a given, measured state of uncertainty in operation, thereby reducing the size of the bounding boxes of outcomes around designs, potentially saving designs once considered to be nominally optimal but not robust.

1.4 SmallSats, the Space Environment, & Design Difficulty

The difficulty of the WaferSat design example is derived from the severe resource constraints and the high sensitivity of thermal conditions to high $\mathcal{AR}$. The design difficulty makes it challenging to survive and operate in even the relatively simple space environment of Low Earth Orbit (LEO). In contrast, design difficulty could also result in a system where the thermal environment is more challenging for survival, but system resources are less constrained (i.e., a larger system). Such an example might include a SmallSat (larger than a WaferSat or DiskSat) in deep space. Resource constraints may be less severe, but a cold thermal environment of deep space is a significant challenge for survival and operation.

WaferSat and other high $\mathcal{AR}$ systems serve as an exemplar in this thesis to explore a new satellite design domain that could benefit from a new design methodology. However, there are potentially other similarly severely constrained systems that could also require and benefit. An example is explored from a high level in Appendix B.

1.5 Research Statement & Thesis Structure

The next generation of SmallSat systems like WaferSat and DiskSat push the boundaries of spacecraft design. MEMS processing offers many benefits that can enhance small satellite production at small scale. The high $\mathcal{AR}$ can allow for larger areas for solar arrays, sensors, and apertures. Flat form factor systems can be efficiently packed for launch, enabling deployment of large ensembles acting in concert. While each individual system may be small, a constellation could be greater than the sum of its parts. However, the high-aspect ratio, low SWaP form factor associated with MEMS processing pushes the design regime to a novel, unexplored design space for satellites. In particular, constraints related to rapid thermal equilibration on extreme temperatures in orbit, present new design challenges on other satellite subsystems such as power. This new design regime offers few feasible solutions for the certain problem and even fewer when uncertainty is considered. When subjected to uncertainty, low SWaP compounded by tight subsystem couplings causes high sensitivity to uncertainty.

In order to realize the benefits of new systems like WaferSat, new approaches are needed to ensure that such systems can reliably survive and operate in the uncertain and harsh space environment. This work will introduce a novel method of operational responsiveness and adaptability to address the thermal-power challenges of highly coupled and sensitive systems under uncertainty. The thesis is structured as follows. In Chapter 2, the prevailing approaches to SmallSat design, design of coupled systems, and robust optimization are reviewed. Gaps in previous research are identified, and an approach to address those gaps is offered. In Chapter 3, the methodology for operationally responsive and adaptive mitigation of uncertainty is developed in detail with the aid of a simplified example design problem. The methodology is then applied to a more detailed WaferSat design problem in Chapter 4. Multiple designs are identified using different combinations of responsive and adaptive uncertainty mitigation approaches. The methodology is further applied to another high $\mathcal{AR}$

system, DiskSat in Chapter 5 in which a detailed comparison between responsiveness and adaptability is explored. In Chapter 6 conclusions, thesis contributions, and suggestions for future work are discussed.

Chapter 2

Literature Review

This work is at the juncture of three main fields of research: pico satellite design, coupled systems & sensitivity, and robust optimization. SmallSat design encompasses the current state of the art for design, and prior developments in addressing the challenges as satellite designs decrease in scale. It is noted that as complex systems - that include a multitude of interacting subsystems - the decrease in scale, the effects of interactions between subsystems can significantly drive behavior of the system. As such, methods exploring approaches in quantifying and designing for coupled and sensitive systems is explored. Finally, in order to design systems that will offer persistent performance under uncertain conditions, approaches in robust optimization are reviewed.

2.1 Pico Satellite Design

Small Satellites offer many benefits but also introduce many challenges. Development of pico satellites (PicoSats), at a smaller scale than CubeSats - and the move to flat form factor chip-scale satellites in particular - presents a novel design regime, distinct from that of traditional large satellites or even smaller CubeSats. The design

approaches to this new design regime are relatively unexplored.

CubeSats, which follow a standard for mass and volume [22], are comprised of one or more 10 cm cube units. CubeSats typically fall in the nano satellite class, from 1.1 kg to 10 kg. By comparison, smaller systems like WaferSat would likely be in the pico satellite mass class from 0.1 kg to 1 kg.

2.1.1 History of Chip-Scale Satellites

The concept for silicon-based chip-scale satellites is not new, however, the design for fully silicon MEMS produced satellites has not yet been realized for spaceflight. As early as the late 1990's, Helvajian and Janson of the Aerospace Corporation noted that the advancements in MEMS technology could be leveraged to mass produce silicon spacecraft through batch-fabrication [23, 24]. In particular, they noted advancements in MEMS sensors could allow for micromachined attitude sensors. Microfluidics could be utilized for micro-thrusters to provide attitude control [23, 25].

Barnhart furthered these concepts with detailed subsystem analysis for SpaceChip, a monolithic satellite-on-a-chip concept [26]. Barnhart explored the challenges within the subsystem sizings, noting that unregulated thermal design would experience temperatures as low as -72 °C and as high as 96 °C. The design was further matured with an intermediate PCBSat with a parts list [27]. The most recent publications on this work from 2009 seem to move away from the monolithic integrated MEMS SpaceChip concept, opting to encase several PCBSat boards in a thin, aluminum structure [11].

Similarly, the Aerospace Corporation concepts for ChipSats eventually developed into the MEMS tethered PicoSatellites. At 400 grams, each consisted of printed circuit boards encased in an aluminum structure. The MEMS PicoSats were one of several satellite missions deployed out of the OPAL spacecraft mothership in 2000 [28]. The concept would eventually grow into the CubeSat standard of today [22, 29].

Figure 2-1: A MEMS PicoSatellite being loaded into a spring-loaded deployer on the OPAL spacecraft [29]

Recently, there has been interest in the development of ChipSats that range in the tens of grams total mass (and even single grams [17])). Such spacecraft, adopt a survival strategy known as R-selection, borrowing a term from biological natural selection [30]. R-selected spacecraft trade individual probability of success for mass-reproducibility [31]. Since a large number of identical spacecraft are fielded, mission success is not reliant on the success of any one satellite. A statistical number of satellites may survive and operate, but little engineering effort is expended to improve individual survivability, thus efficiency is low. The R-selection approach is in direct contrast to the K-selection [30] strategy wherein great effort is expended in order to ensure survival of one or a few satellites - the more common approach for the satellite design process.

A version of such R-selected spacecraft, the Sprite ChipSats, flew aboard the KickSat-1 mission in 2016 [32] and again on KickSat-2 in 2019. The mass-produced, gram-scale approach favors very simple spacecraft with low individual capability. The Sprite spacecraft that were deployed from KickSat did not have batteries, thermal control, or attitude control. Therefore, operation depended on chance illumination of the solar arrays to power the system as it tumbled in orbit. As such, downlinks

from only 4 distinct Sprite ChipSats were confirmed out of 128 [33]. Elimination of batteries reduces the need for thermal control - the Sprites were allowed to equilibrate on extreme temperatures.

Further concepts for ChipSats and WaferSats also propose interplanetary spaceflight, utilizing the high $\mathcal{AR}$ to act as a small solar sail [17] or ground-based laser-accelerated sail [34]. However, such concepts have not yet solved the thermal challenges of high $\mathcal{AR}$, but propose future work for an embedded radioisotope thermoelectric generator or beta converter to heat the system [35]. Further surveys of recent work on ChipSats note that research is focused on hardware design, communications, and propulsion, noting that any high power designs that make use of batteries will first need to solve the thermal challenges arising from the low mass and form factor [36].

2.1.2 The Thermal-Power Challenge of Small, High $\mathcal{AR}$ Satellites

As satellite SWaP decreases, so too does the ability to maintain a survivable temperature range. In particular, as mass decreases, the thermal capacity decreases, resulting in a high sensitivity of temperature to net heat flow. Furthermore, the challenge is exacerbated by the large ratio of thermal radiating surface area to mass of WaferSat. The combination of large radiating surfaces and low thermal capacitance result in rapid thermal equilibration at extreme temperatures. This is analogous to the temperature swings of deployed solar panels. Much like WaferSat, solar panels have high $\mathcal{AR}$, very thermally absorptive and emissive solar cell surfaces, and low thermal capacity. Even though solar cells have greater efficiency at low temperature, they are typically not thermally regulated and have large temperature swings [37]. The difference however, is that the most thermally sensitive components of larger spacecraft are not thermally linked to the large radiating solar cell surfaces.

Recent small satellite concepts in the cube form factor include the PocketQube - a proposed standard in the hundreds of grams. Analysis of the roughly 250 g SMOG-1 PocketQube shows that despite the low heat capacity, the relatively low surface area results in fairly limited temperature extremes attained in a LEO orbit [13]. Furthermore, the internally closed volume creates thermal gradients through the structure, resulting in even lower temperature variation near the center of the spacecraft.

Thermal control of high $\mathcal{R}$ spacecraft has not been directly addressed. Previous designs for chip-scale spacecraft have stated that high $\mathcal{R}$ yields rapid equilibration on thermal extremes that precludes the inclusion of any thermally sensitive components such as batteries. In a thesis on Monarch ChipSats, Adams states that the energy requirement of heating batteries to a survivable range during eclipse exceeds the possible energy generation with solar cells [38].

Thermal analysis of a four inch diameter silicon wafer of various thicknesses in LEO orbits is shown by Bruno, Maghsoudi, and Martin [39]. They present a simple, forward Euler based thermal integration to show the estimated transient, quasi-steady state temperature ranges. The results confirm that thermal cooling equilibration time constants typically are shorter than the eclipse duration of LEO orbits, resulting in wide temperature swings per orbit. Several different power dissipation schemes are presented, but do not allow for significant mitigation of the thermal equilibration on temperature extremes.

In his Master's thesis, Stout notes that traditionally, the thermal design of spacecraft is assumed not to be a design driver and as such the thermal control design is often "outside-the-loop" and occurs late in the design process after other major design decisions have been finalized [40]. However, at the new scale and form factor of WaferSat, thermal considerations must be taken into account sooner and in conjunction with other subsystems.

2.2 Coupled Systems and Sensitivity

Complex systems such as satellites involve many interacting subsystems. The level of interaction only increases as the scale is reduced. Mass, volume, and surface area are limited, and must be shared between the subsystem domains. Furthermore, WaferSat, with a high $\mathcal{AR}$ pushes subsystems nearer to their design limits.

2.2.1 Sensitivity Analysis

A prevalent technique for estimating the sensitivity of systems to sources of uncertainty is variance based sensitivity analysis. In particular Monte Carlo sampling over parameter uncertainty can be used to calculate the Sobol' Indices [41]. First order Sobol' Indices, or main effects, measure the normalized contribution of individual parameters on the variance of a model output (i.e., variance due solely to that parameter). Total effect indices map the contribution of parameter variation to the model output variance and includes effects of interactions between parameters. This is particularly useful for tracing the impacts of uncertainty to specific areas of the system. For spacecraft design, this can be applied to understand what areas of the system and what couplings are most impacted by sources of uncertainty.

More recent work helps to codify components of a system by the relative impact on propagation of change throughout a system [42]. Components can be one of several types: constants, absorbers, carriers, or multipliers of change. Constants are areas of the system that are completely unchanged by uncertainty. Absorbers of change reduce the propagation of change whereas multipliers generate more changes as the names suggest. Carriers are neutral, in that they absorb and create new changes at the same rate. This sorting of components of a system draws attention to areas of the system where problematic multipliers may cause large variance in outputs relative to input uncertainty. The design of key absorbers within a system can create buffers to limit the propagation of change due to uncertainty and maintain predictable performance.

Realistic models of uncertainty - based on measured data from prior space missions in literature - will be used to evaluate effects of uncertainty in the application sections of this thesis. Those sources and models will be discussed as they are introduced and applied. Techniques for sensitivity analysis are useful to trace the net effects of uncertainty to identify areas that require mitigation. Strategic placement of absorbers of change within the system can help to stem the propagation of change. In this work, the notion of dynamic absorbers of change will be explored.

2.2.2 Design Decision Rules

Work by Gross, presents a complex satellite design example utilizing a rule-based approach [43]. An integrated model of the theoretical FireSat mission from SMAD [44] is presented with a constraint network. Design rules are established that aid in the selection of non-parametric decisions in the design process. Analysis with the decision rules reveals non-obvious switching points in the optimal topologies in different areas of the design space. In Figure 2-2, a Pareto front of radio frequency (RF) systems for a satellite. The different colors at the top surface of the Pareto front represent the optimal architecture. The bands of distinct RF architectures reveal that ideal architectural decisions can be identified based on location in the design space, providing a methodology for architectural decision-making under different mission scenarios. The architectural design decision rules are established based on a combination of system sensitivities and design objectives that govern where in the design-space to search.

There are methods - particularly in linear optimization - that focus on exploring and maintaining the sets of active constraints in a model. The active constraint invariancy method by Hadigheh proposes a method for finding the range of tolerable parameter variations that maintains the same set of active constraints at optimality, effectively maintaining the same optimal solution basis [45]. Realizations of parameter uncertainty within the active constraint invariant set result in optimization with

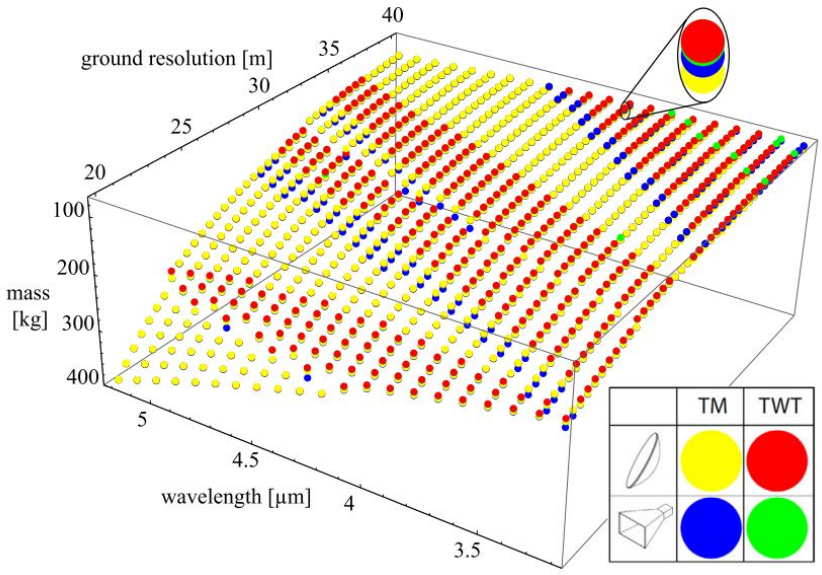

Figure 2-2: Plot of optimal communications antenna decisions in various areas of design space [43]

the same basic solution 'family'. This ensures that any re-tuning of variables (i.e., small changes to maintain optimality and feasibility) to reoptimize in response to uncertainty involves consideration of the same active and slack constraints.

2.3 Robust Optimization

There are many approaches to the mitigation of uncertainty in the field of robust optimization. However, many sacrifice some optimality in favor of resistance or insensitivity to uncertainty. In this section, literature for robust design to mitigate uncertainty is explored.

2.3.1 Robust Solutions Sacrifice Nominal Performance

It is often noted that optimal solutions in the absence of uncertainty are not necessarily still optimal in the presence of uncertainty. Whereas the nominal solution, under no uncertainty, may be optimal, its performance often degrades rapidly with

perturbations due to uncertainty, rendering it unreliable (except where uncertainty is extremely low). This is illustrated in an example by Deb and Gupta and shown in Figure 2-3 [46]. Depicted is a 1D minimization of $f(x)$, where B would be considered nominally optimal (in the absence of uncertainty). However, slight variations in x result in significant increases in $f(x)$, resulting in far worse performance. In contrast, the performance in the vicinity of A is very reliable even under uncertainty, even though its best case solution is never as good as the nominal $f(x)$ of solution B. For the given assumed uncertainty, A would be considered to be a robust solution; on average, it performs better than B and is thus more practical. In [46], Deb and Gupta

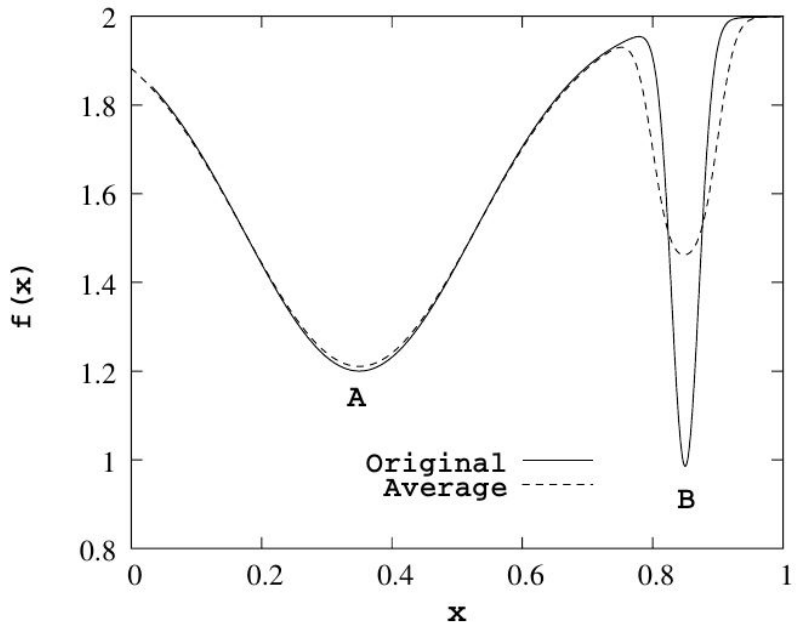

Figure 2-3: 1D example comparing a robust but non-nominally optimal solution (A) and a nominally optimal but non robust solution (B) [46]

propose two metrics of robustness for a given set of neighborhood uncertainty over δ (i.e., a region) for a minimization of the function f. A solution is Type I robust if it achieves the global minimum of the mean of f over the neighborhood (effectively a globally optimal expected value). A solution is Type II robust if it achieves a global minimum for f with a constraint that the deviation from the mean is below some threshold η over the δ-neighborhood of uncertainty (effectively a maximum allowable

variance). These two robustness metrics can be used to augment a multi-objective optimization problem to return solutions that are robust.

Type I and II robustness metrics are incorporated into the Many Objective Robust Decision-Making (MORDM) framework [47, 48]. The MORDM framework utilizes an evolutionary algorithm to propose solutions to a multi objective optimization problem. For a defined, multi-dimensional uncertainty set, Monte Carlo sampling is used to generate an ensemble of uncertain 'states of the world' (SoTW) - each a draw from the uncertainty set. Proposed solutions are subjected to the ensemble and statistical measures - namely expected value and variance - are evaluated. These objectives augment the original set of nominal objectives, guiding the evolutionary search towards solutions that have a balance of high nominal performance and Type I and Type II robustness.

MORDM has been applied extensively in the literature to problems related to water distribution wherein uncertainty over future demand and supply of water resources are deeply uncertain[1] [47, 48, 49]. In such optimizations, the objectives are often in conflict, requiring tradeoff between different objectives. Consideration of the multiple objectives separately allows for analysis of the Pareto optimal tradeoffs and the costs associated. Additionally, robustness metrics to assess the expected value, variance, satisficing constraints, and regret-based metrics are introduced alongside the nominal performance metrics [51]. Results in the robust design of water distribution networks show clear tradeoffs between the key nominal and robustness metrics, indicating a cost of robustness. However, the results do suggest improvement over traditional, conservative planning methods (in terms of cost and water surplus). Finally, key constraints related to catastrophic failures - such as flood damage - can aid in parsing the Pareto front via creation of worst-case percentile objectives [52].

While the statistical objectives of MORDM allow for improvements to identification of a robust Pareto front, it is observed that the tradeoff of robustness is

[1] *Deep uncertainty* refers to scenarios in which the knowledge of the predicted distribution of uncertain outcomes is lacking [49, 50], elevating the difficulty of planning for uncertain outcomes.

often a reduction in the level of nominal performance (the original, non-statistical performance objectives). Designs that persist on the pareto front under uncertainty modeling rely on designs with statistical margin and natural desensitization to sources of uncertainty with absorbers of change.

Whereas the NASA systems engineering approach calls for standardized margin allocation as a function of design maturity [1], recent work by Thunissen proposes a probablistic method for the optimal allocation of margin for the system at hand [2]. Probabilistic simulations of outcomes are performed to optimally allocate margins to balance risk across the system. In a distinct approach, Guenov et al., also present a method to optimally allocate margin across a system, introducing the concept of a 'margin space' containing all allocations of margin [53]. Explorations of margin allocation reveal that in systems with many interacting subsystems, strategically placed margin may have impacts in multiple areas, obviating the need for margin in every subsystem.

2.3.2 Adaptive Approaches to Robustness

The MORDM approach achieves robustness by sacrificing some nominal performance via insertion of margin in key locations as absorbers of change. However, further improvements to robustness can be obtained by adapting to uncertainty as it is realized. Real Options Theory presents a framework for flexibility in the face of uncertainty by delaying decision-making until new information is available. By delaying decisions, there is a 'right but not an obligation' to respond with some recourse after uncertainty is realized [54]. Thus, the value of the delayed decision lies in the ability to choose a course after new information is available.

Real Options Theory originated in finance [55], focusing heavily on valuation of a delayed decision and the monetary cost to gain the option. More recently, Real Options Theory has been applied to engineering applications [56]. In engineering

applications, there is a focus on the required up front design that enables the option, for example design of a parking structure foundation to accommodate more stories later [54] or a phased communications satellite deployment to accommodate an over or under estimate of demand [57].

The Real Options Theory approach provides insight into the value and requirements of delayed decision-making, however the literature focuses mainly on engineering decisions to expand or contract based on uncertain demand or supply estimates. Another line of work, Tailoring and Tuning, developed by Masterson [58], focuses on maintaining performance in the presence of uncertainty via operationally tunable design elements. The design is posed as a multi-stage process, where the design is first tailored for a combination of performance and tuneability. After the hardware is built, it is then tuned to compensate for parametric uncertainty, and maintain performance. The design approach, Robust Performance Tailoring for Tuning (RPTT) incorporates both static robustness and tuneable robustness in the cost function. When applied to a precision optical structures testbed, RPTT is shown to improve the probability of meeting requirements over the range of worst-case modeled parametric uncertainty [59]. Due to computational complexity, the tuning optimizations are performed at the worst-case uncertainty extreme vertices, assuming a convex model.

The Tailoring and Tuning methodology was expanded to incorporate the Isoperformance methodology [60]. The Isoperformance Tuning method combines modeling and hardware tuning to successively update the model to reduce the uncertainty set until the system is tunable to within requirements [61]. The method reduces the required number of hardware tests while improving the model evaluations to successfully tune the system.

Other multistage, adaptive approaches to robust optimization focus on the inclusion of safety factors in the robust counterparts [62]. Due to the often prohibitive growth in computational complexity related to nested optimization, problems are often reformulated around heuristic decision rules with an approximation of optimal

behavior. Tuning parameters are defined as functions of realizations of uncertainty [63]. These decision rules, often in a linear or piecewise linear form, provide a method for tractable evaluation of near-optimal adaptive behavior over modeled uncertainty sets. Decision rule polices are usually considered to be near-optimal as they incorporate the safety factor to provide a probabilistic guarantee of success.

2.3.3 Spacecraft Thermal Adaptive Approaches

There are a number of implementations that could produce operationally adaptive thermal systems. Large spacecraft, particularly those that experience a widely variable thermal environment due to inner and outer cruise through the solar system [64] utilize mechanical louvers with a bimetallic strip to open and close as a function of temperature [65]. The opening and closing of the louvers alters the effective emissivity of the underlying radiator offering operational adjustment. Note that the bimetallic strip offers a pre-tuned, fixed recourse response; the response as a function of temperature cannot be changed on orbit. Attempts have been made to replicate the same mechanical effect on MEMS wafers [66, 67], however the effective emissivity change was extremely limited [68].

Progress has been made in solid state dynamic emissivity surfaces. Thermochromics offer a dynamic emissivity that is a function of temperature [69, 70, 71]. The variation of emissivity with temperature is fixed in operation but can be tailored in the design phase for specific temperature ranges (similar again to a fixed-recourse decision rule). Electrochromics offer a dynamic emissivity surface that is controlled by a bias voltage [72, 73, 74], allowing for variation of the emissivity at will. The EclipseVED electrochromic coating has demonstrated variation in mid-IR emissivity from below 0.1 to greater than 0.9 in lab tests [75, 76]. The coating was also successfully tested in space as a payload aboard the MidSTAR-1 spacecraft in 2007 [75].

Other methods for dynamic thermal-power control involve attitude control to vary

the thermal view factors to cold space and the sun. Due to a highly elliptical orbit, the Space Technology Research Vehicle (STRV) spacecraft had insufficient power to heat the spacecraft to survive long periods of eclipse. Active management of the thermal view factors via attitude control allowed for mitigation of the thermal extremes with limited heater power available [77]. Recent work to optimize for solar exposure and thermal view factors has shown tradeoffs between high power and minimum temperature variation for a CubeSat payload [78].

Implementations of operationally dynamic thermal systems have also been variously implemented on larger spacecraft. Many deep space missions have utilized radioisotope heater units (RHU) in order to provide localized heating through radioactive decay of a small pellet. As the rate of emitted heat is not controllable, alternative methods of rejecting unwanted heat is required. On the Cassini spacecraft, RHUs were mounted on the thruster heads on a rotating bimetallic spring [79]. Half of the RHU canister was radiatively insulated, and half was radiatively emissive. The bimetallic spring was designed so that during the inner portion of the cruise, when solar exposure was greatest, the RHUs would be oriented with the insulating side facing towards the thruster heads and heat would radiate out to space. When in the outer portions of cruise, as the temperature decreased, the RHUs would be turned so that the heat was radiated inward towards the thrusters. Thus, the heat capture rate was automatically regulated - even without control over the radioactive heat dissipation.

In addition to dynamic variation of thermal radiation, various methods have also been use to create selectable dynamic thermal conductivities, i.e., the ability to conductively couple or decouple at will. In order for the Pathfinder Mars rover to meet the wide thermal requirements of cruise and on the surface of Mars, the temperature sensitive components were conductively coupled to RHUs. To prevent overheating during cruise, the temperature sensitive components were also conductively coupled to a radiator. Once on the surface of Mars, where overheating was not a concern, a clamp was released, mechanically breaking the conductive pathway to the radiator

[80, 81]. More recently, there has been development on a device that uses coefficients of thermal expansion to either create a long, low conductivity thermal pathway, or a thermally-shorted high conductivity pathway [82].

Operationally dynamic thermal approaches have also been applied to the third type of heat transfer, convection. The Active Thermal Control for Multispectral Earth Sensors (ACMES) SmallSat will include a technology demonstration of an active pumped fluid loop on a SmallSat [83, 84]. Throttling of the working fluid flow rate affords control over the amount of heat rejection (from payload to radiator) depending on internal payload power dissipation levels. Furthermore, adjustment of the orientation of the radiator will provide favorable radiative view factors at different points in the orbit.

Over the years, various active and passive thermal mitigations have been implemented on large and small spacecraft. However, many of these technologies have been implemented as one-off technologies, implemented for very specific thermal scenarios. In general, many of these thermal mitigations were developed to compensate for a scheduled, gross change in the thermal environment during some phase of the mission. Moreover, many of the mitigation methods applied to larger spacecraft involved mechanical systems that may not be as amenable to smaller scale satellites like WaferSat. Recent development of technologies has focused on generalization of active methods, but no methodologies exist to model and trade the ability of such systems to continually compensate for the effects of thermal uncertainty.

2.4 Technical Gap and Research Objective

The move to smaller, high $\mathcal{AR}$ satellites exposes the challenges associated with designing for static robustness. Whereas it is worthwhile to trade system resources and performance of larger satellites for feasibility, the heightened thermal sensitivity and restricted system resources of high $\mathcal{AR}$ systems renders this tradeoff far more costly.

At smaller scale, there are also fewer SWaP resources available to use for margin. A new methodology is needed to ensure that such systems provide a guarantee of performance under uncertainty (through improved feasibility).

A summary of research gaps and the proposed approaches is shown in Table 2.1. WaferSats provide many potential benefits by utilizing MEMS processing to enable reliable, efficient mass-production of small satellites. The flat, high $\mathcal{AR}$ form factor for small satellites necessitates design for a novel design space not addressed in the design of larger satellites. Approaches to date for chip-scale satellites have avoided the thermal management design challenge of high $\mathcal{AR}$ by simplifying the design and eliminating sensitive components such as batteries. Limiting the design to components that do not require thermal regulation results in much simpler satellites with more limited capability. At the small scale, there is also a high coupling of subsystems, necessitating that subsystem design decisions be made jointly.

Many robust optimization approaches focus on allocation of margin and selection of designs that are desensitized to sources of uncertainty. In this process, these approaches only need to sacrifice a small relative amount of performance in order to achieve robustness. However, limited available SWaP on WaferSat and DiskSat constrains the available static margin that can be allocated to create robust designs and the associated sacrifice of performance is more severe.

Table 2.1: Summary of identified research gaps and corresponding thesis contributions

Research Gaps	**New Approaches to Address Gaps**
Robust optimization: • high performance sacrifice for robustness • results in overdesign with arbitrary margin across system	Creation of a framework of passively responsive robust and active adaptive approaches to mitigate the effects of uncertainty on the active, performance-limiting constraints through continual compensation of uncertain states during operation
Previous operational compensation methods: • robustness, responsiveness, adaptability set by manual weights, not driven by requirements • design for tuning of worst-case uncertainty too conservative • tuning did not optimally compensate over continuously changing uncertainty in time	Development of a formalized, two-stage optimization methodology to: • design sets of variables before operation • continuously re-optimize during simulated uncertain states of the world • incorporation of selectable statistical feasibility criteria as optimization objectives • weighting of tailoring and tuning with constraints on implementation of mitigations
Sprite ChipSats: • survival & operational rate of 3% • avoided thermal design by eliminating batteries • limited functionality of operating units (RF beacon only)	Application of responsive & adaptive methodology on WaferSat, a highly SWaP-constrained, novel high $Æ$ satellite. Thermal feasibility is increased with limited performance sacrifice.
DiskSats could offer higher mass-specific power if thermal sensitivity of high $Æ$ can be addressed	Application to DiskSat, a larger high $Æ$ system, demonstrates a more complex scenario with adaptive redistribution of heat among nodes of a larger system.

To increase the robust performance of satellites in this regime, the thermal-power design challenge can be addressed with an adaptive approach, allowing for operational tuning of design variables in response to uncertainty to allow for greater robust feasibility of nominally optimal performance.

This thesis will build upon prior methods to adaptive design evaluate, particularly the dynamic tailoring and tuning methodology. Selection of operational tuning variables can be extended with exploration of active constraint sets in order to select those that have the greatest impact on the design feasibility. This will allow for a detailed trade studies of available tuning variables, especially with respect to the limited resources and space available on small satellites such as WaferSat.

The authority of tuning was previously assessed via the compensated range of uncertainty. To this end, extreme vertices were evaluated, assuming convex behavior over the bounded uncertain set in order to avoid many function evaluations in nested optimization. This had the effect of designing the tune for the worst-case (i.e., maximin or minimax), and often sacrificed nominal performance. Mapping of active constraint sets to feasibility can aid in the creation of optimal decision rules to optimally or near optimally tune the operational variables in response to a particular state of the world of uncertain realization. The decision rules can enable evaluation of full sets of the ensemble of uncertain states of the world, allowing for evaluation of the statistical robustness objectives to aid in guiding the optimization to further search the pareto optimal set of solutions that trade robustness and nominal performance.

As a small, flat satellite system, WaferSat will be launched as a member of a large set of spacecraft. Optimization for performance and adaptability will enable exploration of multiple types of designs that balance robustness while preserving nominally optimal performance. Beyond WaferSat, the application of adaptability could allow for reductions in the overdesign due to excessive margin, whilst limiting the sacrifice of optimality. These improvements will aid in the advancement of the design approach to constrained satellite systems, giving rise to capable satellites that

reliably provide maximal utility with staying power under uncertain conditions.

The objective of this work is ***to*** optimize resource-constrained SmallSats with highly coupled subsystems ***by*** designing for operationally responsive and adaptive mitigation of uncertainty, ***while*** maintaining high performance.

Pursuant to this objective to address the gaps in the literature, this work has produced four contributions.

1. Created a framework of responsive robust and adaptive mitigation of uncertainty with limited performance sacrifice
2. Developed a two-stage optimization methodology for the prior design for and operational design of responsiveness & adaptability
3. Application to WaferSat: Demonstrated identification of unique designs of equal performance and feasibility
4. Application to DiskSat: Explored tradeoff between responsiveness & adaptability

The first contributions two are related to the methodology. In contribution one, a framework is created to define two distinct types of mitigations: passive responsive and active adaptive mitigations. This framework is developed into a two-stage optimization methodology to increase constraint satisfaction with limited performance loss. The second two are applications to two constrained SmallSat systems. In contribution three, three unique design families are identified for the design of WaferSat, presenting multiple responsive and adaptive avenues to achieve the same goals. The continuous tradeoff between responsiveness and adaptability is explored in greater detail in contribution four, the application to DiskSat.

Chapter 3

Design for Performance, Robustness, Responsiveness, & Adaptability

In this chapter, a methodology is presented for simultaneous optimization for performance, robustness, and adaptability, building upon current approaches to design optimization and robust design. A simplified WaferSat design optimization problem is presented and used as an illustrative example throughout.

3.1 Nomenclature & Relationships

In order to describe the methodology, some nomenclature and the associative relationships must first be defined. For simplicity, the optimization process will be separated into two phases in time: the ***a priori*** phase and the ***a posteriori***. The a priori phase encompasses the traditional design phase in which variables are selected and optimized before launch. The a posteriori phase, or the operational phase, involves the responses or adaptation to specific realizations of uncertainty. The nomenclature is further separated into variable sets, processes, outcomes, and a quality describing the outcomes. The relationships are summarized in Table 3.1 and are described in

more detail in the following subsections.

Table 3.1: Nomenclature Relationships

Variable Set		**Process**		**Output**	**Resultant Quality**
Static Variable[1]	→	Static Tailoring[1]	→	Static Margin	Static Robustness
Dynamic Variable[1]	→	Responsive Tailoring[1]	→	Responsive Variable[2]	Responsive Robustness
Dynamic Variable[1]	→	Adaptive Tailoring[1]	→	Adaptive Variable[2]	Tuneability
Adaptive Variable[2]	→	Tuning[2]	→	Adaptive Margin	Adaptability
				1 a priori phase;	2 a posteriori phase

3.1.1 Defining Variable Sets

The two temporal phases contain variable sets. Variable sets defined in the a priori phase are assumed to be fixed once the a posteriori phase begins (i.e., the values or decisions made over these sets cannot be adjusted in operation). Variable sets in the a posteriori phase are changeable during on-orbit operation - either as a passive response or through active management which can be reprogrammed in flight.

The ***static variables*** are traditional variables that are set during the a priori phase and remain fixed in operation. The ***dynamic variables*** are set during the a priori phase in order to define the variable sets in the a posteriori phase. Note that the values of dynamic variables themselves do not change in operation, instead they constrain response or adaptability in the a posteriori phase. As an example, in the case of the thermal louvers from § 2.3.3, behavior of the slats is defined by the design of the bimetallic strip. The dynamic variable set would include selection of the metals, initial shape, and therefore design of the open-close temperature setpoints. However, once the spacecraft is in orbit, the temperature setpoints cannot be modified. As such, the louvers are responsive to changes in heat loads, but are not able to adapt the response.

The operational phase involves two variable sets: ***responsive variables*** and ***adaptive variables***. Responsive variables passively adjust in operation in reaction to stimulus. The behavior of response variables is therefore said to follow a fixed

recourse. The opening and closing of bimetallic thermal louvers are an example of responsive variables. The design of the governing dynamic variables produces a fixed response to temperature stimulus. In contrast, adaptive variables are changeable in operation by command. Such variables follow a controlled response in reaction to stimulus. It is important to note that adaptive variables offer the flexibility of changing the response on the fly. If the thermal louver angle was controlled by servos rather than bimetallic strips, the commanded angle would be an example of an adaptive variable.

3.1.2 Processing Variables Sets

In this work, the variable sets are defined according to several processes. Design of variable sets in the a priori phase are said to be ***tailored*** and variable sets that are dynamically adjusted in the operational phase are said to be ***tuned***.

Design of static variables using ***static tailoring*** is used in order to produce static margin against active constraints. During static tailoring, a specified amount of static margin against each constraint can be allocated; static variables are changed accordingly. The margin against constraints provides a buffer in the event of variance due to uncertainty. Therefore, more outcomes remain feasible even when perturbed by uncertainty.

Since the responsive and adaptive variable sets are governed by dynamic variables, there is a two-step process. Dynamic variables are set via tailoring in the a priori phase. The process of ***responsive tailoring*** produces the responsive variable set and ***adaptive tailoring*** produces the adaptive variable set. The fixed recourse behavior of the response variables results in responsive robustness; i.e., there is a passive mitigating response to the effects of uncertainty. The adaptive variables are actively ***tuned*** during operation. This adaptability produces ***adaptive margin*** that can be actively tuned or re-tuned as necessary to mitigate the net effects of off-nominal

states.

3.1.3 Outputs & Resultant Qualities

Outcomes from the processes and variable sets are described by the associated quality. Static margin, produced by static tailoring possesses the quality of *static robustness*. Static robustness affords the ability to withstand the perturbing effects of uncertainty without changing. This is a more conservative approach and it is notable that the design for static margin often involves a sacrifice of optimal performance.

In contrast to the rigidity of the a posteriori behavior of statically robust designs, design for and operation with responsive variables results in the ability to react to the perturbations due to uncertainty. This quality is described as *responsive robustness*. Responsive robustness is a passive, fixed-recourse reaction to individual draws from uncertainty, or *states of the world* (SoTW). Passive response to uncertainty keeps complexity low, as the response occurs automatically under uncertainty - no active control or estimation of the SoTW is necessary. Effectiveness of responsive robustness is dependent on the ability to model and predict the range of uncertain SoTW as the behavior cannot be changed after the a priori phase. If actual encountered uncertain states differ drastically from the predicted uncertain states, the intended passive mitigation may be insufficient.

Adaptive tailoring to produce an adaptive variable set results in the ability to change variables during the a posteriori phase, described as tuneability. The end result of the optimized tuning response to uncertain SoTW is in turn described as *adaptability*. In distinction to the passivity of responsive robustness, tuning and adaptability are active mitigations to the effects of uncertainty. Furthermore, since tuning is active, there is some ability to retune, or change the adaptive behavior in response to new or unexpected SoTW.

Design for feasibility may combine elements of static robustness, responsive ro-

bustness, and adaptability. In general, different combinations of the three elements may provide the same ability to meet the constraints of the system under uncertainty. The set of designs that produce the same level of performance through different parametric and non-parametric means are ***isoperforming*** [60, 85]. The set of designs that produce the same modeled statistical probability of constraint satisfaction can be said to be ***isofeasible***. The intersection of isoperforming and isofeasible designs achieve the same function with different form. Consideration of non-unique designs that are isoperforming and isofeasible may provide multiple avenues for reliable design optimization under uncertainty.

The discussed nomenclature and associated relationships outline at a high level, the main elements of the methodology. In the next sections, the methodology will be discussed in greater detail, building up from the outline. Additionally, a simplified example problem is presented to serve as an application to provide context for the stages of the methodology.

3.2 A Simplified WaferSat Example Problem

Throughout this chapter, the following example problem will be used to demonstrate the elements of the methodology. In this section, a simplified WaferSat thermal and power design problem is posed.

3.2.1 Design Variables & Parameters

In this problem, it is assumed that a 200 mm diameter, 150 gram silicon WaferSat is in a circular low Earth orbit (LEO) at an altitude of 400 km. The WaferSat is in an orientation where one surface is always nadir-facing. For worst-case thermal purposes, all analyses assume a solar β angle (the angle between the Earth-Sun vector and its

projection in the orbit plane) of zero. A depiction of the orbit is shown in Figure 3-1. Note that only one of the axes in the figure is defined: the Earth-Sun axis. The y and z axes are deliberately undefined and therefore this orbit and analysis will apply to any orbit inclination (which does not itself have a direct thermal impact). The β angle of zero results in the most challenging thermal extremes; eclipse is longest in duration (using the simplified cylindrical umbra assumption), and solar exposure of the zenith surface is greatest for the nadir-facing attitude (at $\nu = 0$ sunlight incidence is normal to the zenith surface). As β angle increases, the length of eclipse decreases and the peak solar exposure of the zenith surface occurs at steeper angles of incidence (for the nominal nadir-facing attitude).

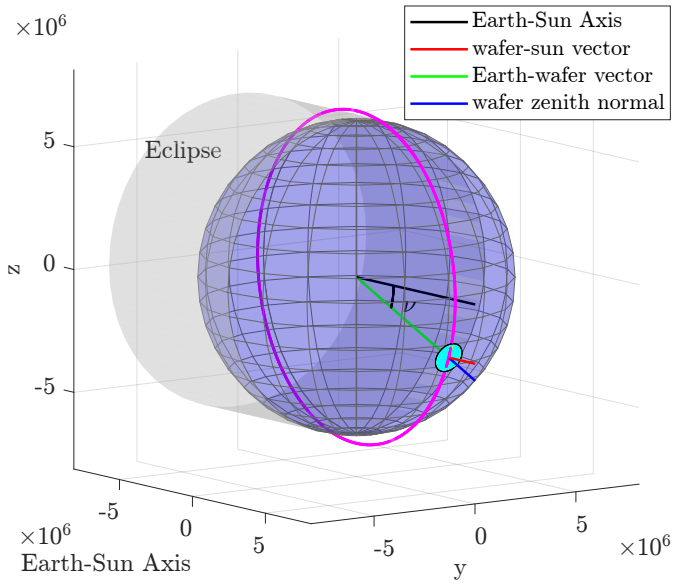

Figure 3-1: A zero β angle, 400 km altitude, circular orbit. WaferSat is depicted at a true anomaly, ν referenced to the closest position to the Sun.

The set of static design variables is summarized in Equation 3.1, which includes the thermo-optical design of surfaces as well as allocation of solar array area. The solar array area is expressed as a physical fill factor of the zenith surface, f_{SA} (fractional area coverage). The emissivities, ε_* refer to the IR wavelength emissivity of nadir and zenith surfaces. α_* refers to the visible wavelength absorptivity of the nadir and zenith surfaces. Note that the thermo-optical properties of the solar array are assumed to be

constants from literature values for solar cell coverglass: $\varepsilon_{SA} = 0.69$ and $\alpha_{SA} = 0.92$ [37]. The static design variables are represented in Figure 3-2 with fractional solar cell coverage and surface thermo-optical variables. Note that in the single-node modeling, the net thermo-optical surface properties are treated as area-weighted means rather than the represented non-homogeneous area segments.

$$\mathbf{v}_s = \Big[f_{SA}, \quad \varepsilon_z, \quad \alpha_z, \quad \varepsilon_n, \quad \alpha_n \Big]^T \tag{3.1}$$

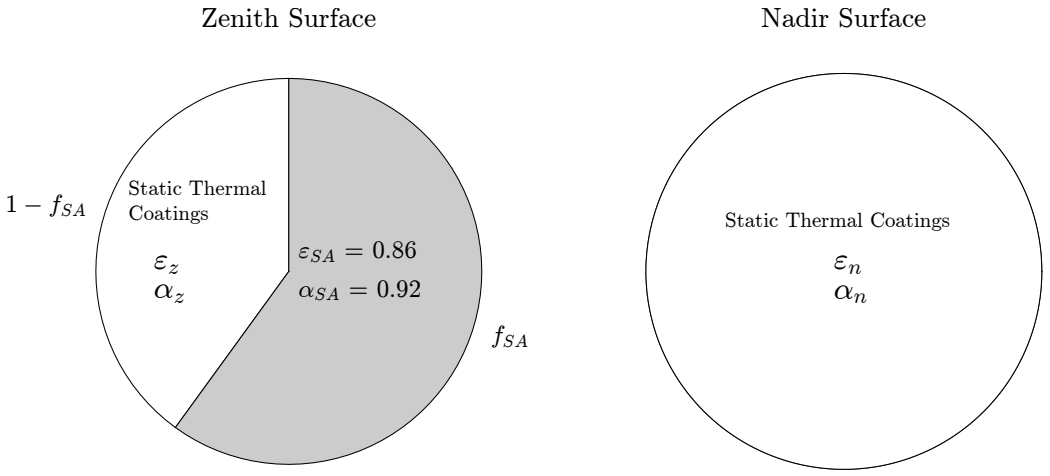

Figure 3-2: Simplified representation of WaferSat surfaces

As more elements of this simplified WaferSat example are expanded upon, more sets of design variables will be introduced in the following sections of the chapter.

3.2.2 Power Maximization & Thermal Constraints

To evaluate the ability of WaferSat to support a payload, a nominal power performance metric is introduced. At any given time, the internal power dissipation levels defined during eclipse, P^e_{int} or sunlight, P^s_{int} can be distributed throughout the system (to payload, heaters, subsystems, etc.) and it is assumed that all internally dissipated power results in internal heat in the system. To measure the ability of WaferSat to support a high-power payload at an arbitrary point in the orbit,

the performance objective is maximize the minimum of eclipse and sunlight power dissipation levels (P^e_{int} and P^s_{int} respectively), shown in Equation 3.2. The resultant value is the minimum amount of power that can be guaranteed to be supplied at any point during the orbit. It is also assumed that any internal power dissipation results in heat dissipation within the system. As such, it is always possible to reduce power dissipation in the sun to reduce sunlight internal heat and increase power dissipation in eclipse to increase heating during eclipse to improve thermal survival (this results reduced performance as P^s_{int} is lower). The final two constraints of the formulation in Equation 3.2 set a 'performance floor' - that is, the internal powers must exceed a threshold of 1.4 W at all times.

$$\begin{aligned} \max \quad & \min\{P^s_{int}, P^e_{int}\} \\ \text{s.t.} \quad & T_{min} \geqslant T^{req}_{min} \\ & T_{max} \leqslant T^{req}_{max} \\ & 0 \leqslant \int_0^{2\pi} P_{SA} d\theta - \int_0^{2\pi} P_{int}(\theta) d\theta \\ & f_{SA} \leqslant 0.75 \\ & P^e_{int} \geqslant 1.4 \\ & P^s_{int} \geqslant 1.4 \end{aligned} \tag{3.2}$$

The first two constraints of Equation 3.2 are the temperature requirements - set by the most limited operable temperature limits of all elements in the system. T_{min} and T_{max} represent the minimum and maximum temperatures attained in stable temperature cycling (i.e., per-orbit thermal transients are converged in a repeated cycle). The third constraint defines a net non-negative electrical energy requirement on a per-orbit basis. That is, over the course of a single orbit, the total amount of electrical energy generated with the solar array is greater than or equal to the total internal electrical energy dissipated (electrical energy generation must exceed or equal internal dissipation over the course of each orbit). Note, that this does not set any constraint on when power can be dissipated; the internal power dissipation can occur at different

values at any point in the orbit. It is assumed that any electrical energy that is not immediately dissipated is stored in batteries. Additionally, it is assumed that the maximum possible physical fill factor of the solar arrays is 75% on any surface.

Note that so far, this formulation only provides a method for optimizing in the absence of uncertainty. As such this serves only as the base of the optimization that will grow as more subelements of the methodology are introduced in the subsequent sections.

3.3 Nominal Optimization

Optimization is often first thought of in the absence of uncertainty. In an idealized and certain world - where all parameters and variables are assumed to be exactly known and there is full confidence in the validity of the models - all outcomes are deterministically predictable. With these assumptions, it is reasonable to optimize without margin. In this section, an approach to nominal optimization is presented. Through an example, it is shown that while a nominal optimal solution offers high performance, feasibility under uncertainty is severely limited in sensitive systems.

3.3.1 Optimization for a Certain World

In the nominal optimization process, a heuristic optimizer is used to optimize over the static variable set. In this work, a simulated annealing optimizer is used, but other global heuristic optimizers may also be used such as genetic algorithms, particle swarm optimization, or stochastic gradient descent. The methodology of this thesis is most amenable to optimization strategies that utilize stochastic sampling of populations and iterative solution proposals. Such optimizers are more generalizable and do not require access to derivatives or specifics of the model. Simulated annealing (SA) was

selected for its generality: it is non-specific to the thermal/power modeling (modeling is described in greater detail in Chapter 4), and it is amenable to the different types of static and dynamic variable sets that will be introduced later. The simulated annealing algorithm is introduced with an adaptive neighborhood sampling scheme to adjust for variable solution acceptance rates [86] (note that the term 'adaptive' in this context is distinct from the adaptive design. The adaptive neighborhood refers to variance in SA distribution sampling to regulate the probability of solution acceptance). Other heuristic optimization methods such as genetic algorithms and particle swarm optimization could also be used for this methodology due to their similar generalizability around modeling. It is useful to note however, that the methodology could be adapted to incorporate gradient-based optimization which could increase computational efficiency - a critical benefit as the scope of modeling increases.

The nominal optimization process is expressed in Equation 3.3 and is illustrated in Figure 3-3. In generalized form, the objective of the optimizer is to maximize a performance objective and is subject to the inequality constraint function, $\mathbf{c}(x)$. Note that $\mathbf{c}$ represents an arbitrary set of functions - linear or nonlinear - to generate any number of m constraints. x represents the arbitrary list of inputs that define the constraints. Similarly, an equality constraint function, $\mathbf{c}_{eq}(y)$ defines equality constraints. The optimizer operates over the first variable set described in § 3.1, the static variable set, $\mathbf{v}_s$.

In the certain case, the optimizer will produce a nominal optimal solution (or a close approximation of global optimality in the case of a heuristic optimizer). Note that simulated annealing does not provide a guarantee of optimality, but does aid in the avoidance of local optima. Adjustment of the annealing schedule and neighborhood search allow for reliable convergence on an optimal solution. In Figure 3-3, the solution proposal has not yet been subjected to uncertainty; at this point, its performance is assumed to be a single, deterministic outcome with guaranteed feasibility.

$$\begin{aligned} \max_{\mathbf{v}_s} \quad & P_{erf} \\ \text{s.t.} \quad & \mathbf{c}(x) \leqslant 0 \\ & \mathbf{c}_{eq}(y) = 0 \end{aligned} \tag{3.3}$$

In order to evaluate the nominal optimal solution under uncertain conditions, distributions of uncertain parameters are injected to propagate the nominal optimal solution to generate a distribution of outcomes under many uncertain SoTW. This is illustrated in the right block of Figure 3-3 (blue dashed lines). A comparison of the certain and uncertain evaluations will be shown in § 3.3.3. In the new distribution of outcomes, a smaller fraction of outcomes are feasible.

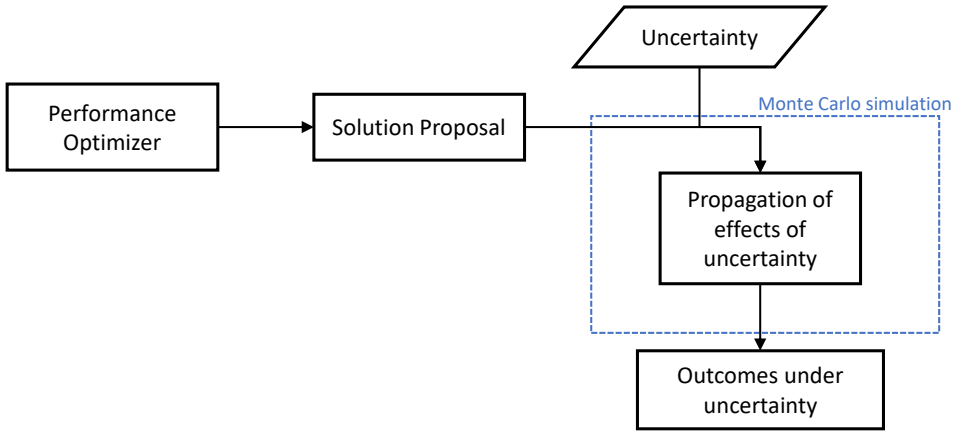

Figure 3-3: Nominal Optimization; optimizer does not consider uncertain outcomes. After the optimization process is complete, the optimized design may be subjected to models of uncertainty to evaluate performance under uncertainty to reveal a lack of robustness.

3.3.2 Active Constraint Set

In order to understand how the operational tuning variables will influence feasibility, it is useful to first identify the key and driving active constraints in the design, i.e., those constraints that prevent further increases in performance. Understanding the

active constraints reveals the design drivers and importantly, the limits of feasibility under uncertainty. Locating the active constraint sets will allow for later evaluation of how dynamic and adaptive variables can influence the active constraint sets to maintain optimality of specific solution families.

In the simplified WaferSat example, the active constraints are the temperature requirements. In Figure 3-4, the transient, single-node temperature profile of the WaferSat is shown in stable oscillation over five orbits (note that there is an arbitrary initialization temperature of 290 K; the temperature trace converges on the stable oscillation within one cycle). The two insets show a zoom in of the non-monotonic changes in temperature at two points in the orbit: the start and end of eclipse (depicted as blue patches) or dawn and dusk respectively. During these two points, the nadir side of the WaferSat is directly illuminated by the sun. At dusk (just before the start of eclipse), solar incidence angle - the angle between the nadir surface normal and the sun-WaferSat vector - is decreasing up until the point that WaferSat passes into the umbra (assumed in this analysis to be cylindrical). At dawn, as WaferSat exits the umbra, the angle of nadir solar incidence is high and decreases until the WaferSat is edge-on to the sun. The result is a period of nadir-surface heating exiting eclipse, followed by a period of cooling near the edge-on orientation to the sun.

The magenta dashed lines represent the temperature requirements (notional in this example) and the grayed regions represent temperature requirement violations. The maximum and minimum temperatures meet the temperature constraints at equality, indicating that they are active and limiting to performance. For power performance to increase, the solar array area must increase, resulting in a greater portion of surfaces coating with highly emissive and absorptive area (exacerbating heating in the sun and radiative cooling during eclipse, respectively).

In the zero uncertainty case, this nominal solution is feasible. However, as noted in § 1.2.2, the high $\mathcal{R}$ of the system causes high temperature sensitivity. Any deviation from the nominal heat flows in or out of the system results in large changes in

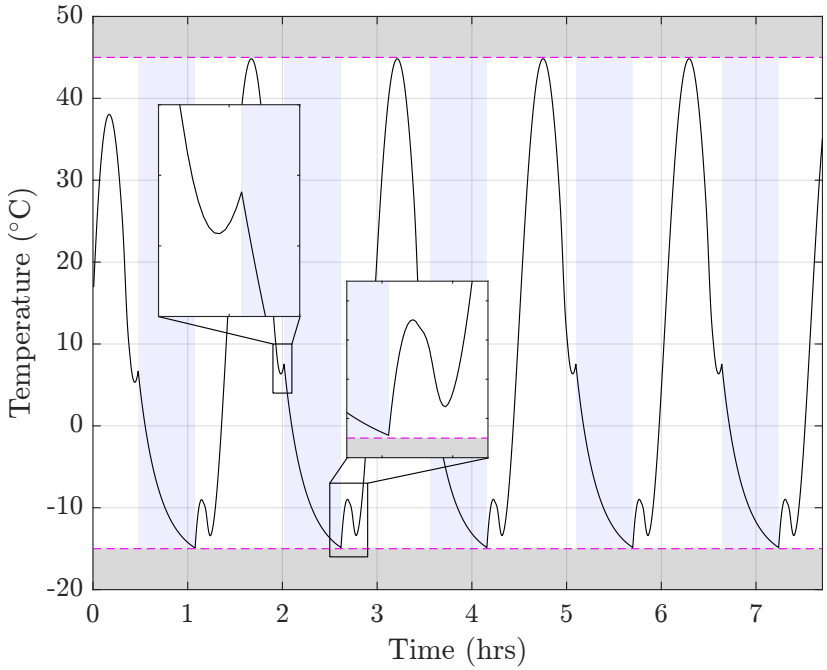

Figure 3-4: Quasi-steady state single-node temperatures of nominal optimal design with no uncertainty. Note that the temperature constraints are met at equality.

temperature and thus the ability to meet the active constraints. As uncertainty is added to the scenario, the feasibility of this nominal optimal solution will diminish.

3.3.3 WaferSat Example: Nominal Optimal Design is not Robust

In the absence of uncertainty, the performance of the nominal optimal design provides a guaranteed performance level since the outcome is deterministic and certain. In the simplified WaferSat example, a simple parametric uncertainty is introduced, resulting in a varied distribution of performance outcomes. A comparison between the certain performance outcome and the degraded distribution of performance outcomes in the presence of uncertainty is presented.

In the absence of uncertainty, there is no variability in outcomes. The modeled performance of the system is exactly, deterministically known. This is represented

in Figure 3-5, where there is a 100% probability of producing a power performance of 1.83 W. There is also a 100% expectation of exceeding the required minimum performance threshold of 1.4 W and there is a 100% expectation of meeting the temperature constraints that were met at equality.

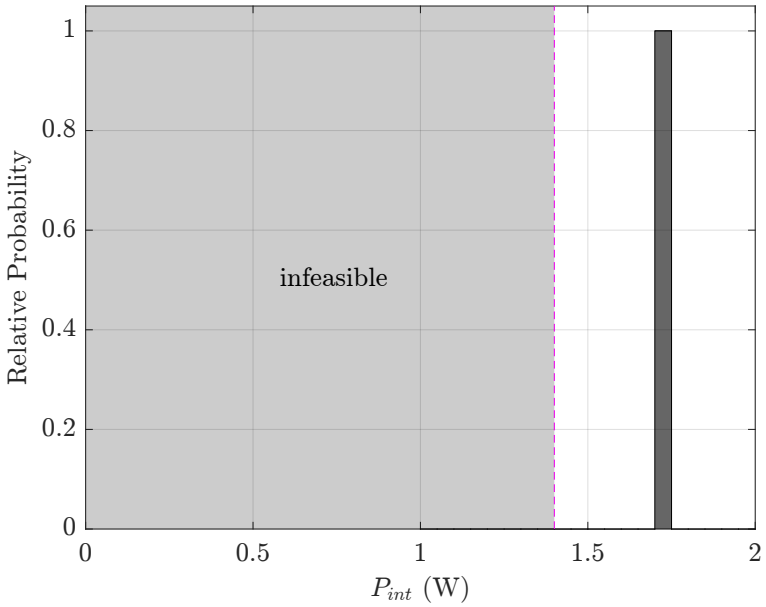

Figure 3-5: One performance SoTW with no uncertainty

In reality, there are potentially many sources of uncertainty and therefore, there exists variance in outcomes. In this example, a simple parametric uncertainty is introduced in one variable: the static emissivity coating of the nadir-facing non-solar array surface area. This could represent an error introduced in manufacturing where the precise static emissivity coating of the nadir surface is not exactly and reliably reproduced. This manufacturing error will result in large variability of the thermal balance which is already at the edge of feasibility.

As shown in Figure 3-3, to model the effects of uncertainty, uncertain parametric distributions are introduced to evaluate the nominal optimal solution. To generate a distribution of uncertain emissivities, an uncertain perturbing factor, δ is sampled from a Gaussian distribution with zero mean and 0.05 variance, $\delta \sim \mathcal{N}(0, 0.05)$. The distribution in Figure 3-6 represents the weighted range of realizations of the

nadir-side net emissivity. Note that in this example, this distribution is used as an illustrative example; it does not represent a realistic distribution of static emissivity coating variance in manufacturing. The negative tail of the distribution was truncated in order to prevent emissivity realizations less than 0.08. The mean value of the distribution is centered on the target emissivity value (the value designed under no uncertainty). More realistic sources and distributions of uncertainty will be used in more detailed examples in the following chapters.

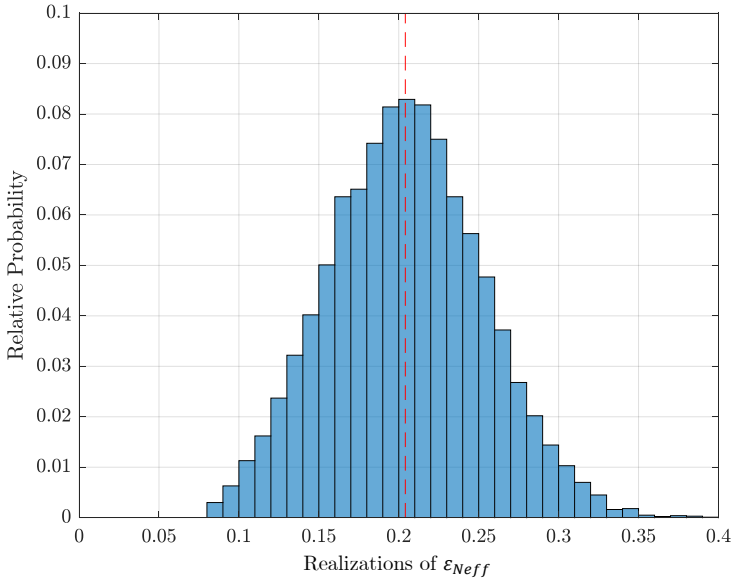

Figure 3-6: The effective emissivity, ε_{Neff} of the nadir-facing surface resulting from Gaussian uncertainty in static coatings

When modeling the power performance over the ensemble of SoTW using the static effective emissivity coating distribution from Figure 3-6, what was once a single deterministic outcome, becomes a distribution of power performance outcomes. Histograms of the power performance are shown in Figure 3-7. The minimum power performance threshold of 1.4 W is shown as a vertical magenta dashed line, and the infeasible region is grayed out. The nominal optimal outcome under no uncertainty is shown as a black single-bin histogram, representing this single outcome. Without uncertainty, there is a 100% guarantee of the nominal 1.74 W of power performance and a 100% guarantee of meeting the temperature constraints at equality.

In stark contrast, in the uncertain case, the net radiative heat fluxes changes on the nadir surface for each ε_{Neff}. The power dissipation values must change in the sunlit and eclipse conditions in order to adhere to the temperature constraints. The new ensemble of outcomes under the modeled parametric uncertainty is shown in Figure 3-7 as a blue histogram of power performance outcomes. Under the uncertain case, the expected value of performance has decreased to 1.46 W. Although this is still greater than the performance threshold of 1.4 W, the percentage of outcomes that meet or exceed the threshold is 64%; i.e., the system fails to satisfy the performance requirement for a significant portion of outcomes. While the design performs very well without uncertainty, it is unreliable (due to its low feasibility) under this model of uncertainty.

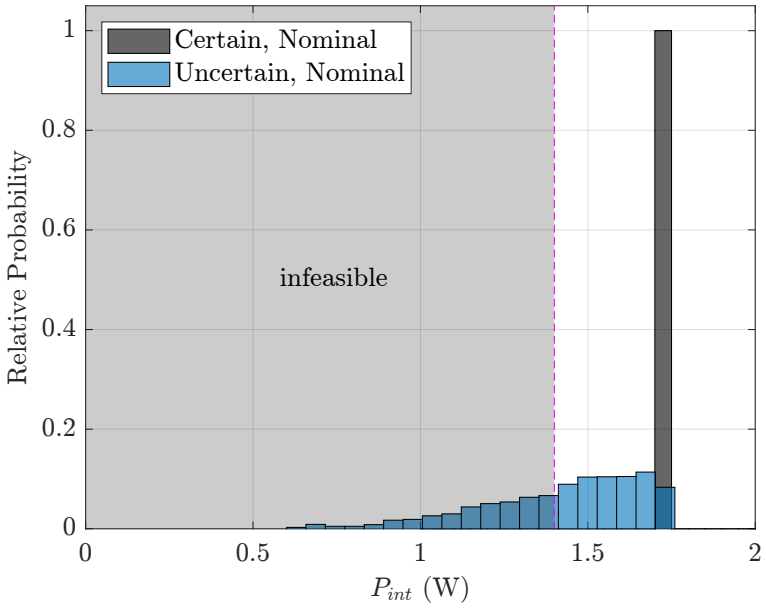

Figure 3-7: Distribution of nominal power performance outcomes under no uncertainty (black), and under modeled uncertainty (blue). Performance varies widely and degrades with the addition of uncertainty.

Optimization performed without consideration of uncertainty may yield results that are impractical for the real world. Whereas nominal performance without uncertainty is high, this is only guaranteed in the absence of uncertainty. Therefore the nominal performance outcome may not reliably meet requirements as observed

in the simplified WaferSat example. Other techniques are required to provide high performance with a high probability of feasibility.

3.4 Static Robust Optimization

Solutions that are only optimal and feasible in the no uncertainty case are not necessarily useful in reality where there is uncertainty. In constrained optimization, the set of active constraints are tight (i.e., the constraints are met at equality, the edge of satisfaction), and therefore offer no margin against variance in outcomes. One approach to mitigating the effects of uncertainty is to provide sufficient margin in the needed areas to account for worst-case outcomes under uncertainty.

3.4.1 Static Tailoring for Static Robustness

The original nominal optimization approach is expanded to include an additional loop to feed statistical information on the distribution of uncertain SoTW back to the optimizer as new constraints as shown in Figure 3-8. As an example, the new criteria may be for greater than n-σ statistical feasibility over the modeled uncertainty. The new constraints focus the optimizer search for designs that are both high-performing and tailored to provide an n-σ guarantee of feasibility. Designs such as the nominal optimal are discarded due to their low feasibility.

To identify designs that are statically robust, designs must be filtered for a decreased net effect to the active constraints from the sources of uncertainty. This can be achieved either through a design that has some natural insensitivity to the uncertainty (i.e., absorbers of change [42]) or through the allocation of margin. This filtering is expressed in Equation 3.4 as a new set of constraints related to the probability measure of active constraint satisfaction. The probability measure of active constraint satisfaction, $\mathbb{P}_{feas}$ is the probability that all constraints are met

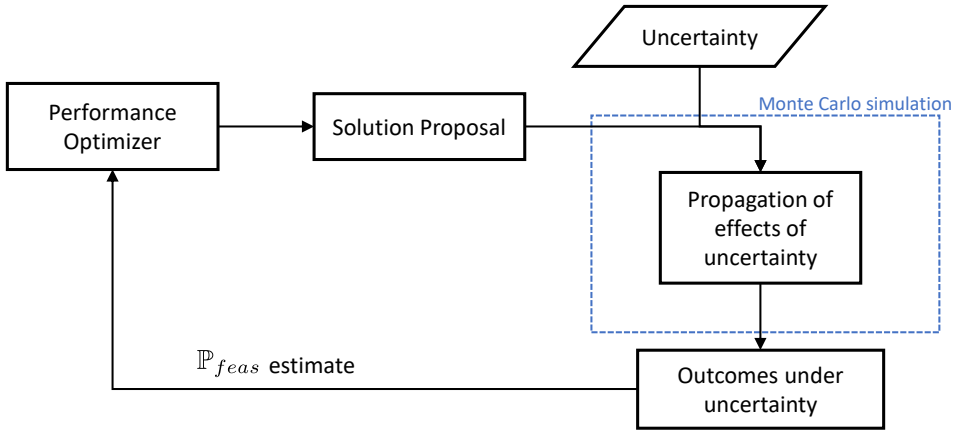

Figure 3-8: Feasibility results over the distribution of outcomes are sent back to the optimizer as new constraints, guiding the optimizer towards designs that are performance optimal *with* sufficient static margin

under modeled uncertainty. The distribution of outcomes in the constraint-space are evaluated for feasibility and fed back as augmenting constraints to the optimizer. Note that the active constraints in $\mathbf{c}$ and $\mathbf{c}_{eq}$ remain in the formulation, but only apply to the outer loop in the absence of uncertainty. The constraint functions $\mathbf{c}$ and $\mathbf{c}_{eq}$ are evaluated over the nominal, no uncertainty case, before the sampling from the uncertain ensemble. As such, these constraints now only enforce active constraint feasibility of the nominal state. The new augmenting constraint applies to the uncertain evaluations.

$$\begin{aligned} \max_{\mathbf{v}_s} \quad & P_{erf} \\ \text{s.t.} \quad & \mathbf{c}(x) \leqslant 0 \\ & \mathbf{c}_{eq}(y) = 0 \\ & \mathbb{P}_{feas} \geqslant \mathbb{P}_{feas}^{req} \end{aligned} \tag{3.4}$$

By setting some statistical feasibility criteria for the optimizer, the magnitudes of static margin are allocated as needed. When evaluated over an ensemble of uncertain

outcomes, generated from the uncertainty distribution, the n-σ bounds on the outcomes can be estimated. A desired n-σ level of feasibility is used as an augmenting criteria for the optimizer. For each nominal solution proposal, the estimated feasibility over the uncertain ensemble is then evaluated against the feasibility criteria. This focuses the search in the optimizer design towards solutions that provide the requisite statistical feasibility in addition to performance. In design with only static variables, desensitization of the active constraints is achieved with static margin. In this process, static tailoring optimizes the static variables for the original performance objectives while allocating the requisite static margin to meet the feasibility criteria.

The method for evaluating the active constraint probability of feasibility will be discussed using the simplified WaferSat example in the next section.

3.4.2 WaferSat Example: Optimizing for Static Robustness

As observed in the nominal optimal WaferSat scenario from § 3.3.3, the optimal solution occurs when the temperature constraints are tight, i.e., the temperature extremes in quasi-steady state meet the temperature requirements at equality. Designs that contain margin against the constraints in the zero uncertainty case can improve feasibility when uncertainty is introduced by allowing some room for extreme temperatures to increase or decrease and still remain within the constraints.

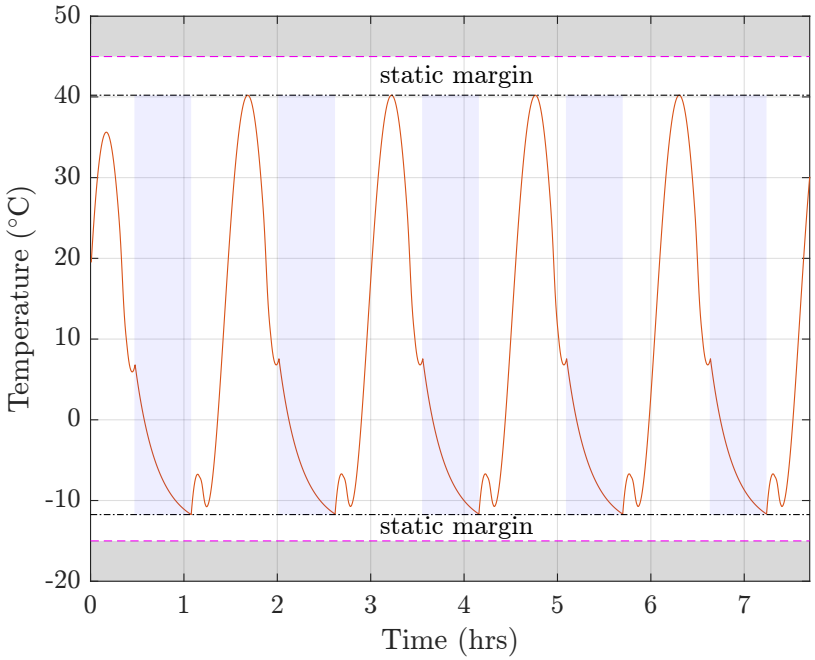

Figure 3-9: Static Robust design with static margin against the active temperature constraints in the zero uncertainty scenario

The optimization formulation is a modified version of Equation 3.2, augmented with an additional statistical feasibility constraint, shown in Equation 3.5. The probability measure of thermal requirement satisfaction, $\mathbb{P}_{feas}$ must be greater than

some required probability measure (e.g., for 2-σ, $P_{feas}^{req} = 0.954$).

$$\begin{aligned}
\max_{\mathbf{v}_s} \quad & \min\{P_{int}^{s}, P_{int}^{e}\} \\
\text{s.t.} \quad & T_{min} \geqslant T_{min}^{req} \\
& T_{max} \leqslant T_{max}^{req} \\
& 0 \leqslant \int_0^{2\pi} P_{SA} d\theta - \int_0^{2\pi} P_{int}(\theta) d\theta \\
& f_{SA} \leqslant 0.75 \\
& P_{int}^{e} \geqslant 1.4 \\
& P_{int}^{s} \geqslant 1.4 \\
& \mathbb{P}_{feas} \geqslant \mathbb{P}_{feas}^{req}
\end{aligned} \tag{3.5}$$

The probability measure, $\mathbb{P}_{feas}$ is the probability that both temperature constraints are satisfied under uncertainty, as expressed in Equation 3.6. This corresponds to the right-hand portion of the loop in Figure 3-8 where the temperature extremes are evaluated under uncertain SoTW. Note that this is distinct from the first two constraints of Equation 3.5 which enforce feasibility of the nominal, no uncertainty evaluation of the candidate solution.

$$\mathbb{P}_{feas} = \mathbb{P}\left(T_{min} \geqslant T_{min}^{req} \cap T_{max} \leqslant T_{max}^{req}\right) \tag{3.6}$$

In the right half of Figure 3-8, the true probability measure, $\mathbb{P}_{feas}$ is approximated using Monte Carlo sampling of outcomes under the uncertainty distribution. The approximation is expressed as the expected value of the feasible states, X under the probability space being evaluated, $\mathcal{P}_f$ (i.e., a probability space defined through evaluation of the thermal-power model, subject to the modeled uncertainty). In practice, the probability measure is estimated using importance sampling of individual SoTW that meet the temperature requirements over the modeled uncertain ensemble of size p, as expressed in Equation 3.7. The weight of the importance sampling is defined by an indicator function given in Equation 3.8 which checks for temperature

constraint satisfaction (the active constraint set) at each uncertain SoTW evaluation.

$$\mathbb{P}_{feas} \approx \mathbb{E}[X; \mathcal{P}_f] = \frac{1}{p} \sum_{1}^{p} x_i; \quad x_i \sim \mathcal{P}_f \tag{3.7}$$

$$x_i = \begin{cases} 1, & T_{min} \geqslant T_{min}^{req} \cap T_{max} \leqslant T_{max}^{req} \\ 0, & \text{otherwise} \end{cases} \tag{3.8}$$

An example of a robust design with 85% feasibility is shown in Figure 3-9. The temperature profile follows a similar general shape to that of the nominal optimal design, but with static margin allocated to both the maximum and minimum temperature requirements. Note that the optimizer allocated different magnitudes of static margin for the maximum and minimum temperature requirements. In this example, this allocation asymmetry is likely due to the differences in heat variance in the sunlit and eclipse portions of the orbit as well as the nadir-side radiative proportionality to T^4.

A static robust design is identified through static tailoring for 85% feasibility under the modeled uncertainty. A histogram of outcomes (orange) is shown in Figure 3-10 with a comparison to the nominal optimal solution under uncertainty (blue from Figure 3-7). Nearly 70% of outcomes in the static robust design under uncertainty occur within the tailored static margin (the largest histogram bin in orange). Power performance begins degrading after the static margin is consumed (in larger uncertain deviations in the tails of the uncertainty distribution). As a result, the new expected value of power performance under uncertainty is 1.51 W and 85% of outcomes are feasible. Note however, that the best case (nominal case) power performance is 1.63 W, less than the best power performance of the nominal optimal design.

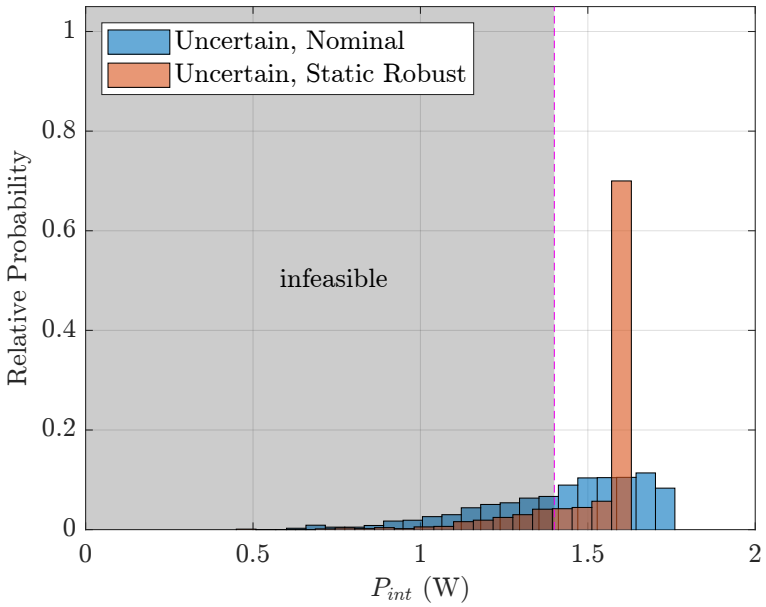

Figure 3-10: Distribution of nominal outcomes and statically robust outcomes under modeled uncertainty

In the static robust design, margin is allocated against the temperature constraints, increasing the percentage of outcomes that remain thermally feasible under modeled uncertainty. However, there is a tradeoff, as the maximum performance level of 1.83 W achieved by the nominal optimal design (under no uncertainty) is lost.

3.4.3 Nominal Performance & Static Robustness: Pick One

Providing feasibility guarantees using static margin for the active constraints comes at a cost. Optimization with static margin improves feasibility in the worst cases at the expense of performance [21]; this is often referred to as 'the price of robustness'. By effectively decreasing the size of the feasible space, the designs identified provide some guarantee of feasibility through a buffer against the active constraint-space. However, the decrease in the searchable feasible space (to allow for margin against active constraints) creates a more constrained problem, resulting in lower optimal performance. This exchange of optimality for reliability is often accepted because the

nominal optimal solutions are simply unrealistic under uncertainty and the robust sacrifice is seemingly the maximum guaranteed performance.

However, when the system at hand is severely limited in SWaP, such as WaferSat, the sacrifice in performance may be substantial. It may be useful to instead seek designs that may offer another route to improved feasibility with a smaller performance decrease. A method is needed that does not require a tradeoff between optimality and robustness.

3.5 Responsive Robust Optimization

Design for responsive robustness involves dynamic behavior of the uncertainty mitigation mechanism during operation. In this chapter thus far, all design has occurred over static variables; in order to elicit dynamic behavior in operation, dynamic variables must be included in the a priori design. In this section, the method for responsive tailoring is presented, including an expansion of the simplified WaferSat example problem. A new design variant with a passive response to uncertain states using phase change materials (PCM) is used to improve thermal feasibility. The behavior of the PCM is tailored during the design process, but the response cannot be changed in operation.

3.5.1 Responsive Tailoring

Responsive tailoring follows a similar process to that outlined in Figure 3-8. However, the responsive tailoring specifically occurs over a new dynamic variable set. For a given responsive mitigation, there is a set of design decisions that must be made during the a priori phase that will define the responsive behavior on orbit. Since the response is set during the a priori phase, the behavior in operation is described as fixed-recourse; the responding dynamic behavior cannot be reprogrammed.

During the design loop in Figure 3-8, model propagation over the ensemble of uncertain states allows for assessment of each candidate design. The feedback of the statistical feasibility criteria guides the search in defining the characteristics of the response (the responsive tailoring process), while maintaining the max performance search objective of the outer loop. This process follows the same optimization formulation as in Equation 3.5, however, during the model evaluations over the uncertain ensemble, the responsive behavior is propagated. The resultant responsive margin afforded by the responsive tailoring process will increase the probability of feasibility.

The general form of the optimization formulation in Equation 3.9 is similar to that in the static robust formulation. The optimization occurs over a new dynamic, responsive variable set, $\mathbf{v}_d^r$ in addition to the original static variable set, $\mathbf{v}_s$. The responsive variable set will govern the response to uncertainty that is modeled for each uncertain SoTW. During model evaluations under uncertainty, the dynamic behavior responds to the thermal conditions. Therefore the outcomes under uncertainty are distinct from those in a non-responsive scenario.

$$\begin{aligned} \max_{\mathbf{v}_s,\, \mathbf{v}_d^r} \quad & P_{erf} \\ \text{s.t.} \quad & \mathbf{c}(x) \leqslant 0 \\ & \mathbf{c}_{eq}(y) = 0 \\ & \mathbb{P}_{feas} \geqslant \mathbb{P}_{feas}^{req} \end{aligned} \tag{3.9}$$

An example responsive robust design will now be presented using phase change materials in WaferSat. The absorption and emission of heat during phase changes creates a responsive buffer: the responsive margin.

3.5.2 Phase Change Materials: Responsive Heat Storage

One example of a responsive robust thermal mitigation is phase change materials (PCM). Heat storage in materials can occur in several ways. Storage of heat with an associated rise in temperature - sensible heat storage - comprises the bulk of material heat capacity. However, during a phase transition, heat is transferred in or out of the PCM mass at constant temperature. This latent heat storage offers a region of mass-effective heat capacity without a change in temperature.

Implementation of PCMs requires material selection and mass/volume allocation in the a priori design phase. The response is realized in the a posteriori phase, where the solid/liquid fraction acts in response to system single-node temperature and heat flux. Modeling and operation of PCMs will be discussed in greater detail in § 4.4.1.

Usage of PCMs introduces the new dynamic responsive variable set, $\mathbf{v}_d^r$ defined in Equation 3.10 where T_c denotes the temperature of phase change, H_c° denotes latent enthalpy of phase change, and c_p^{pcm} denotes the sensible specific heat capacity of the PCM. In practice, these variables may be correlated through the PCM material selection (or mass-weighted sum combinations of different materials).

$$\mathbf{v}_d^r = \begin{bmatrix} T_c, & H_c^\circ, & c_p^{pcm}, & m_{pcm} \end{bmatrix}^T \tag{3.10}$$

Selection of these variables, specifically the phase change temperature and latent enthalpy of phase change, will determine the corresponding response in the evaluations under uncertain SoTW. Note that each responsive mitigation included will expand this dynamic variable set.

3.5.3 WaferSat Example: Application of PCM

The simplified WaferSat example can be optimized to include some PCM mass in order to improve feasibility in the presence of uncertainty. In order to provide a fair

comparison at constant total system mass, it is assumed that any PCM added to the WaferSat displaces the equivalent mass of silicon substrate. Similar to the static robust design of § 3.4.2, a target statistical feasibility of 85% is set in the optimizer; this appears as the last, augmenting constraint of Equation 3.11. Furthermore, the addition of PCM as a responsive mitigation introduces the dynamic responsive variable set, $\mathbf{v}_d^r$.

$$\begin{aligned}
\max_{\mathbf{v}_s, \mathbf{v}_d^r} \quad & \min\{P_{int}^s, P_{int}^e\} \\
\text{s.t.} \quad & T_{min} \geqslant T_{min}^{req} \\
& T_{max} \leqslant T_{max}^{req} \\
& 0 \leqslant \int_0^{2\pi} P_{SA} d\theta - \int_0^{2\pi} P_{int}(\theta) d\theta \\
& f_{SA} \leqslant 0.75 \\
& P_{int}^e \geqslant 1.4 \\
& P_{int}^s \geqslant 1.4 \\
& P_{feas} \geqslant P_{feas}^{req}
\end{aligned} \tag{3.11}$$

The temperature profile of the resulting responsive design is shown in Figure 3-11. The allocation of PCM mass creates responsive margin against the active constraints. Note that the relative allocation of responsive margin bears similarity to that of the static margin in § 3.4.2; a greater proportion of margin is dedicated to the maximum temperature constraint.

The regions of constant temperature can be viewed during heating and cooling through the phase transition temperature of 288 K (15 °C). The isotemperature regions effectively lengthen the thermal time constants. The behavior is dynamic, responding to variances in heat flow for each uncertain SoTW. The result of this behavior is responsive margin against the temperature constraints. Note that in this design, the maximum performance is approximately equal to that in the nominal

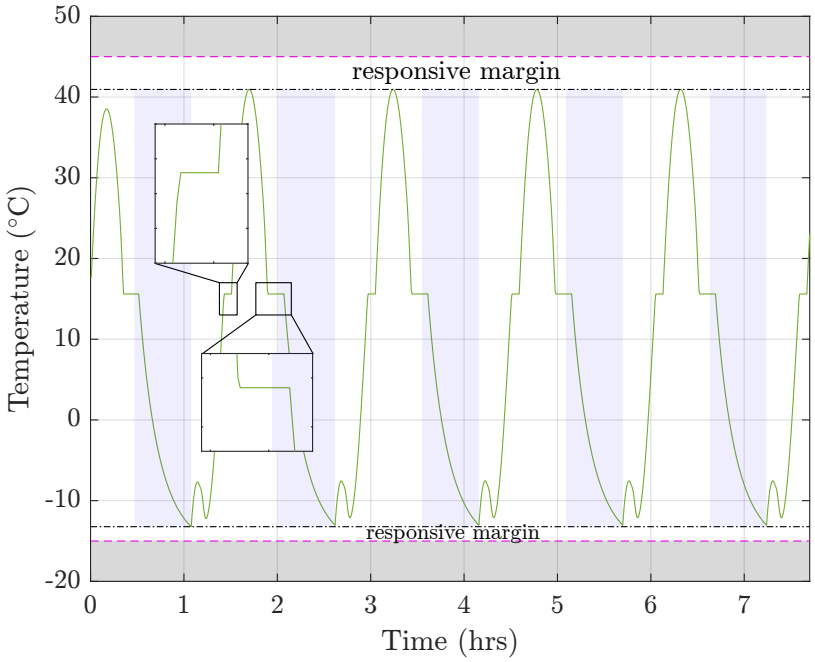

Figure 3-11: Responsive robust single-node temperatures in the zero uncertainty case. Isotemperature regions during cooling and heating through the phase transition point lengthen the effective thermal time constants.

optimal design at 1.74 W.

Two dynamic variables were optimized during the responsive tailoring process: total PCM mass and temperature of fusion (or phase transition temperature). In this example, for simplicity, the sensible heat storage of the PCM was ignored. The phase transition temperature or temperature at which latent heat is stored or released determines the temperature of the phase transition (storage or release of latent heat). The optimal value of phase transition of 288 K or 15°C places the phase transition right at the period of nadir-side heating at the start of eclipse. The result is non-monotonic heat flows into the system and PCM during the phase transition. The solid-liquid response as a function of time is shown in Figure 3-12 during the freezing phase transition (the same time period as the second inset of Figure 3-11). The period of nadir-side solar illumination results in the non-monotonic behavior; as the nadir-side is heated at dusk, the PCM partially re-melts, prolonging the period of isothermal phase transition. The result is a greater effectiveness of the PCM mass in

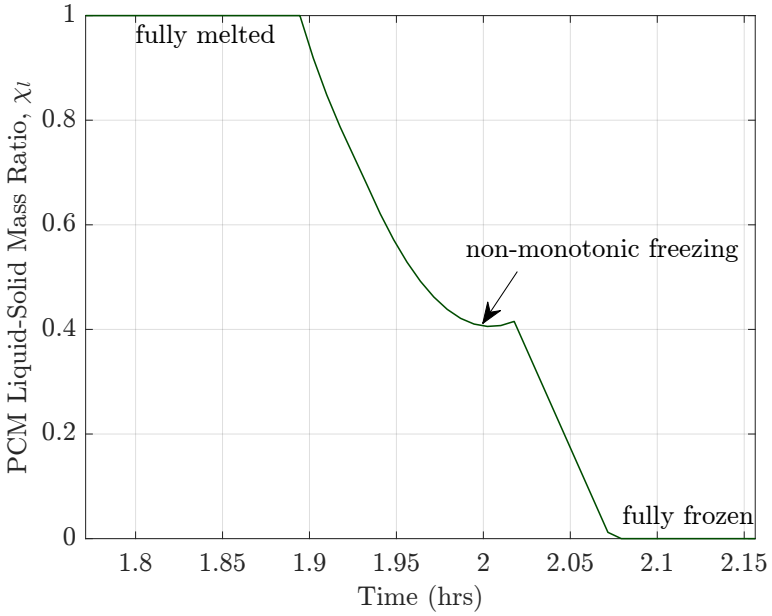

Figure 3-12: Liquid mass ratio during phase transition during cooling at dusk

lengthening the thermal time constant. Selection of a phase transition temperature near the middle of the temperature oscillation range also has a balancing effect on the distribution of responsive margin near the maximum and minimum requirements.

A histogram of power performance under uncertainty is shown in Figure 3-13. Feasibility is improved, to meet the target 85% of outcomes meeting the performance threshold. The expected value of performance of 1.59 W is also higher than that in the static robust solution (1.51 W).

One particular advantage of responsive robustness is the passivity of the fixed-recourse response. Once the dynamic variables have been set during the a priori phase, no further control is necessary - the response to uncertanity occurs automatically (e.g., PCMs melt and freeze as heat flows in and out). This does however, also present a downside: the response to uncertainty is unchangeable in operation. Responsive tailoring relies heavily on the uncertainty model used in the tailoring process. The final method, adaptive optimization, presents an additional alternative with the ability to actively compensate for uncertainty.

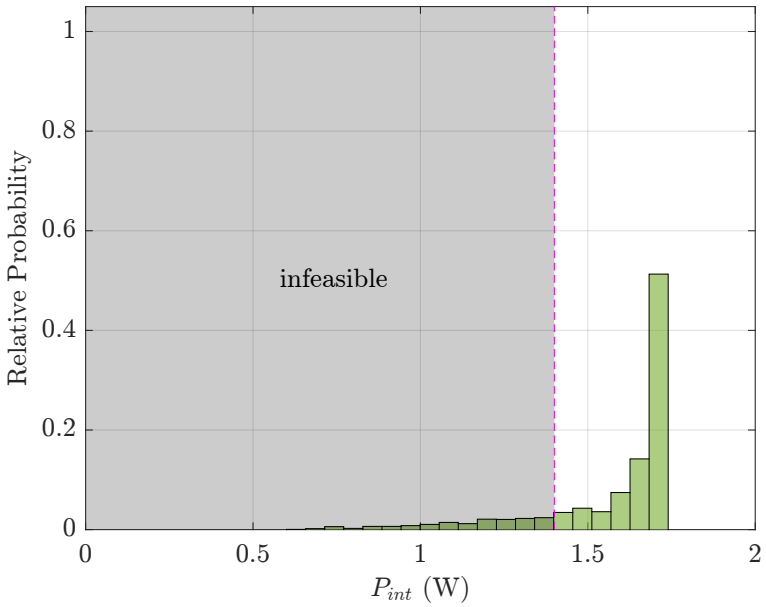

Figure 3-13: A histogram of responsive robust power performance outcomes under the modeled uncertainty.

3.6 Adaptive Optimization

Optimization for adaptivity involves optimization during both the a priori and the a posteriori phases. Like the responsive tailoring, there is a set of dynamic variables that will govern the behavior in operation. In the a posteriori phase, the adaptive variables are optimized for compensation of the effects of uncertainty, i.e., the adaptive behavior is actively optimized for realizations of uncertainty. This process occurs in two stages: adaptive tailoring of the dynamic variables and tuning of adaptive variables in operation.

3.6.1 Design for Adaptability & Adapting to Uncertainty

The expanded two-stage process for adaptive tailoring and tuning is shown in Figure 3-14. In the outer loop, adaptive tailoring over a new set of dynamic variables that govern the adaptive mitigation are optimized. For each solution proposal within the

MC simulation block (blue dashed lines), an inner loop tuning optimization designs for minimum variance of the uncertain solutions. Note that this inner loop optimization is dynamically constrained by the dynamic variables set during the adaptive tailoring phase.

Feedback of the tuned distribution of outcomes is used in the outer loop to evaluate the statistical feasibility. In this way, the desired level of tuneability is designed in during the a priori phase, and the optimal response to the modeled uncertainty is realized in the inner loop.

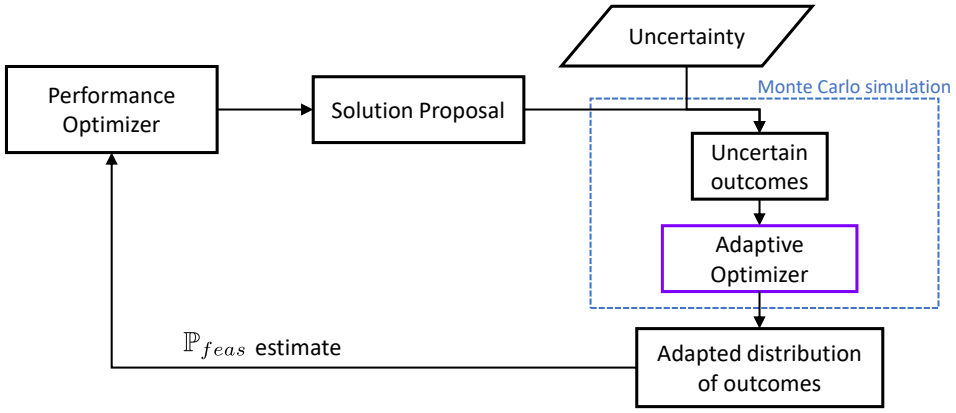

Figure 3-14: Two-stage optimization: adaptive tailoring of dynamic variables to govern and constrain adaptive behavior, tuning optimization to determine optimal tuned response to uncertain SoTW

The outer and inner loops of optimization are expressed in Equations 3.12 and 3.13 respectively. The outer loop optimization now includes the dynamic adaptive variable set, $\mathbf{v}_d^a$, the governing set of variables for adaptive behavior. The objective of the inner loop is to maximize the probability of feasibility of the active constraint set, $\mathbb{P}_{feas}$. This occurs over the adaptive variable set, $\mathbf{v}_a$, which is subject to decisions made in the outer loop. The adaptive constraint function, $\mathbf{c}_a$ is also subject to the variables in $\mathbf{v}_d^a$. Therefore, the inner loop optimization defines the optimal tuning behavior in compensation for uncertain SoTW to maximize the feasible outcomes.

$$\begin{aligned} \max_{\mathbf{v}_s, \mathbf{v}_d^r, \mathbf{v}_d^a} \quad & P_{erf} \\ \text{s.t.} \quad & \mathbf{c}(x) \leqslant 0 \\ & \mathbf{c}_{eq}(y) = 0 \\ & \mathbb{P}_{feas} \geqslant \mathbb{P}_{feas}^{req} \end{aligned} \tag{3.12}$$

$$\begin{aligned} \max_{\mathbf{v}_a} \quad & \mathbb{P}_{feas} \\ \text{s.t.} \quad & \mathbf{c}_a(z, \mathbf{v}_d^a) \leqslant 0 \end{aligned} \tag{3.13}$$

The two stage process for the design of adaptability can be broken down with two segments. In the a priori design phase, the design for adaptability controls how much tuneability is available. In the a posteriori operations phase, design of the adaptability produces the ideal, active mitigation of uncertainty.

3.6.2 WaferSat Example: Adaptive Electrochromics

An example of adaptability using dynamically selectable emissivity surfaces - electrochromics - is used to illustrate adaptive mitigation of uncertainty. Dedication of some WaferSat surface area to electrochromic surface allows for compensation of errors in the static emissivity coatings of other surfaces. A simple 2-element nadir surface is shown in Figure 3-15. The static surface consists of a target emissivity, ε_N and an uncertain perturbation δ. The adaptive portion of the surface consists of electrochromic area selectable over a continuous range, $\varepsilon_E \in [0.2, 0.8]$. In this example, allocation of the area to electrochromics is set through adaptive tailoring, and the optimal selection of compensating emissivity during operation is set through tuning.

For an electrochromic fractional fill factor, β_E, the effective emissivity is given as

$$\varepsilon_{Neff} = \beta_E \varepsilon_E + (1 - \beta_E)(\varepsilon_N + \delta) \tag{3.14}$$

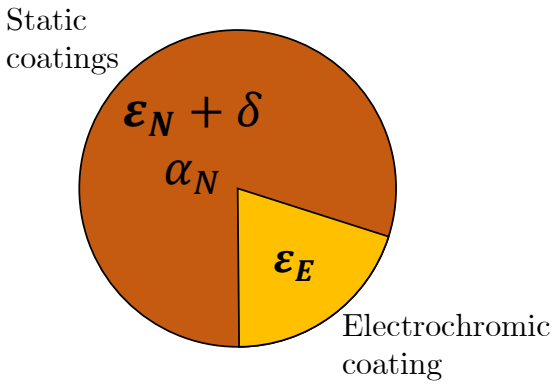

Figure 3-15: Diagram of nadir surface and thermal properties

A value of 0.5 is assigned for the nominal value of the electrochromic surface, ε_E^{nom}. This allows for even compensatory range before saturation at the electrochromic limits. The electrochromic area fill factor, β_E is optimized as part of the adaptive tailoring process. The uncertain perturbing factor, δ is sampled from the distribution introduced in § 3.3.3.

In general, the inner loop optimization objective is to maximize feasibility under modeled uncertain conditions. For simplicity and improved computational speed, a minimum variance optimization heuristic can be applied as expressed in Equation 3.15. The emissivity tuning objective is formulated to minimize the difference between the realized uncertainty and the original nominal target, ε_N. This has the effect of returning the uncertain realizations back to the nominal state (or as closely as is possible). The electrochromics are assumed to be continuously commandable over the range from 0.2 to 0.8 (indicated by the constraints of Equation 3.15).

$$\begin{aligned} \min_{\varepsilon_E} \quad & |\varepsilon_N - [\beta_E \varepsilon_E + (1-\beta_E)(\varepsilon_N + \delta)]| \\ \text{s.t.} \quad & \varepsilon_E \leqslant 0.8 \\ & \varepsilon_E \geqslant 0.2 \end{aligned} \tag{3.15}$$

Since the perturbing uncertainty and the electrochromics act upon the same quantity, a simple, optimal decision rule can be derived. Note that the finite emissivity range

of the electrochromics presents three scenarios: exact compensation, saturation high, and saturation low, shown in Equation 3.16. In exact compensation (first case of Equation 3.16) there is an exact value of the electrochromics which reproduces the original target value of ε_N. The magnitude of uncertain emissivity perturbation that can be exactly compensated, C is a function of the electrochromic area allocated (and is set by decisions during adaptive tailoring) and is shown in Equation 3.17. In the two saturation cases (cases two and three of Equation 3.16) the effect of the uncertainty is mitigated, but is not completely compensated. The electrochromics are set to either the maximum or minimum possible value. In this optimization for a target 85% feasibility guarantee, the electrochromic area is tailored to cover 11% of the nadir surface area.

$$\varepsilon_E^* = f(\delta) = \begin{cases} (\varepsilon_N + \delta) - \frac{\delta}{\beta_E}, & |\delta| \leqslant C \\ 0.8, & \delta > C \\ 0.2, & \delta < -C \end{cases} \tag{3.16}$$

$$C = \frac{\beta_E(0.5 - \varepsilon_E^{max})}{1 - \beta_E} = \frac{\beta_E(0.5 - \varepsilon_E^{min})}{1 - \beta_E} \tag{3.17}$$

Note that C is a common value for the range of positive and negative δ that is compensatable since the electrochromics are assumed to be nominally centered at 0.5 (the middle of the range). In other words, the electrochromics afford equal tuning authority for increases and decreases in heat. When the center of the electrochromics are not at the center of the range, the tuning authority can become asymmetric; this will be explored later in Chapter 4.

The unmitigated and adaptive realizations of ε_{Neff} are shown in Figure 3-16. The nominal target ε_N is marked with a dashed red line. The center, most-probable set of outcomes of the electrochromic adaptive histogram (purple) represents the exact compensation cases, where the electrochromic surface is able to maintain the target effective emissivity. The left and right tails of the histogram represent the saturation

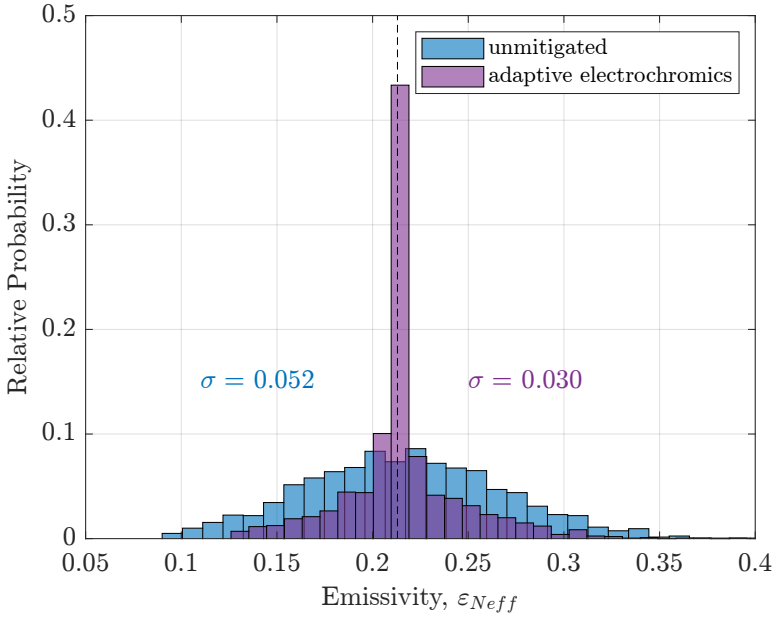

Figure 3-16: A comparison of the unmitigated and electrochromic adaptive distributions of ε_{Neff}

low and high cases, respectively. The result is a marked reduction in the effective emissivity variance from 0.05 to 0.02 and in about 45% of outcomes, the nominal condition is exactly produced.

In this example, there is also a secondary mitigating effect of adding electrochromic area due to the replacement of static surface area with electrochromics. As the ratio of electrochromic area increases, the total amount of uncertain static area decreases. However, in this example, the decrease in net temperature variance due to the reduction of static coated area is small. An additional set of histograms with a comparison of the variance is shown in Figure 3-17. The blue histogram shows the original, nominal solution variance of the uncertain effective nadir emissivity with variance 0.052 (labeled as unmitigated). The grey histogram shows the variance of the effective nadir emissivity with the adaptively tailored 11% nadir surface area coverage, but with the electrochromics inactive - with emissivity value always set to 0.5. There is little change to the distribution of outcomes, compared to the decrease once the electrochromics are adaptively tuned (Figure 3-16).

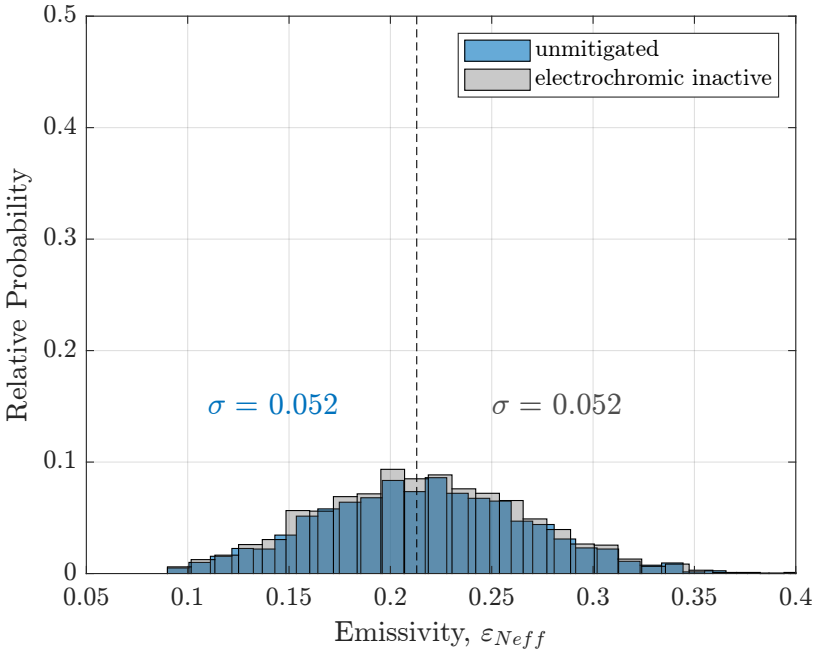

Figure 3-17: A comparison of emissivity outcomes for the unmitigated case in blue and inactive electrochromics in gray. The inactive electrochromics are held at a value of 0.5 for all time.

A histogram of outcomes of power performance of the adaptive design is shown in Figure 3-18. The largest bin of power performance represents the exact compensation cases, where the nominal optimal power performance is realized, even under uncertainty. For larger uncertain perturbations, the electrochromics saturate (high or low) and power performance degrades (in the tails of the uncertain distribution). The expected values, probabilities of meeting the performance threshold, and maximum performance capability are summarized in Table 3.2 for all cases.

Table 3.2: Summary of expected values and probabilities of success

	Design	**Case**	$\mathbb{E}[P_{int}]$ (W)	$\mathbb{P}[P_{int} \geqslant 1.4]$	$\max(P_{int})$ (W)
	Nominal Optimal	Certain	1.74	1.00	1.74
	Nominal Optimal	Uncertain	1.46	0.64	1.74
	Static Robust	Uncertain	1.51	0.85	1.63
	Responsive Robust	Uncertain	1.59	0.85	1.74
	Adaptive	Uncertain	1.63	0.85	1.76

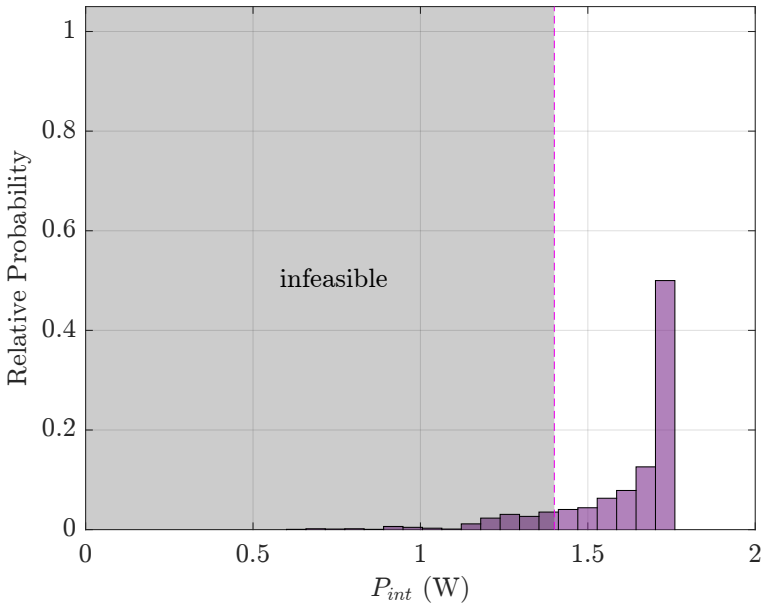

Figure 3-18: Distribution of adaptive optimal solution using electrochromic-mitigated ε_{Neff}

The expected values of power performance, probabilities of meeting the power performance threshold, and maximum power performance are summarized in Table 3.2 for all designs and uncertainty cases. The nominal optimal design appears to perform well under certain conditions. However, the assumed absence of uncertainty is unrealistically optimistic. The same nominal optimal design under uncertain conditions performs poorly in both expected value of performance and probability of constraint satisfaction. The static robust design increases the probability of feasibility to the target of 85%, but still has a low expected value and maximum performance. The responsive design is able to recover the maximum power performance whilst increasing the probability of feasibility to 85%. Furthermore, the expected value increases to 1.59 W. The adaptive design fares the best in all three categories. Interestingly, it has a higher maximum power performance than the nominal optimal design under certain conditions, suggesting that adaptive activity can potentially improve the nominal performance beyond that of the nominal optimal.

3.7 The Costs of Static Robustness, Responsive Robustness, Adaptability

As is noted often in Real Options Theory [87, 56], flexibility provides a way to hedge against uncertainty, but is not without 'cost.' This often is expressed as a literal monetary cost, but can be extended to the engineering design context to represent the design ramifications of decisions to include dynamic and/or adaptive variables including alternatives forgone.

In the WaferSat electrochromics example, the 'cost' may be expressed as an opportunity cost of surface usage. While the surface area to mass ratio of WaferSat is high in a relative sense, at the absolute scale, the total surface area is limited. Dedication of surface area to electrochromics must displace other uses of the wafer surfaces. Electrochromics area on the zenith surface reduces the total potential area of solar cells and other surface components (e.g., sensors, propulsion, communications). Therefore, a balance must be found between the surfaces devoted to adaptability (e.g., electrochromics) and to the nominal objective (e.g., electrical power generating area). If a balance cannot be found, other responsive or adaptive mitigations should be considered.

The fact that the limited resources and surface areas pit the nominal and adaptable objectives at odds with one another prevent the selection of a design that is maximally adaptable with every and all adaptable variables included as such a design may no longer satisfy the nominal design objectives. Therefore it may be useful to identify a set of isoperforming and isofeasble designs in order to search for the balance of robustness and adaptability that incurs an acceptable implementation cost for the mission at hand.

3.8 Summary

In this chapter, the methodology was presented, building up from traditional nominal and static robust optimization. It is shown through example that the traditional nominal optimization approaches under severe constraints do not yield reliable solutions under uncertainty. Conversely, the traditional robust approaches that rely on static margin sacrifice significant performance in pursuit of a feasibility guarantee. Responsive robustness is introduced with a statistical feasibility criteria, evaluated over a modeled uncertainty set. Tailoring of a priori dynamic variables define the response in operation, yielding designs that effect the desired, feasibility-increasing response in operation. Next, the adaptive approach is introduced, showing the two-step process of tailoring the dynamic adaptive variable set to optimize the tuning range relative to the range of uncertainty. Optimization over the uncertain states identifies the optimal tuning response to continuously changing states of uncertainty in operation.

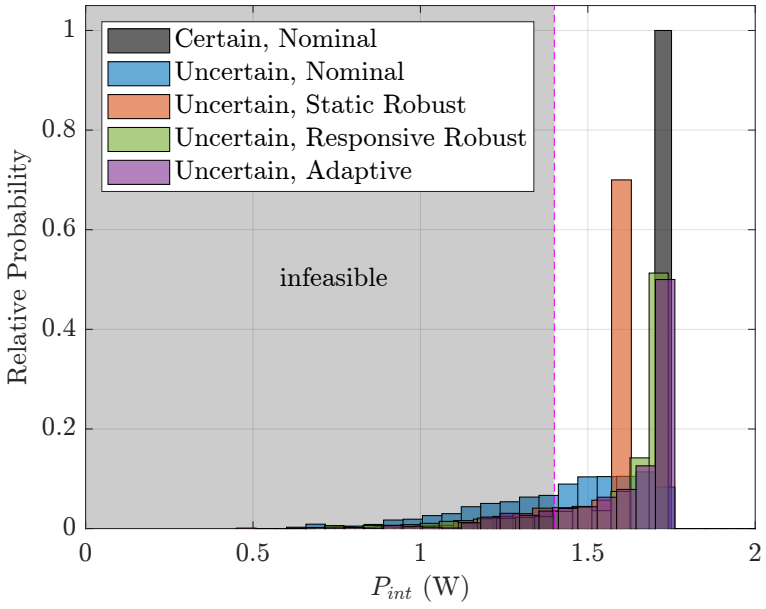

Figure 3-19: A comparison of histograms of performance outcomes under uncertainty for each individual mitigation method

A simplified WaferSat example problem was used to illustrate the improvements to

feasibility under a simple parametric uncertainty case. Static robustness, responsive robustness, and adaptability mitigations were presented in isolation to demonstrate unique methods to improve feasibility under uncertainty. A summary comparison of outcomes is presented together in Figure 3-19 and Table 3.2. Note that the responsive and adaptive designs result in both a greater expected performance under uncertainty as well as better nominal maximum performance. In other words, there is a smaller sacrifice of uncertainty in order to elicit the desired reliability under uncertainty.

In the following chapters, more complex examples that utilize and compare non-unique combinations of static robustness, responsive robustness, and adaptability will be presented.

Chapter 4

WaferSat

In this chapter, a more detailed version of the simplified WaferSat example from Chapter 3 is presented. This design example will incorporate more design variables in a more thermally constrained problem and will exercise the methodology through optimization of the simultaneous use of three responsive robust and adaptive mitigations. Through this problem, three unique balances of robustness and adaptability that produce the same level of performance and feasibility are identified and compared. Attainment of the same function with different form allows for more informed trades of different combinations of responsiveness and adaptability

4.1 Problem Definition

In this example, a 300 g WaferSat is in the same orbit as that defined in the simplified example from §3.2. The WaferSat is in a 400 km altitude orbit with solar β angle of zero. This orbit presents the most thermally restrictive scenario with maximum eclipse length and most direct solar exposure in the nadir-facing orientation. The WaferSat will first be nominally optimized for the nominal, zero uncertainty scenario.

4.1.1 Parameters & Static Design Variables

The description of the scenario is broken into three parts: definition of constant parameters, description of the set of static design variables, and the definition of the optimization. There are various constant parameters throughout the system. The parameters and values are summarized in Table 4.1. Although WaferSat will contain

Table 4.1: Constant parameters used throughout the WaferSat problem

Parameter	**Symbol**	**Value**	**Units**
WaferSat radius	r_{waf}	100	mm
WaferSat thickness	t_{waf}	4.1	mm
WaferSat mass	m_{waf}	300	g
Si density	ρ	2330	$\mathrm{kg\,m^{-3}}$
mean Earth bond albedo	A_E	0.31	-
mean Earth black body temperature	T_E	255	K
orbit altitude	h	400	km
solar array emissivity [37]	ε_{SA}	0.86	-
solar array absorptivity [37]	α_{SA}	0.92	-

many embedded components, it is assumed that the silicon substrate is the main mass component. As such, the properties of silicon are assumed to dominate in sizing and calculation of thermal mass.

The static design variable set includes the design of static surface thermo-optical coatings. This includes the zenith, nadir, and radial wall surfaces. The zenith and nadir surfaces include design parameters for the physical fill factor of solar array area as a percent coverage (nadir surfaces can generate power from Earth albedo-reflected sunlight). For the nominal problem, it is assumed that any surface area not occupied by solar arrays is coated with static thermo-optical coatings. This set of static design variables will be used for the nominal and static robust optimization approaches. When including responsive robustness and adaptability in the optimization, the variable sets will be augmented with dynamic and adaptive design variables (outlined in §4.4).

Table 4.2: Set of static design variables, $\mathbf{v}_s$

Static Design Variable	**Symbol**
zenith static emissivity	ε_z
zenith static absorptivity	α_z
nadir static emissivity	ε_n
nadir static absorptivity	α_n
radial wall static emissivity	ε_r
radial wall static absorptivity	α_r
zenith solar array physical fill factor	f_{SA}
nadir solar array physical fill factor	f_{SN}

WaferSat is severely limited in SWaP; as such, the optimization objective is to maximize internal power dissipation capability at all points in the orbit. All internal power dissipation is assumed to result in heating in WaferSat - a deleterious effect in the sun, but beneficial during eclipse. Maximized internal power available at all times to a payload enhances capability and reduces restrictions on when the payload can operate.

4.1.2 Constrained Optimization

Due to the high $\mathcal{AR}$ and short thermal time constants of the WaferSat system, it is anticipated that the temperature constraints may limit performance. A summary of the estimated temperature constraints of several subsystems of the WaferSat system are summarized in Table 4.3. The focus of the optimization will be for performance in operation, so the operational temperature limits will be considered. Note however, that the wider survival limits present another, non-operational option for survival of the system. The most temperature-constrained element will be the lithium titanate batteries. These temperature limits were tested in [88]. Although these batteries showed operation down to $-40\,^{\circ}\mathrm{C}$, the effective capacity suffered a greater than 20% loss under $-15\,^{\circ}\mathrm{C}$. The operational temperature requirements for WaferSat will be from $-15\,^{\circ}\mathrm{C}$ to $30\,^{\circ}\mathrm{C}$.

Table 4.3: General spacecraft subsystem temperature requirements [44, 89]

Component	**Operational** (°C)	**Survival** (°C)
Solar arrays	-150 to 110	-200 to 130
Lithium Titanate batteries [88]	-15 to 30	-40 to 45
Avionics	-20 to 60	-40 to 75
Electrospray propellant[90]	-20 to 70	-40 to 200
Antennas	-100 to 100	-120 to 120

The WaferSat system will use solar arrays to generate electrical power that is dissipated and stored in batteries. As an additional constraint, it will be assumed that over the course of each orbit, the total dissipated power is less than or equal to the total generated electrical power. This constraint allows for constant operation - there will not be a need to enter lower power states to recharge.

$$\begin{aligned} \max_{\mathbf{v}_s} \quad & P_{int} \\ \text{s.t.} \quad & T_{min} \geqslant T_{min}^{req} \\ & T_{max} \leqslant T_{max}^{req} \\ & 0 \leqslant \int_0^{2\pi} P_{SA} d\theta - \int_0^{2\pi} P_{int}(\theta) d\theta \\ & f_{SA} \leqslant 0.70 \\ & f_{SN} \leqslant 0.70 \end{aligned} \tag{4.1}$$

The nominal optimization is shown in Equation 4.1. The optimization objective will be to maximize the mean internal power P_{int} capability, using the static design variable set, $\mathbf{v}_s$. The temperature requirements constrain the extreme temperatures attained over the orbit in quasi-steady state. The maximum solar array physical fill factors are capped at 70% of the respective surfaces.

4.1.3 Thermal & Power Modeling

Modeling of thermal and power are performed in a coupled model. The defining equations and propagation method for this model are summarized.

Heat fluxes into and out of the WaferSat system drive changes in temperature. As shown in Equation 4.2, the derivative of thermal heat is the result of the net heat flows in (sources: Q_{source}) and out (sinks: Q_{sink}), and instantaneous internal power dissipation, P_{int}.

$$\frac{d}{dt}(mCpT_{waf}) = \Sigma Q_{net} = \Sigma Q_{source} + \Sigma Q_{sink} + P_{int} \tag{4.2}$$

There are many heat source terms, corresponding to unique heat sources incident upon distinct areas of the WaferSat. These heat source terms follow a similar format, given in Equation 4.3. Each heat source term from source 1 to surface 2, Q^{src}_{1-2}, is a function of a source flux density, E_{flux}, an effective area of incidence on surface 2, A_{inc}, and an absorptive modifier of surface 2, α_2.

$$Q^{src}_{1-2} = E_{flux} A_{inc} \alpha_2 \tag{4.3}$$

The combinations of heat sources are summarized in Table 4.4. Note that the columns of the table correspond to the terms in Equation 4.3. The subscripts of Q denote the heat and incident surface: $Q_{heatsrc-surface}$. The subscript indices are summarized in Table 4.5. The symbol $*$ refers to either any base letter or subscript.

Thermal radiation terms follow the format defined in Equation 4.4 where σ is the Stefan-Boltzmann constant, ε is the radiating surface emissivity, F_{1-2} is the thermal view factor from surface 1 to surface 2, A_1 is the radiating surface area, and T refers to the respective temperatures.

$$Q^{snk}_{1-2} = \sigma \varepsilon_1 F_{1-2} A_1 \left(T_1^4 - T_2^4\right) \tag{4.4}$$

Table 4.4: Incident Heat Source Terms

Source Term Q_{source}	**Source Flux Density** E_{flux}	**Area of Incidence** A_{inc}	**Absorptive Modifier** α
Q_{sol-SA}	E_{sol}	$A_{waf}F_{sol-SA}f_{SA}$	$\alpha_{SA} - \eta_{SA}$
Q_{sol-z}	E_{sol}	$A_{waf}F_{sol-z}\left(1 - f_{SA}\right)$	α_z
Q_{sol-n}	E_{sol}	$A_{waf}F_{sol-n}$	α_n
Q_{a-SA}	$a_E E_{sol}$	$A_{waf}F_{E-z}f_{SA}$	$\alpha_{SA} - \eta_{SA}$
Q_{a-z}	$a_E E_{sol}$	$A_{waf}F_{E-z}\left(1 - f_{SA}\right)$	α_z
Q_{a-n}	$a_E E_{sol}$	$A_{waf}F_{E-n}$	α_n
Q_{i-SA}	I_E	$A_{waf}F_{E-z}f_{SA}$	ε_{SA}
Q_{i-z}	I_E	$A_{waf}F_{E-z}\left(1 - f_{SA}\right)$	ε_z
Q_{i-n}	I_E	$A_{waf}F_{E-n}$	ε_n

The radiating term permutations are summarized in Table 4.6.

At thermal steady state, the net absorbed and radiated heats are equal. Equation 4.5 can be used to solve for steady state temperatures. Note that the steady state temperatures approximate a zero-mass system, which would exhibit instantaneous equilibration.

$$\Sigma \text{ heat source terms} = \Sigma \text{ radiation terms}|_{T_w} \tag{4.5}$$

The transient solution is solved numerically using a forward Euler scheme. Note that more complex integration schemes may be used, however forward Euler was selected as a strictly explicit forward solver in time. This is particularly beneficial when incorporating the thermally responsive and adaptive mitigation methods (since no implicit solving is required). The stability of the forward Euler scheme is verified with selection of time step size that is small enough to ensure bounded convergence on thermal steady state oscillation.

$$\left.\frac{dT}{dt}\right|_i \approx \frac{\Sigma \text{ heat source terms} - \Sigma \text{ radiation terms}|_{T_i}}{mc_p} \tag{4.6}$$

$$T_{i+1} \approx T_i + \left.\frac{dT}{dt}\right|_i \Delta t \tag{4.7}$$

Table 4.5: Summary of heat and radiation subscripts and symbols. The symbol $*$ refers to either any base letter or subscript.

Terms and Indices	**Definition**
$(*)_a$	albedo heat source
$(*)_n$	nadir surface
$(*)_{SA}$	zenith solar array
$(*)_{SN}$	nadir solar array
$(*)_{sol}$	sun term
$(*)_{waf}$	wafer surface area
$(*)_z$	zenith surface
A_*	area
a_E	effective Earth albedo
F_*	thermal view factor
f_*	physical fill factor
I_E	effective black body Earth IR

Emissivity and absorptivity, the non-dimensional coefficients on radiative emission and absorption of grey bodies (i.e., non idealized black bodies), are in reality, a continuous function of wavelength. Although these quantities may vary with wavelength, by Kirchoff's law of thermal radiation - shown in Equation 4.8 - for a given wavelength, all bodies absorb (denoted by α) and emit (denoted by ε) with the same coefficient quantity.

$$\varepsilon_\lambda = \alpha_\lambda \tag{4.8}$$

This work will utilize a common thermal modeling simplification wherein radiative wavelengths are considered in one of two 'bins': visible light, and mid-IR. There is a single radiative coefficient quantity for each wavelength bin. As a notational convention for distinguishing the wavelength bins, ε will always be used in reference to the radiative coefficient for the mid-IR bin and α will always be used for the visible light bin.

Each flat, circular surface of WaferSat has a 2π steradian (hemispherical) thermal view factor. Calculation of view factor from the Wafer to the Earth involves geometry of the scaled area of the Earth 'seen' by each surface. A depiction of the geometry is shown in Figure 4-1. The WaferSat is at an orbit radius r_o and the Earth is assumed

Table 4.6: Thermal Radiation Terms

Radiation Term Q_{rad}	**Radiating Area** A_{rad}	**Emissivity** ε	**Temp. 1** T_1	**Temp. 2** T_2
Q_{z-E}	$A_{waf}F_{z-E}(1-f_{SA})$	ε_z	T_{waf}	-
Q_{z-s}	$A_{waf}F_{z-s}(1-f_{SA})$	ε_z	T_{waf}	T_s
Q_{SA-E}	$A_{waf}F_{z-E}f_{SA}$	ε_{SA}	T_{waf}	-
Q_{SA-s}	$A_{waf}F_{z-s}f_{SA}$	ε_{SA}	T_{waf}	T_s
Q_{n-E}	$A_{waf}F_{n-E}(1-f_{SN})$	ε_n	T_{waf}	-
Q_{n-s}	$A_{waf}F_{n-s}(1-f_{SN})$	ε_n	T_{waf}	T_s
Q_{SN-E}	$A_{waf}F_{n-E}f_{SN}$	ε_{SN}	T_{waf}	-
Q_{SN-s}	$A_{waf}F_{n-s}f_{SN}$	ε_{SN}	T_{waf}	T_s
Q_{w-E}	$A_{waf}F_{w-E}$	ε_w	T_{waf}	-
Q_{w-s}	$A_{waf}F_{w-s}$	ε_w	T_{waf}	T_s

to be spherical with radius r_e. The WaferSat is depicted with an Earth angle of incidence, φ_i, or the angle between the nominally nadir-pointing surface normal and the WaferSat-Earth direction. This angle of incidence is a cone angle. The view

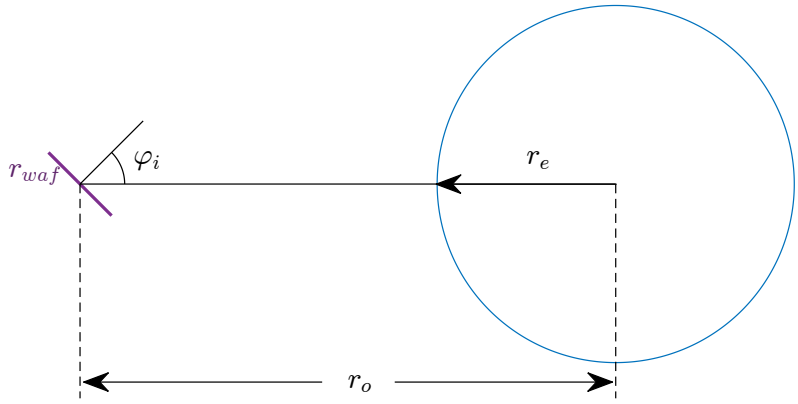

Figure 4-1: Diagram of disk to sphere for Equation 4.9 (not to scale for Wafer-Earth system)

factor to the Earth from the WaferSat nadir surface, F_{ne} is given in Equation 4.9 [91]. There are two distinct view factor states: when either one or both surfaces have a non-zero view factor to the Earth. The boundary between the states occurs when a projection along the edge of WaferSat is tangent to the edge of the Earth (when

$|\varphi_i| = \arccos\left(\frac{r_e}{r_o}\right)$). As the projection along the WaferSat edge traverses across the Earth (for increasing φ_i), both surfaces have a non-zero view factor to the Earth.

$$F_{ne} = \begin{cases} \frac{\cos(\varphi_i)}{x^2}, & |\varphi_i| \leqslant \arccos\left(\frac{1}{x}\right) \\ \frac{1}{\pi x^2}\left(\cos(\varphi_i)\arccos(z) - y\sin(\varphi_i)\sqrt{1-z^2}\right) & \\ \qquad + \frac{1}{\pi}\arctan\left(\frac{\sin\varphi_i\sqrt{1-z^2}}{y}\right), & |\varphi_i| > \arccos\left(\frac{1}{x}\right) \end{cases} \tag{4.9}$$

$$\text{for } x = \frac{r_o}{r_e}; \quad y = \sqrt{x^2-1}; \quad z = -x\cot(\varphi_i)$$

To calculate thermal view factors from the zenith surface to the Earth, F_{z-E}, Equation 4.9 is used with a new angle of incidence, $\pi - \varphi_i$.

Although WaferSat is a thin disk, the edges still account for approximately 5% of the total surface area and so must be accounted for. The calculation of the view factor to the Earth from the edge of WaferSat (assuming that WaferSat is a straight-walled, short cylinder) is shown in Equation 4.10 [92, 93] for the same angle of incidence, φ_i.

$$F_{se} = \int_0^{\arcsin\left(\frac{r_e}{r_o}\right)} \int_0^{2\pi} \frac{\sin(\vartheta)\sqrt{1-s^2}}{\pi^2} d\psi d\vartheta \tag{4.10}$$
$$\text{for } s = \cos(\vartheta)\cos(\varphi_i) + \sin(\vartheta)\sin(\varphi_i)\cos(\psi)$$

When the nadir surface normal angle of incidence, φ_i is zero (the nominal attitude), Equation 4.10 simplifies to the result in Equation 4.11.

$$F_{se} = \frac{1}{2} - \frac{u}{\pi x} - \frac{\arcsin(u)}{\pi} \tag{4.11}$$
$$\text{for } u = \sqrt{1 - \frac{1}{x^2}}$$

Note that Equations 4.9, 4.10, and 4.11 are valid when the disk radius and thickness are much smaller than the radius of the sphere, $r_{waf} \ll r_e$ and $t_{waf} \ll r_e$; this is a

reasonable assumption for virtually any size of WaferSat.

The power terms are given in Equation 4.12 where η_{SA} refers to the efficiency of the solar array and Γ refers to the solar incidence angle (the angle between the sunlight and the solar array surface normal). Electrical power generation is calculated for direct solar illumination and indirect Earth albedo illumination. Both terms include calculated including solar array area on the zenith and nadir surfaces.

$$P_{sol} = E_{sol}\eta_{SA}A_{waf}\left[f_{sa}\cos\left(\Gamma_{SA}\right) + f_{SN}\cos\left(\Gamma_{SN}\right)\right] \tag{4.12}$$

$$P_{alb} = a_E E_{sol}\eta_{SA}A_{waf}\left[F_{z-E}f_{sa}\cos\left(\Gamma_{SA}\right) + F_{n-E}f_{SN}\cos\left(\Gamma_{SN}\right)\right] \tag{4.13}$$

Electrical power can either be immediately dissipated or stored in batteries for later use. Therefore an internal power dissipation function, $P_{int}(\theta)$ is defined. Note that on a per-orbit basis, the system must be electrically power neutral. That is, the system cannot internally dissipate more or less than is generated.

$$\int_0^{2\pi} P_{sol}(\theta) + P_{alb}(\theta)d\theta = \int_0^{2\pi} P_{int}(\theta)d\theta \tag{4.14}$$

4.2 Modeling Parametric Uncertainty

The optimization process relies on evaluations of ensembles of modeled uncertainty to evaluate the statistical feasibility of designs. In this WaferSat problem, two realistic sources of uncertainty are used: local albedo and Earth IR variance.

4.2.1 Local Albedo

For traditional satellites of a low $\mathcal{R}$, Earth bond albedo, or reflected solar irradiance, is often considered as a bulk average term over the entirety of the surface of the Earth for most thermal modeling. For satellites with large $\mathcal{R}$ and a slow rate of thermal

equilibration, the local variation has little effect. Therefore, models need not account for the such variations.

As observed in §1.2.2, as satellite form factor transitions into the high $\mathcal{AR}$ regime, thermal time constants decrease, and the system approaches thermal equilibrium more quickly. Thus, local, transient variances in the net heat flows in and out of the system translate to large changes in temperature.

At a given point in orbit, the surface that faces the Earth has a thermal view factor to a local area of the surface of the Earth. Variations due to cloud cover and seasonal weather change the net albedo and therefore incoming nadir-side solar irradiance as the spacecraft flies over different regions of the Earth. Variance due to albedo depends on geometric angles from the solar irradiance direction, spacecraft position, and view of the Earth. Note that variance due to albedo has no effect during eclipse.

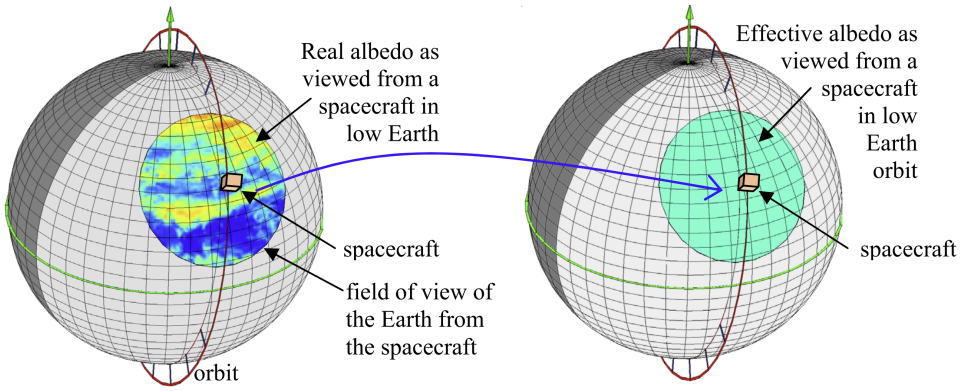

Figure 4-2: Comparison of view of Earth albedo from LEO spacecraft. Left: realistic local albedo distributions. Right: effective average constant [94]

The NASA Clouds and the Earth's Radiant Energy System (CERES) project has included measurements of local Earth albedo as viewed from LEO spacecraft. Through the CERES project, multiple spacecraft have mapped local albedo with variance estimates, resulting in estimated distributions of variance for some common LEO orbits [94, 95]. A comparison of the local albedo as viewed from a LEO spacecraft is shown in Figure 4-2 from [94]. On the left is a depiction of a realistic view of

locally varied albedo, compared to the traditional single-value average model method on the right. The effects of modeling with local variation for a high $\mathcal{AR}$ WaferSat are significant.

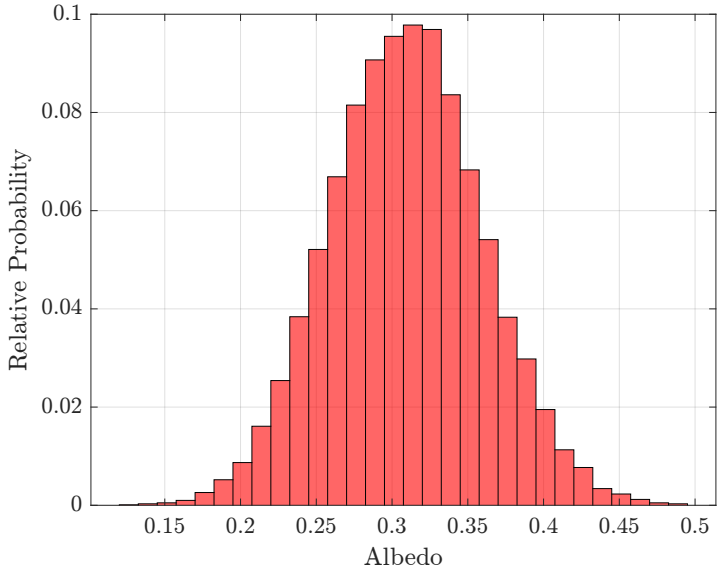

Figure 4-3: Distribution of local albedo using measured data from NASA CERES project

Modeling of local albedo uncertainty for the WaferSat example will draw upon the model from [94] for a 400 km circular orbit with inclination 51.6° (ISS orbit). The distribution is modeled as a Gaussian distribution with mean 0.31 and variance of 0.05, shown in Figure 4-3. Note that this model does not include the correlation between latitude and albedo.

4.2.2 Earth IR

Due to internal heat, the Earth emits IR radiation which can be approximated using the Earth black body temperature according to Equation 4.15. The total Earth IR heat flux, Q_{EIR}, is a function of the Earth black body temperature, T_e, the Stefan-Boltzmann constant, σ_{sb}, the orbit radius, r_o, and the radius of the Earth, r_E. Similar to the traditional modeling of albedo for larger satellites, the Earth black

body temperature is often considered to be a constant value. However, much like in the case with local albedo variation, the variances due to local changes in net Earth IR heat flux have an impact on temperature variance when $\mathcal{R}$ is high.

$$I_E = \sigma_{sb} T_e^4 \left(\frac{r_o^2}{r_E^2} \right) \tag{4.15}$$

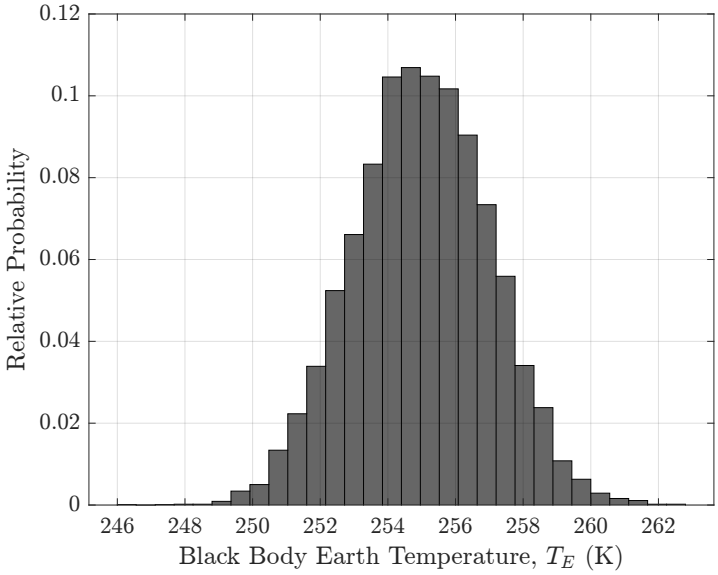

Figure 4-4: Estimated distribution of local Earth black body temperatures encountered by a satellite in LEO based on measured data from NOAA [96] and CERES projects [94]

There have been measurements and analyses of the Earth heat budget, including estimates of the incoming and Earth-radiated IR [97, 98]. Variation in local Earth black body temperature occurs on several time scales: longer seasonal time scales, as well as short time scales (less than the length of a LEO orbit). Measurements from the NOAA-9, NOAA-10 [96], and CERES missions [94] provide estimates of the distributions of local variation of Earth black body temperature encountered over single orbits in LEO. An estimate of the distribution of Earth black body temperatures encountered in the short period, over a single orbit in LEO. This distribution, for a 400 km, 51.6° inclination ISS orbit is shown in Figure 4-4.

4.2.3 High Æ Sensitivity to Local Uncertainty

To show the high sensitivity of WaferSat to realistic albedo and Earth IR variance in LEO, a comparison is made between two blank silicon wafers in LEO of different Æ. A scaled visual comparison of the two wafers is shown in Figure 4-5. The high aspect ratio wafer, in blue, has an Æ of 97.6, roughly equivalent to that of a 200 mm diameter WaferSat. The low aspect ratio wafer, grey, has an Æ of 2.27, so chosen to match one of the disk-to-cube similitude scalings of surface area to mass derived in §1.2.1. The low Æ wafer should have a similar surface area to mass thermal response to that of a 150 g Si cube.

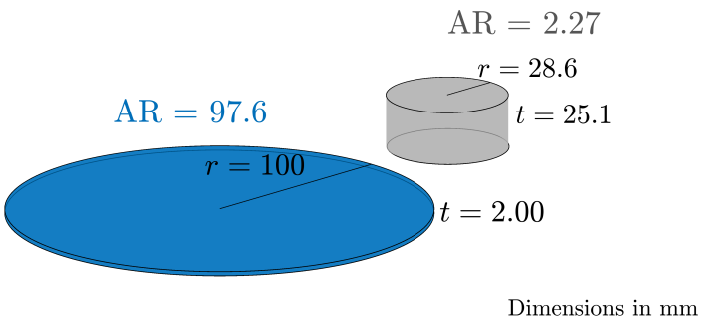

Figure 4-5: Scaled comparison of high and low Æ wafers

A comparison of the temperature variation is shown for the high and low Æ blank Si Wafers in Figure 4-6. All surfaces are assumed to have thermo-optical properties of bare silicon wafers: $\alpha = 0.73$, $\varepsilon = 0.7$. Both wafers are 150 g in mass and in a 400 km altitude orbit with a β angle of zero and one surface normal always nadir-facing.

Over the course of $n = 10^3$ Monte Carlo runs, the two orbiting wafers are modeled with uncertainty draws from the local Earth albedo and Earth IR distributions. The dashed lines represent the estimated 2σ variance over the course of the orbit. In addition to a general lower temperature sensitivity, the low Æ system has a much lower variance due to the modeled uncertainty. The high Æ wafer, by comparison, has a much more variable temperature in response to local uncertainties of both types.

Furthermore, the magnitudes of variance around the mean temperatures are large relative to the full range of temperature.

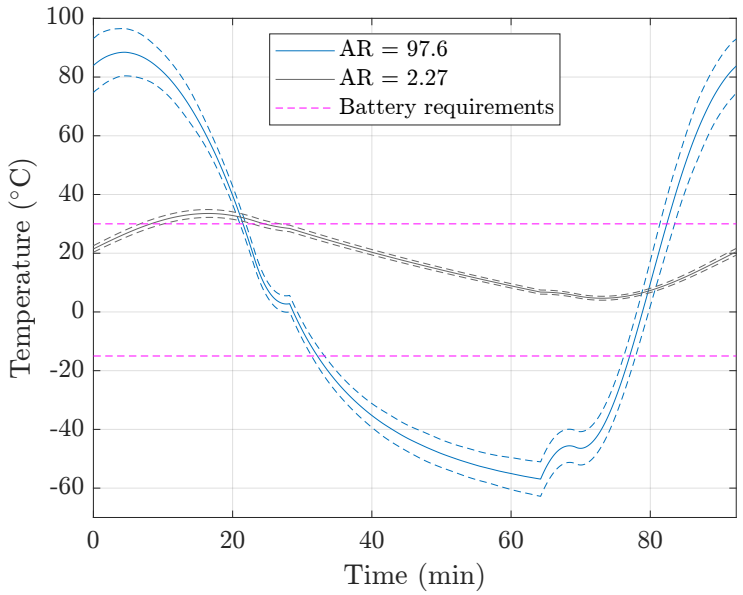

Figure 4-6: Mean temperatures (solid lines) over one orbit with 2σ variance (dashed lines) for a high $\mathcal{R}$ and low $\mathcal{R}$ blank Si wafer under local albedo and Earth IR uncertainty.

While this problem uses two sources of parametric uncertainty, more can be applied to create a more detailed model of uncertain outcomes. As will be shown later in § 4.6, optimization for uncertainty sources with different balances of responsive robustness and adaptability may yield differing levels of tolerance of error in the predicted uncertainty model used for optimization (i.e., robustness of robustness and robustness of adaptability for unknown unknowns).

4.3 Nominal & Robust Optimization

When optimizing for the nominal optimal, zero uncertainty scenario, a baseline performance level is established. The nominal optimal internal power dissipative capability is a continuous 1.15 W.

The active constraint-space is shown in Figure 4-7. The x-axis shows the minimum temperature in quasi-steady state and the y-axis shows the corresponding maximum temperature. The magenta dashed lines represent the temperature requirements. As in the simplified WaferSat case, at the nominal optimal solution, the two temperature constraints are active and performance-limiting (i.e., relaxation of these requirements would allow for an increase to performance). This is shown by the location of the nominal outcome, the red point, near the intersection of the temperature requirements, indicating that both are met at equality.

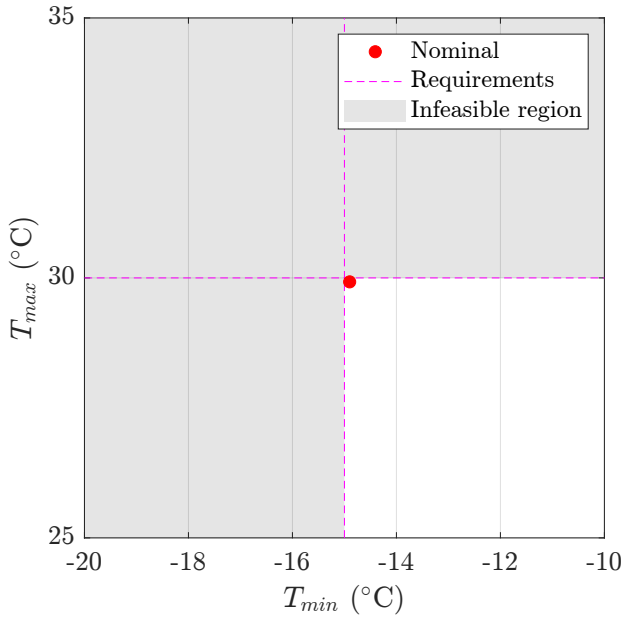

Figure 4-7: Nominal Optimal Solution, zero margin

4.3.1 The Nominal Optimal Design is Not Robust

The same nominal solution is shown again in Figure 4-8, this time modeled with an ensemble of uncertain states, drawing from the literature measurement-driven models of local albedo and local Earth IR uncertainty from §4.2. An estimated 2σ error ellipse is shown to bound the distribution. Under this uncertain scenario, the once guaranteed nominal outcome in the absence of uncertainty, is now only feasible

in 13.1% of the modeled outcomes.

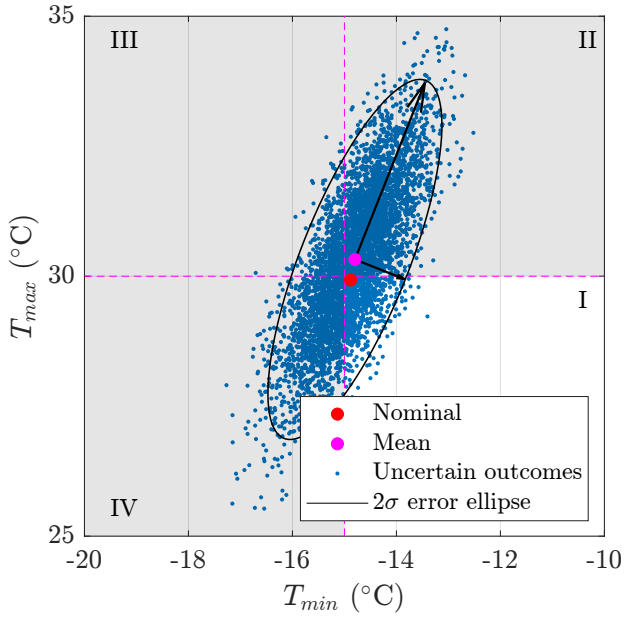

Figure 4-8: Nominal Optimal Solution under modeled uncertainty

The infeasible quadrants of the constraint space (gray) indicate the mode of temperature requirement failure of the uncertain outcomes. Quadrant IV in the lower left, which accounts for 27.8% of outcomes, indicates violation of the minimum temperature constraint, but not the maximum temperature constraint. Such outcomes can be described as cold-biased. Quadrant II in the upper right - the warm-biased outcomes indicating maximum temperature requirement violation only - account for 49.6% of outcomes.

There is some asymmetry in the distribution about the zero uncertainty outcome; the nominal (red point) and mean (magenta points) do not align and a significant plurality of outcomes occur in quadrant II. This is consistent with the sample variance about the blank wafer as shown in Figure 4-6. Variance of temperature outcomes is greatest near T_{max} (manifesting as variance along the y-axis), where albedo and Earth IR actively contribute to heat variance. By comparison, when near the end of eclipse, where T_{min} is usually attained, only uncertainty in Earth IR has an effect, resulting in lower variance (x-axis aligned variance in points). As such, the distribution is

skewed to the violations near the maximum temperature constraint. Comparatively, quadrants I and III contain very few outcomes. Quadrant III corresponds to bias to the extremes of temperature (most unfavorable) and quadrant I corresponds to bias towards the mean (most favorable).

The black arrows in Figure 4-8 represent the principal directions of variance from a principal components analysis (PCA). The principal components are defined by the eigendecomposition of the covariance of the temperature outcomes. The eigenvectors indicate the directions of the two principal components and the corresponding eigenvalues indicate the magnitudes of variance along the principal components directions.

From the distribution of outcomes, it is clear that violation of the temperature constraints due to the temperature uncertainties severely limits the practicality of the nominal optimal design. Although the power performance that it delivers is desirable, the low feasibility under uncertainty renders it unreliable in all but the nominal or seldom-realized best case outcomes.

The uncertain outcomes are shown for an ensemble of size $n = 10^4$ as blue points distributed around the nominal point in red. Note that the ensemble population size was selected to approximate the variance error from MC sampling to $< 2\%$ as shown in Figure 4-9.

4.3.2 The Robust Design is Not Nominal Optimal

The WaferSat problem can also be statically tailored to identify a solution that meets some statistical feasibility criteria. The active constraint space for this statically robust design is shown in Figure 4-10. Per the augmenting statistical constraints, the new estimated feasibility under uncertainty is 2σ, or feasible in 95.4% of the uncertain outcomes. However, in exchange for increased feasibility through static robustness, the power performance decreased from 1.15 W to 0.84 W. This is shown in the corresponding T_{min}, T_{max} constraint space in Figure 4-10. In this design, the

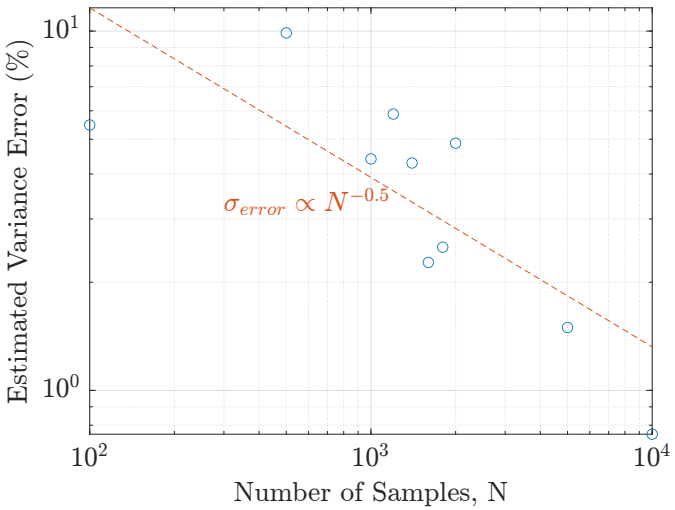

Figure 4-9: Standard rate of variance convergence error with Monte Carlo sample size. Population size $N = 10^4$ correlates to $< 2\%$ variance error.

entirety of the 2σ bounding ellipse is contained in the feasible space. The location of the nominal outcome is not offset from the temperature requirements indicating static margin. The directions of the principal components of variance (black arrows) indicate once again that there is greater variance in the maximum temperatures and as a result, more static margin is allocated.

Table 4.7: Summary of nominal and robust designs

Variable	**Symbol**	**Nominal**	**Static Robust**	**units**
zenith static emissivity	ε_z	0.10	0.11	-
zenith static absorptivity	α_z	0.09	0.09	-
zenith solar array coverage	f_{SA}	11.1	5.6	%
nadir static emissivity	ε_n	0.63	0.14	-
nadir static absorptivity	α_n	0.09	0.09	-
nadir solar array coverage	f_{SN}	69.7	59.3	%
mean zenith emissivity	$\overline{\varepsilon}_z$	0.18	0.15	-
mean nadir emissivity	$\overline{\varepsilon}_n$	0.18	0.13	-
mean zenith absorptivity	$\overline{\alpha}_z$	0.79	0.56	-
mean nadir absorptivity	$\overline{\alpha}_n$	0.67	0.58	-
Internal Power	P_{int}	1.15	0.84	W
Probability of Feasibility	$\mathbb{P}[feas]$	13.1	95.4	%

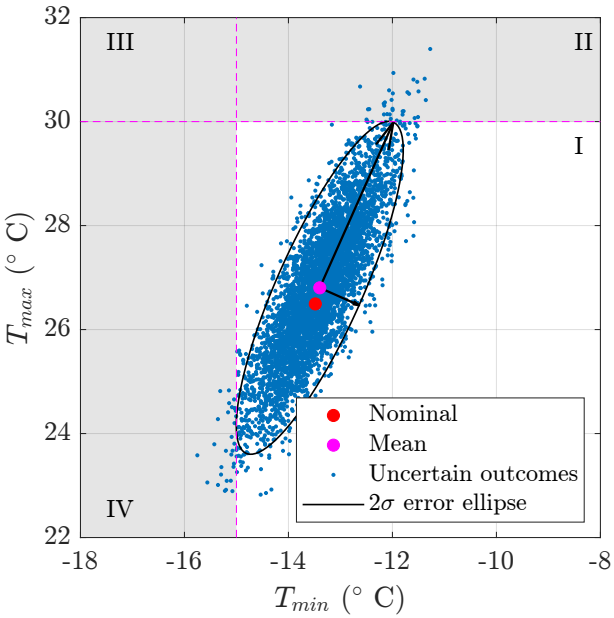

Figure 4-10: Nominal Optimal Solution under modeled uncertainty

The nominal optimal and static robust designs are summarized in Table 4.7. Notably, in the static robust design, the total solar array area is decreased by about 16% including both zenith and nadir surfaces. Additionally, the nadir static emissivity is significantly decreased. The result is apparent when observing the mean surface emissivities and absorptivities. The significant reduction in highly emissive and absorptive solar array area contributes to large decreases in the mean emissivities and absorptivites of the static robust design (summarized in lower half of Table 4.7). The net reduction in mean surface emissivity and absorptivity result in lower mean heat fluxes in and out of the system. This has two net effects: a reduction in the mean temperature oscillation (i.e., lower amplitude of mean temperature), and lower sensitivity to ephemeral local heat source variances due to uncertainty. This is measurable using principal components analysis.

The PCA properties of both designs are summarized in Table 4.8. Notably, the decreases in mean surface emissivities and absorptivities have contributed to a decrease in variance of outcomes as indicated by the reduction in both principal component eigenvalues. There is a reduction in size of both principal dimensions

of the 2σ error ellipse of the static robust design. The static robust design has increased feasibility through two methods: tailoring of requisite static margin at each performance-limiting constraint and a desensitization of the system temperature extremes to the heat uncertainties. The static margin manifests as a shift in the entire distribution to provide offsets of all points in the distribution away from the constraints. The desensitization results in a reduction in the point cloud of outcomes. The directions of the principal components are largely unchanged.

Table 4.8: Summary of PCA properties for Nominal and Static Robust Designs

Property	**Nominal**	**Static Robust**
PC 1 eigenvalue	2.23	2.02
PC 2 eigenvalue	0.17	0.11
PC 1 eigenvector	$[0.36, 0.93]^T$	$[0.41, 0.91]^T$
PC 1 explained var.	92.6%	94.7%

Whereas the nominal optimal design provides desirable performance, it is severely lacking in robustness. In stark contrast, the robust design significantly improves on robustness, but at the expense of the nominal performance. In a low SWaP system such as WaferSat, this exchange is costly, significantly reducing the utility of each unit. Responsive robust and adaptive methods may offer the ability to improve feasibility and maintain more performance through dynamic compensation to states of uncertainty. Three methods are introduced in the next section.

4.4 Responsive & Adaptive Mitigations

In this WaferSat design problem, optimization will consider combinations of three responsive and adaptive mitigations: phase change materials, thermal view factor control, and electrochromic area. Phase change materials, as introduced in the simplified WaferSat example, offer responsive robustness while thermal view factor control

and electrochromic area offer adaptability. In this section, a detailed description of the modeling, variable sets, and design considerations for these three mitigations is presented.

4.4.1 Phase Change Materials

Phase change materials offer two types of heat storage: sensible and latent. Sensible heat storage - heat storage associated with changes in temperature - is the most commonly thought of type of heat capacity. Latent heat is absorbed and emitted at constant temperature during a phase change. Introduction of phase change material mass with a tailored phase change temperature creates a period of constant temperature that is a function of net heat flows during the change. The effect is a dynamic lengthening of the thermal time constant (dynamic since the lengthening is a function of net heat flows during change).

Common high latent heat capacity PCMs include paraffins. As hydrocarbon chains, paraffins offer a large variety of materials with different phase change temperatures from which to choose. However, use of paraffins as PCMs has some implementation challenges, notably the containment during solid and liquid phases and conductivity of heat into and out of the PCM mass. Work on microencapsulation of PCMs in materials such as silicon nitride helps to solve both implementation challenges. An example slurry of microcapsules is shown in Figure 4-11 [99]. A common encapsulation ratio for Silicon Nitride by mass is 50% [100, 101]; this ratio will be assumed for this analysis.

The governing properties of the amount of heat absorbed and the length of temperature pause include PCM mass, phase change temperature (through material selection), encapsulation ratio, and rate of heat absorption/emission. Note that as a responsive tailoring mitigation, all of these variables are dynamic design variables that are set during the a priori phase; therefore, they augment the design in the outer loop

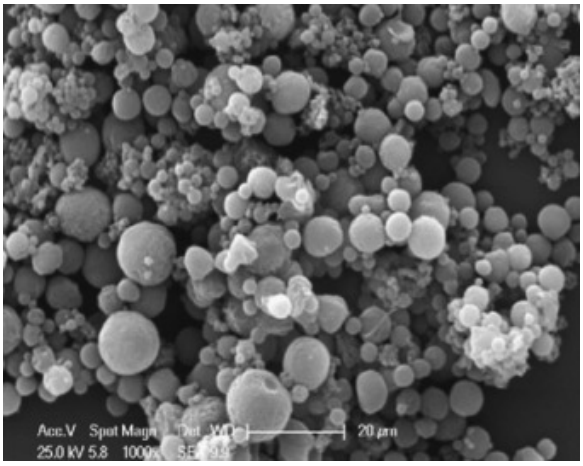

Figure 4-11: Silicon Nitride Paraffin Microcapsules [99]

optimization, while the modeled response is realized in the inner loop evaluations.

Table 4.9: PCM dynamic design variables

Parameter	**Notation**
PCM phase transition temperature	T_t
PCM latent heat of phase change	H_t°
PCM sensible specific heat capacity	c_p^{pcm}
PCM mass	m_{pcm}

Equation 4.16 shows the change in sensible heat over a change in temperature from T_0 to T_f. The sensible heat is a function of mass, m, and specific heat capacity, c_p (which may be a function of temperature).

$$\Delta Q_{sensible} = \int_{T_0}^{T_f} m c_p dT \tag{4.16}$$

Three possible changes in absorbed and emitted heat of a PCM are shown in Equation 4.17. Line one shows the energy absorbed by a PCM for a temperature change from T_0 to T_f with a complete phase change at T_c, therefore $T_0 < T_c < T_f$. H_c° indicates the mass-specific absorbed enthalpy of phase change from phase 1 to 2. Line two gives the absorbed energy of a partial phase change from temperature T_0 to T_c where the percentage of PCM mass that is in phase 2 is χ_c. $\chi_c = 0$ indicates that all mass is in phase 1 and $\chi_c = 1$ indicates that all PCM mass is in phase 2. Line

three of Equation 4.17 indicates the liberated heat during a partial phase change from phase 2 to 1 during a decrease in temperature from T_f to T_c. χ_c again indicates the PCM mass percentage in phase 2. In all three lines, the integral lines (associated with changes in temperature) correspond to sensible heat and the linear terms represent the storage of release of latent heat (at constant temperature T_c).

$$\begin{aligned}
\Delta Q_{complete12} &= \int_{T_0}^{T_c} mc_p dT + m_{pcm} H_c^\circ + \int_{T_c}^{T_f} mc_p dT \\
\Delta Q_{partial12} &= \int_{T_0}^{T_c} mc_p dT + m\chi_c H_c^\circ \\
\Delta Q_{partial21} &= \int_{T_f}^{T_c} mc_p dT - m_{pcm}(1-\chi_c) H_c^\circ
\end{aligned} \tag{4.17}$$

The duration of constant temperature, T_c, during changes between phases 1 and 2, is given in Equation 4.18. The time is heavily dependent on the heat flux term, Q_{net}^c, which is a summation of all system heat fluxes during the phase change. This term is a function of position, temperature, and surface design variables. For complete change from phase 1 to 2, in line 1, $\chi_c = 1$. For a complete change from phase 2 to 1 in line 2, $\chi_c = 0$.

$$\begin{aligned}
t_{12} &= \frac{m_{pcm} H_c^\circ \chi_c}{Q_{net}^c(T_c, \theta)} \\
t_{21} &= \frac{m_{pcm} H_c^\circ (1-\chi_c)}{Q_{net}^c(T_c, \theta)}
\end{aligned} \tag{4.18}$$

When considering use of PCM mass to increase thermal time constants, it is important to consider the implementation impacts on the system. In order to maintain a constant total mass constraint on the system, in the WaferSat problem, it is assumed that any additional PCM mass must displace the equivalent mass of silicon. This displacement of mass presents a tradeoff: the more the system relies on PCM mass

to maintain feasibility, the more the usable Si substrate must be reduced in favor of the functionally inert, but responsive robustness-producing PCM.

4.4.2 Thermal View Factor Control

As shown in §4.1.3, radiative heat flux terms have a linear dependency on view factor between surfaces. Adjustment of spacecraft attitude has an impact on thermal view factors - particularly view factors to the surface of the Earth - and can thus be used to regulate heat flows. This is an actively tuned compensation and would therefore be classified as thermal adaptability.

Design of adaptive mitigations involves optimization of dynamic variables in the a priori design phase as well as the tuned response in the a posteriori phase. In a full design optimization of the system, the adaptive tailoring step would involve the design of the attitude control system in order to allow the requisite control of view factors. For simplicity, in this thesis, it is assumed that an electrospray system thrusts out of plane at the edges of the wafer to enable control of spacecraft roll about the velocity vector. This does, however, set constraints on the maximum roll rate of the system. Therefore these assumed dynamic variables still govern the tuneable response. Therefore, in this example, thermal view factor control presents as a tuning only mitigation with constraints from assumed, constant dynamic variables (i.e., the design of the ACS).

Nominally, WaferSat is assumed to be in a low drag configuration, edge on to the velocity direction with one surface-normal always nadir-facing. In order to maintain the low drag configuration, it is assumed that any changes in attitude for thermal view factor regulation will occur about the Local Vertical Local Horizontal (LVLH) roll axis only (or roll about the alongtrack velocity direction).

The net heat flows as a function of roll angle from Figure 4-12a only consider the heat flow variation at a single point in the orbit. An expansion of the net heat

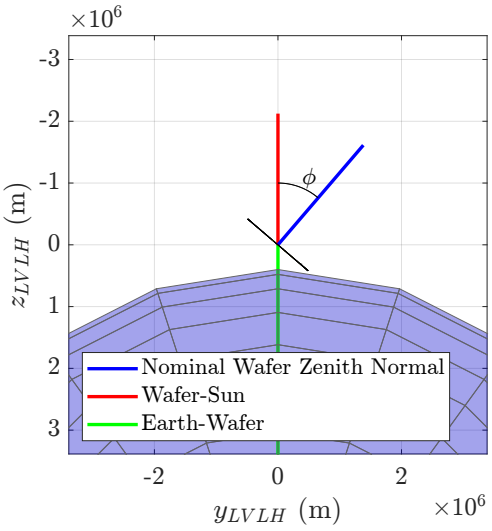

(a) View of WaferSat in LVLH frame, rolled through angle ϕ

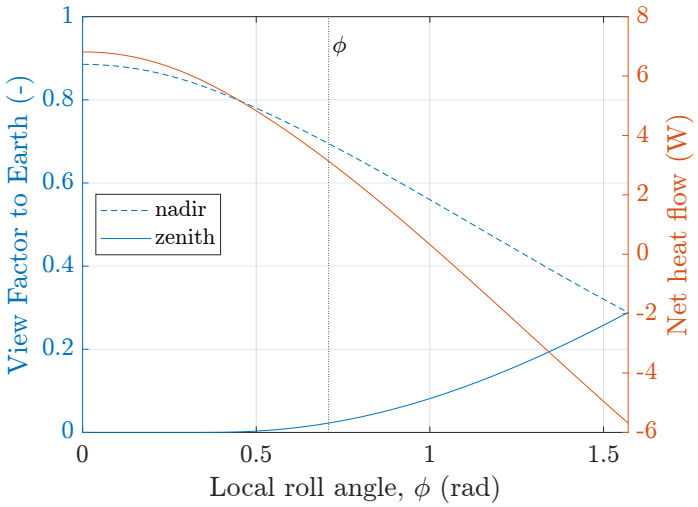

(b) View factors of both surfaces to Earth (blue, left axis) and net heat flow (orange, right axis) at $\theta = 0$; LVLH roll angle from (a) shown with dashed line

Figure 4-12: WaferSat LVLH roll, thermal view factors, and net heat flows at $\theta = 0$

flows to show the heat variance as a function of position within the orbit is shown in Figure 4-13. In addition to the net heat flows, and LVLH roll angle, an additional axis for true anomaly (or position in the orbit relative to the point in the orbit that is closest to the sun) is shown. A surface plot shows the variation in net heat flows in (positive) or out (negative) of the system as a function of roll angle and position. The gray plane demarcates the boundary between positive and negative heat flows. Note that the orange edge on the right of the plot matches the orange net heat flow line from Figure 4-12b. The magenta edge at the back left of the figure represents the nominal, zero-roll net heat profile. The discontinuous negative section in the middle of the surface is the eclipse portion of the orbit. Notably, at every sunlit position in the orbit, there exists a roll angle that can produce a net negative heat flow, or a cooling effect.

The net heat flows shown in Figure 4-13 are shown as an example for the nominal case. In reality this would need to be recomputed as needed at each location in response to uncertainty rather than as an entire surface. Furthermore, the shape

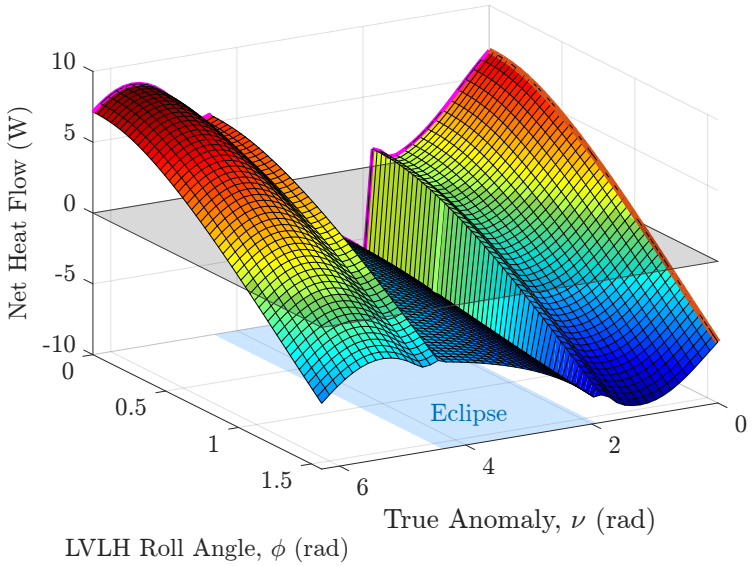

Figure 4-13: Net heat flows as function of LVLH roll angle and True Anomaly, $\beta = 0$

of the surface will vary significantly with changes in the orbit. Notably, as β angle changes, the LVLH roll angle of maximum heating will vary. In this example, a roll angle of 0 always corresponds to the greatest net heat flows (the magenta edge in the back left of the figure).

4.4.3 Electrochromics

Another thermal control variable for thermal radiation is the emissivity. In general, surfaces have a constant profile of emissivity as a function of wavelength. However electrochromics offer an option to selectively assign emissivity within a bounded range. This commanded change to emissivity, and thus rate of thermal radiation, can allow for tuning of net radiative magnitude.

A company, Eclipse Energy Systems has developed, tested, and flown an electrochromic surface, EclipseVED [73]. Measured electrochromic emissivity data as a function of wavelength is shown in Figure 4-14 [102]. The high emissivity state, red, and the low emissivity state, blue, bound the range of tunable emissivities of the

surface.

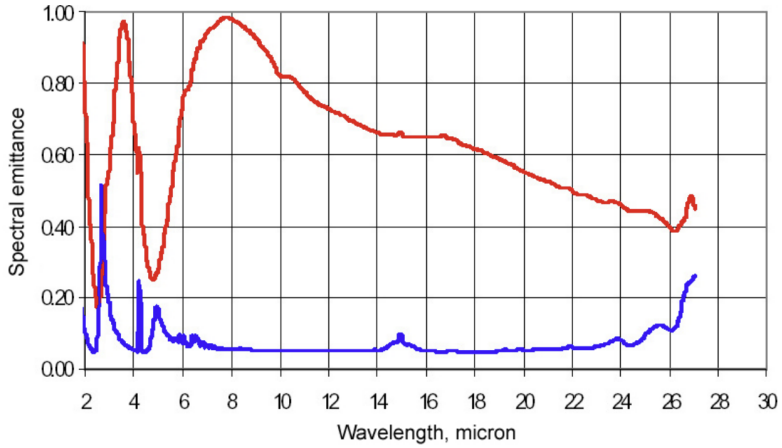

Figure 4-14: Measurements of EclipseVED electrochromic emissivity as function of wavelength in: low emissive (blue) and high emissive (red) states [102]

Although the electrochromic emissivity data indicates a continuous function as a function of wavelength, modeling of the electrochromics in this work assumes a single electrochromic value for the bin of IR wavelengths. The peak black body radiating wavelength is given by Wien's Displacement Law, shown in Equation 4.19. The peak wavelength, λ_{peak} is a function of the proportionality constant, $b = 2898\,\mu\text{m}$, and the black body temperature, T.

$$\lambda_{peak} = \frac{b}{T} \tag{4.19}$$

Wien's displacement law identifies the peak radiating wavelength of Planck's law, shown in Equation 4.20. The spectral irradiance intensity, B, is expressed as a function of wavelength, λ, and black body temperature, T.

$$B(\lambda, T) = \frac{2hc^2}{\lambda^5} \frac{1}{e^{hc/(\lambda k_B T)} - 1} \tag{4.20}$$

The Planck's Law curves for spectral irradiance vs. wavelength are shown in Fig-

ure 4-15 for the two temperature consraints. The peaks of irradiance occur according to Wien's Displacement Law. The peak wavelengths are 9.5 and 11.2 µm for the maximum and minimum operating temperature constraints respectively (shown with black dashed lines). Therefore, for WaferSat operation within the feasible and operable temperature range, the peak emissive wavelengths should be approximately bounded by this range. The range from 9.5 to 11.2 µm is approximately aligned with one of the maximum ranges of the electrochromic emissivity from Figure 4-14. For simplicity, the range of emissivities used for electrochromic modeling is from 0.2 to 0.8 applied to the IR wavelength bin.

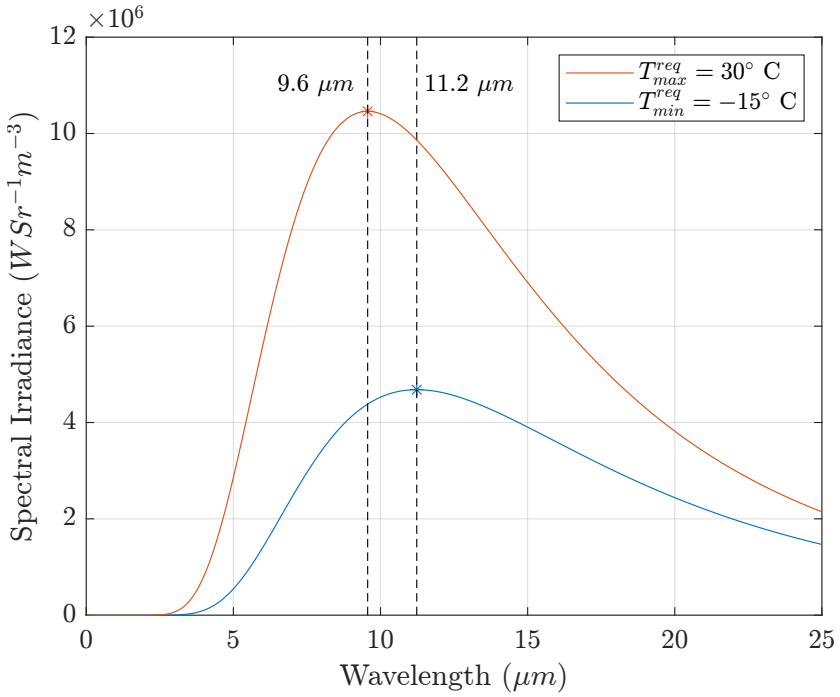

Figure 4-15: Planck's curve for the bounding temperature requirements with Wien's Law peak irradiance wavelengths.

While three thermal mitigation options are used in this example, there are many other potential methods for mitigation of the thermal constraints under uncertain conditions. Optimization with these three mitigations will allow for an exploration of unique combinations thereof. The three thermal mitigations in this WaferSat problem will be used to maintain temperature constraint satisfaction under uncertainty whilst maintaining high power performance.

There are more available options for survival, noting the wider temperature requirements for non-operational survival as indicated in Table 4.3, or switching to non-operational power states that reserve power dissipation for heating in eclipse and dormancy in the sun. If there are ever conditions in which the system goes into safe mode or an otherwise non-operational state, the ability to actively control adaptive mitigations may be lost. By comparison, a responsive mitigation which acts passively (like PCMs) could continue operation even if the spacecraft is in safe mode. To this end, a system could be designed to be able to meet the wider survival temperature constraints with passive responsive mitigations only and meet the operational temperature constraints with active adaptive mitigations.

4.5 Comparing Isoperforming and Isofeasible Solutions

Optimization for performance and feasibility results in the identification of multiple solutions that are both isoperforming (equal in performance) and isofeasible (equal in feasibility). All three designs have been optimized to produce a 2-σ guarantee of feasibility as well as the same power performance level as the nominal optimal design of 1.15 W. In this section, three designs utilizing different levels of static robustness, responsive robustness, and adaptability are compared. The non-uniqueness of the three designs reveals that the same performance and feasibility are both achievable with different approaches to mitigation of the effects of uncertainty. Consideration of the 'costs' of implementation might cause a preference for a particular design, based on the mission at hand. The mission may impose constraints on the implementation of the responsive or adaptive mitigations compelling a specific relative emphasis. The optimization process involves the design of static variables, dynamic variables for responsiveness, dynamic variables for adaptability, and adaptive variables. In Figure 4-16 an example of the surface design of the zenith and nadir sides of the

wafer is shown.

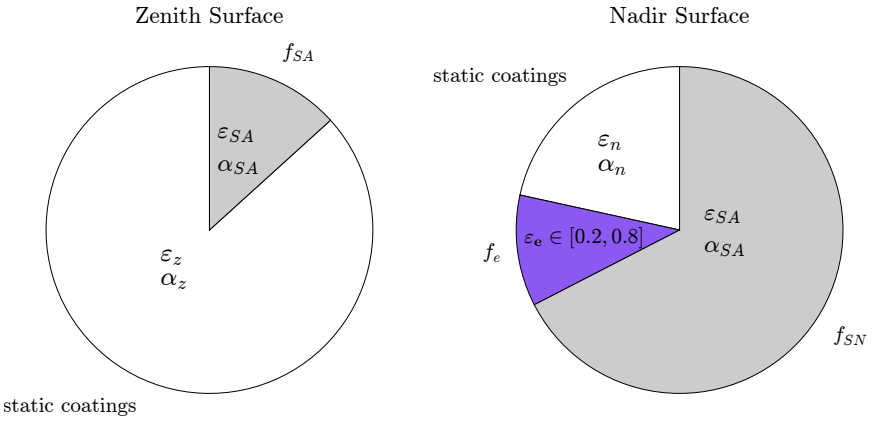

Figure 4-16: WaferSat surface design with allocation of nadir area to electrochromics (purple).

While all three identified designs utilize each of the three mitigation methods to some degree, each design has a distinct emphasis on the usage of one mitigation in particular. The key static and dynamic variables are summarized in Table 4.10. Design 1, *D1* emphasizes PCMs - it has the largest quantity of PCM, and thus the majority of its mitigation of the effects of uncertainty come from the corresponding responsive robustness afforded. Design 2, D2, is weighted towards electrochromics and adaptability. Finally, Design 3, *D3* relies most heavily on thermal view factor management, a different form of adaptability. Furthermore, each design utilizes a different set of static variables and therefore each design also utilizes a different level of static margin.

The three designs utilize distinct combinations of robustness and adaptability, but they also share some commonalities. In all three designs, most of the solar array area is populated on the nadir surface, with limited area on the zenith surface. As a result, most of the solar power generation occurs through albedo-reflected sunlight or direct solar illumination of the nadir surface. Interestingly, this source of solar illumination is also subject to uncertainty. The zenith surface, which constantly radiates to free-space with no thermal view factor to the Earth is a large sink of heat out of the system. Survival and operation during eclipse, without incident solar input, and with limited

Table 4.10: Summary of key static and dynamic variables of three isoperforming and isofeasible designs.

Variable	**Symbol**	**D1**	**D2**	**D3**	**units**
zenith static emissivity	ε_z	0.16	0.14	0.18	-
zenith static absorptivity	α_z	0.09	0.09	0.09	-
zenith solar array coverage	f_{SA}	13.3	13.1	16.2	%
nadir static emissivity	ε_n	0.14	0.62	0.44	-
nadir static absorptivity	α_n	0.09	0.09	0.09	-
nadir solar array coverage	f_{SN}	67.4	67.8	64.6	%
PCM mass	m_{PCM}	21.1	10.8	10.1	g
Temperature of fusion	T_f	290	261	258	K
electrochromic area coverage	f_e	11.1	22.9	10.8	%
electrochromic value at nominal	ε_e^c	0.70	0.63	0.68	-
max LVLH roll angle	ϕ_{max}	2.8	5.6	28.6	°

internal power, drives the need for low radiation to free space. As a result, the zenith static emissivity coatings and zenith solar array area (with high emissivity coverglass) are optimized to low values. The design of power generating area on the nadir-facing surface, while unusual, has some precedent is spacecraft design. Early Russian spacecraft utilized bifacial solar cells to augment power generation through albedo reflected solar irradiance in low Earth orbiters [103]. More recently, analysis of bifacial solar cells has been shown to potentially increase power output of LEO satellites with limited increases in mass [104, 105]. Since 2000, the International Space Station has utilized bifacial solar cells, generating power through albedo and increasing average power during scenarios when the solar array gimbals must be locked [106].

4.5.1 Design 1: PCM-Dominant

Design 1 - the PCM-dominant design - derives the lion's share of its ability to maintain performance and feasibility from responsive robustness. Phase change material offers mass with a high net internal heat storage capacity through latent heat absorption during the phase transition.

The optimization was guided towards this design by placing additional constraints in the implementation of the three mitigations. The maximum allowable electrochromic area, f_e is 12%, the maximum allowable LVLH roll angle, ϕ_{max} is 0.1 rad, and the maximum PCM mass is 30 g. In this scenario, the allowable electrochromic area and LVLH roll angles are more restricted whereas the total PCM mass is relatively unrestricted and allowed to displace up to 10% of the total WaferSat mass. This might correspond to an application where there is a need to populate some of the surfaces with other components such as instruments (restricting allowable area for electrochromics) and relatively precise control over pointing is needed (i.e., a desire not to let thermal view factor control dominate spacecraft attitude).

The realizations under uncertainty - for an ensemble of size $p = 10^4$ - is shown in Figure 4-17. The two axes show the quasi-steady state extreme temperatures along with the respective temperature requirements in magenta dashed lines. The point cloud of outcomes is characterized using two methods. The first is a 2-element Gaussian Mixture Model (GMM) with 2σ bounding error ellipse. The second method is Non-Linear Principal Component Analysis. The first principal component of variance is shown as a green curve through the point cloud. This line indicates the primary axis of variance. The red point indicates the nominal, zero uncertainty scenario and the magenta point indicates the mean maximum and minimum steady state temperatures over the uncertain set of outcomes.

The optimal values of the dynamic variables reveals the mechanism of feasibility maintenance. The temperature of fusion, T_f of 290 K is in the upper third of the feasible temperature range. This bias towards the maximum temperature constraint increases the responsive margin allocated to the T_{max} constraint. This is observable in the locations of the nominal and mean points; they are both further from the T_{max} constraint, an indicator of margin focused near this constraint. The close proximity of the nominal point to the T_{min} constraint indicates that limited responsive robustness effect for this constraint.

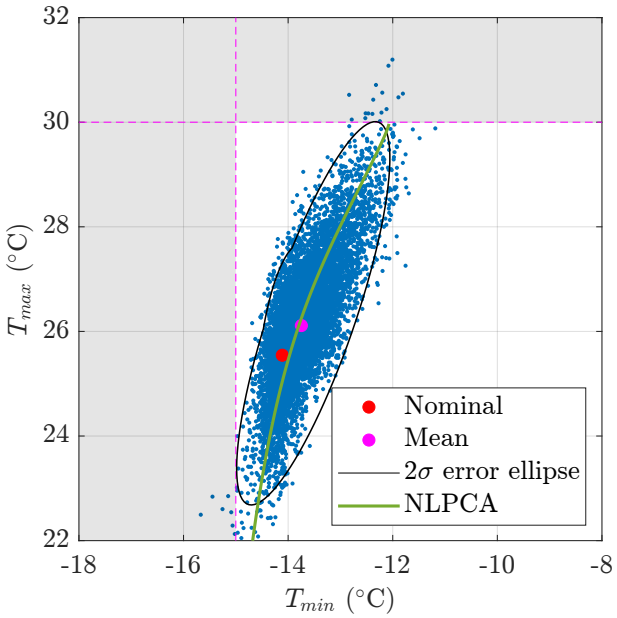

Figure 4-17: Design 1 distribution of outcomes in T_{max} and T_{max} constraint space with GMM 2σ error ellipse and NLPCA first principal axis of variance

The optimal value of the nominal center value of the electrochromics, ε_e^c also reveals the focus of adaptability. The high value of ε_e^c of 0.7 within the range 0.2 to 0.8, means that there is much more authority of electrochromics to reduce thermal radiation from the nominal state. Therefore, the activity of the electrochromics is more effective at mitigating uncertain effects near T_{min}. This is apparent in Figure 4-17, where the variance is lower in the T_{min} (x-axis). Additionally, the direction of the NLPCA first principal component curve is more aligned with the vertical T_{min} temperature requirement. Therefore, the principal component of variance (along the curve) is more aligned with the T_{max} axis rather than the T_{min} axis which is favorable near the T_{min} temperature requirement.

In this design, responsive robustness is focused near the T_{max} constraint, and adaptability is focused near the T_{min} constraint. This helps to reveal the distinct mechanisms of reduction in sensitivity of constraint satisfaction. Responsive robustness acts by providing responsive margin, thereby shifting the nominal, mean, and distribution away from the constraint. In contrast, adaptability that is focused near

a constraint has a tendency to reduce the magnitude of variance in the direction of the constraint.

4.5.2 Design 2: Electrochromics-Dominant

Design 2 - the electrochromics-dominant design - relies the most on adaptability. In this design the mitigation constraints are adjusted to allow for a greater area of electrochromics: up to 25%. In contrast to Design 1, the PCM mass is limited to 12 g and the maximum LVLH roll angle is 0.10 rad.

As the design that relies most heavily on the adaptability of emissivity regulation, this design has the lowest overall variance in outcomes as shown in Figure 4-18. The ensemble of uncertain outcomes is again characterized with a GMM model with bounding 2σ error ellipse. However, in this design, the distribution of outcomes is not well defined for NLPCA. Optimization of the PCM temperature of fusion, T_f at 258.6 K or -14.4° C results in the PCM response occurring near the minimum temperature constraint. There are some uncertain SoTW where incident Earth IR is higher than nominal during eclipse which result in less cooling during eclipse. One of these scenarios is shown in Figure 4-19 which shows the quasi-steady state temperature trace vs. time on top and the PCM liquid ratio, χ_l in the bottom plot. In this scenario, the PCM only partially freezes, and $T_{min} = T_f$; this is true for all partial freeze scenarios (note that the nominal scenario is a partial freeze scenario). The effect is visible near the vertical T_{min} line at -14.4° C in Figure 4-18 where there is a faint cluster of points all with $T_{min} = T_f$. This high density of T_{min} values at the same value prevents convergence of the NLPCA axis of variance estimate.

Despite the proximity of the PCM temperature of fusion to the minimum temperature requirement, the nominal and mean points in the constraint space are still closer to the minimum temperature constraint. In this design, there is still responsive margin focused near the minimum temperature constraint, but it is contained in the

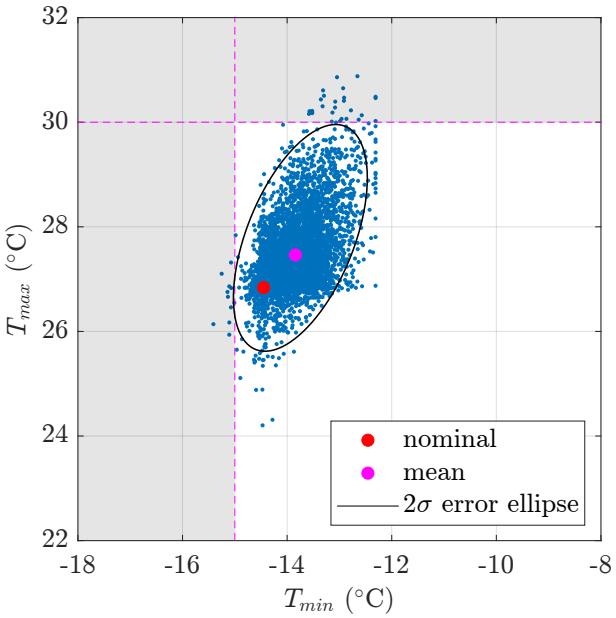

Figure 4-18: Design 2 distribution of outcomes in temperature constraint space.

latent heat storage of the PCM.

The nominal value of the electrochromics, ε_e^c, of 0.63 still provides significantly more adaptive authority to decrease net thermal radiation than increasing. This contributes to the asymmetry of the distribution; there is more variance in T_{max} than T_{min} and there is greater variance above the nominal T_{max} and T_{min}. Variance of T_{min} is strongly reduced by the partial PCM freezing as well as electrochromic range.

As in the simplified example from § 3.6.2, there are three outcomes of electrochromic adaptability at a given point in time and position in the orbit. Exact compensation, where the electrochromic value is able to completely counter the perturbing effect of local heat flux uncertainty results in reproduction of the nominal temperature conditions at that point in the orbit. In this case, the commanded value of electrochromics is interior to the tuneable range ($\varepsilon_e^{min} < \varepsilon_e < \varepsilon_e^{max}$). Note that in the scenario where there is exact compensation of the quasi-steady maximum and minimum temperatures of the orbit, the red nominal point of Figure 4-18 is reproduced under uncertainty (for saturation reasons, this is not a common occurrence).

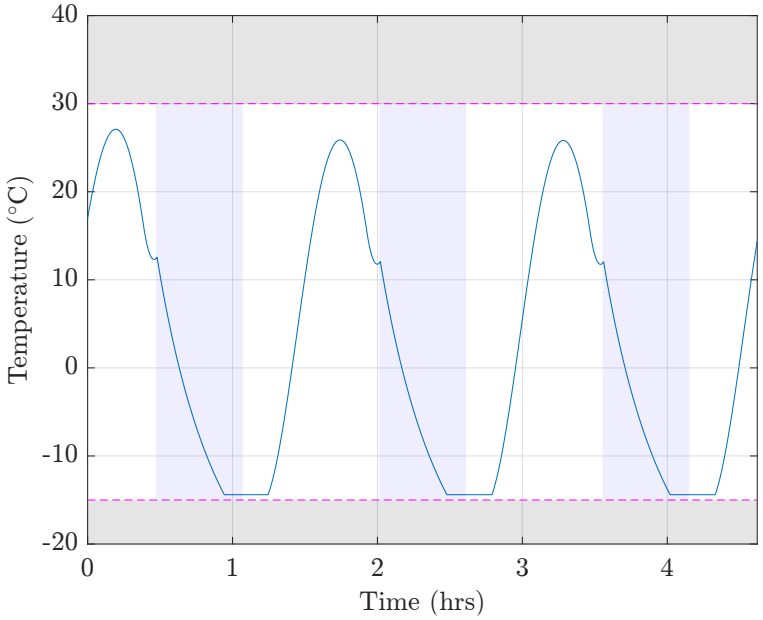

(a) Temperature oscillation over three orbits; $T_{min} = T_f$

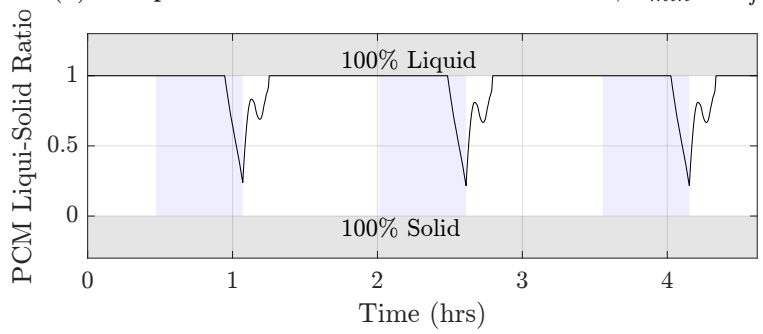

(b) PCM Liquid-Solid mass ratio over time

Figure 4-19: Design 2 PCM partial freeze scenario.

There are also two saturation cases, wherein the commanded value of electrochromics is limited by the tuneable range. Saturation high occurs where the electrochromics value is at the maximum of the range, $\varepsilon_e = \varepsilon_e^{max}$. In this scenario, exact compensation is out of reach, and the realized temperature will be greater than nominal. Conversely, saturation low occurs where $\varepsilon_e = \varepsilon_e^{min}$ and the realized temperature is lower than nominal. These cases are viewable in Figure 4-20 which depicts a single, selected uncertain scenario out of the ensemble. Figure 4-20a shows three cases of the quasi-steady state temperatures over a single orbit. The red trace shows the nominal, zero uncertainty temperatures.

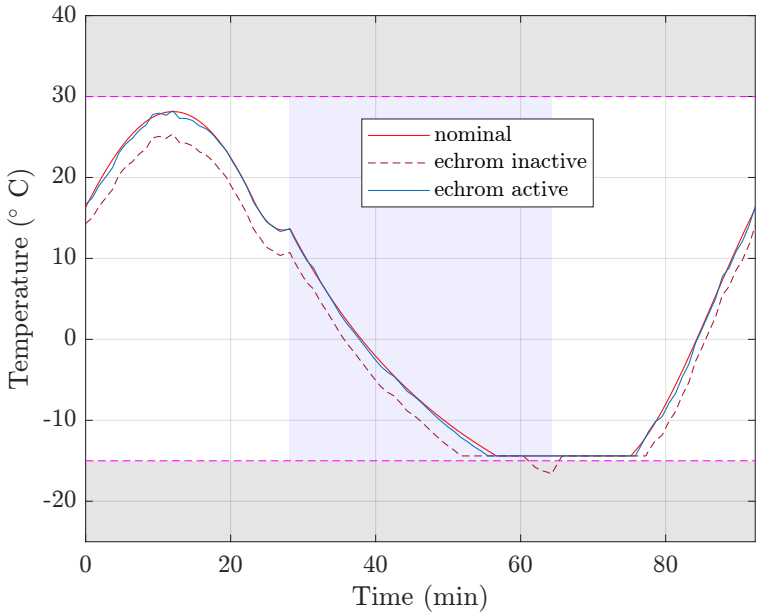

(a) Temperatures vs. time over one orbit. Shown: nominal, inactive electrochromics, optimally tuned active electrochromics

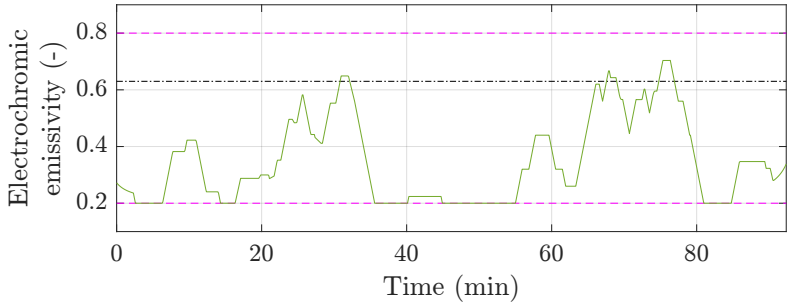

(b) Optimally tuned electrochromics in active case

Figure 4-20: Temperature and electrochromics response for the adaptive mitigation of a selected uncertain outcome.

The blue trace shows the tuned, electrochromics-mitigated temperatures. The dashed trace shows the temperatures under uncertainty if the electrochromic area is inactive and at the electrochromic value at nominal. The tuned electrochromic values are shown in Figure 4-20b. As shown by the dashed electrochromics inactive temperature trace, this uncertain scenario is mostly uncertain in the cold direction. As a result, there are several cases of saturation low, shown where the green line of Figure 4-20b is equal to 0.2 and the blue mitigated temperatures are below the red nominal. The

exact compensation cases occur where the commanded electrochromics values are not at the limits. At these times, the blue uncertain cases are close to the nominal temperatures. Note that during the tuning process, it is assumed that local albedo and T_E are not directly known. Instead, all commanded electrochromic values are calculated in reaction to detectable temperature changes. Therefore, there is some phase lag and some error even in the exact compensation cases.

4.5.3 Design 3: Thermal View Factor-Dominant

Design 3 relies most heavily on thermal mitigation through adaptive view factor control (VFC). As WaferSat is exposed to perturbing heat flows, adjustments to the LVLH roll angle are made to gain favorable thermal view factors either to regulate the system net heat flows up or down. This design allows for the greatest maximum LVLH roll angle of 28.6°, while constraining PCM mass to 12 g and electrochromic area to 12%.

The constaint space and distribution of quasi-steady state temperature distribution is shown in Figure 4-21 under the local albedo and T_E uncertainty set. As shown in § 4.4.2, for a β angle of zero, the nominal nadir-facing orientation corresponds to the greatest net heat absorption due to the greatest solar exposure. As a result, at all points in the orbit, from this β angle, LVLH roll has a cooling effect (turning away from the sun, reducing view factor to the Earth). In this design, the nominal point, shown as a red point, is closest of all designs to the maximum temperature requirement since there is more ability to regulate heat flows down with LVLH roll.

To display the tuning response in one uncertain scenario, a single uncertain SoTW is shown in Figure 4-22. In Figure 4-22a are the quasi-steady state temperatures for three cases: nominal (no uncertainty) in red (same as the red point from Figure 4-21), inactive VFC in the single uncertain SoTW - i.e., WaferSat maintained in nadir-pointing orientation for all time - in a dashed line, and an active VFC case

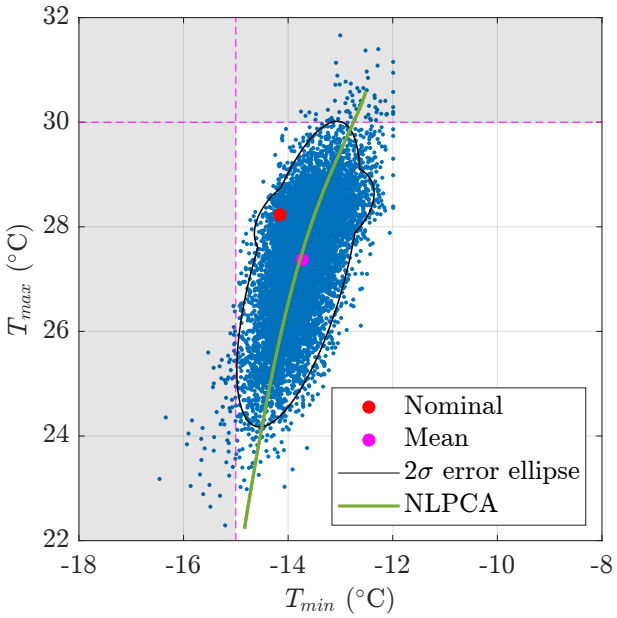

Figure 4-21: Design 3 distribution of outcomes in temperature constraint space.

in blue. The corresponding LVLH roll angles vs. time for the VFC active case are shown in Figure 4-22b. Similar to the operation of the electrochromics, there are several states of operation at each position in the orbit. The saturation cases indicate times when the roll angle is at its limits: $[0°, 28.6°]$ (due to the symmetry for $\beta = 0$, only positive roll angles are considered). Note that during eclipse, the spacecraft always resumes the nadir-facing (0 roll angle) orientation, in order to retain heat in the absence of sunlight. At several points in the orbit, the LVLH roll angle assumes a value interior to the range limits, corresponding to an exact compensation case. However, like the electrochromics compensation cases, since the roll angle is responding to temperature changes, the exact compensation never results in exactly nominal temperatures. Furthermore, due to constraints in roll rate due to the assumed ACS, limits on the rate of roll angle can also prevent the optimal roll angle at a given position from being attained. The WaferSat was assumed to roll at a maximum rate of $0.3\,\mathrm{rad\,min^{-1}}$. This was an assumed constant only; more detailed exploration of the impacts of maximum roll rate would aid in further evaluation.

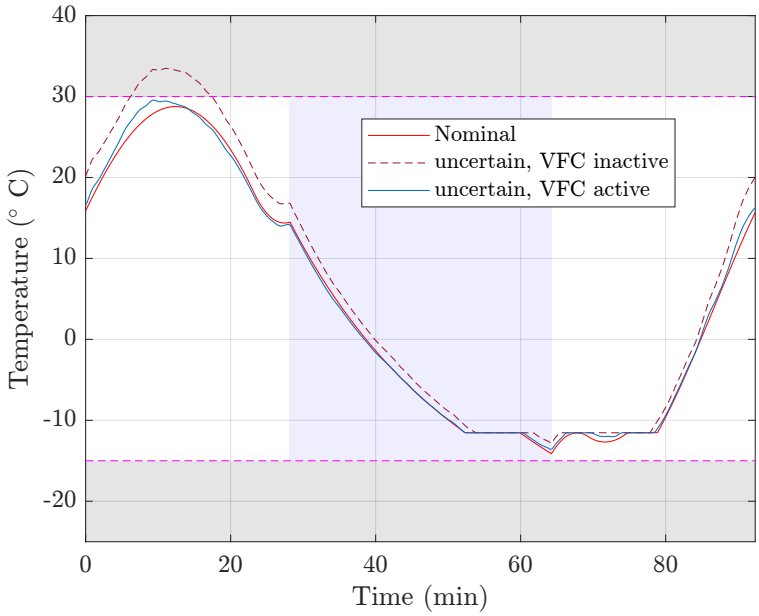

(a) Temperatures vs. time over one orbit. Shown: nominal, inactive VFC, optimally tuned active VFC

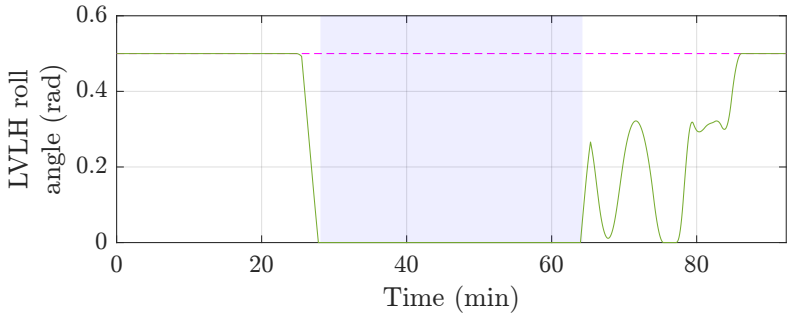

(b) LVLH roll angle as a function of time in one orbit to regulate temperatures

Figure 4-22: Temperature and LVLH roll response for the adaptive mitigation of a selected uncertain outcome.

As with each of the mitigation methods presented, control of thermal view factors carries with it an associated cost of implementation. By allowing thermal requirements satisfaction to drive spacecraft roll angle, there is a reduction in the ability to point WaferSat at-will, for example, for payload purposes. While this might work well for applications where the payload involves an omni-directional sensor, or where pointing is otherwise unimportant, in the cases where precise pointing is mission critical, pointing for thermal regulation and payload may be at odds. Another

strategy might be to restrict thermal view factor control to times when the payload is not operating, but this involves new mission timeline constraints.

4.5.4 Summarizing Designs

Optimization with different sets of constraints in the implementation of the responsive and adaptive mitigations enabled the identification of three unique designs that achieve the same level of expected performance and feasibility under the modeled uncertainty ensemble. These unique designs each have a distinct emphasis on one of the three mitigations introduced. These distinct designs can be said to achieve the same function with unique form. The defining mitigation variables for the three design families are summarized in Figure 4-23. The dynamic and adaptive variable sectors of the radar plot are labeled with the corresponding mitigation. Greater utilization of a particular area is indicated by greater radius in that area. Design 1 is the most reliant on the responsive robustness of PCM. Design 2 is most adaptable due to electrochromics, and Design 3 is most adaptive with thermal view factor control.

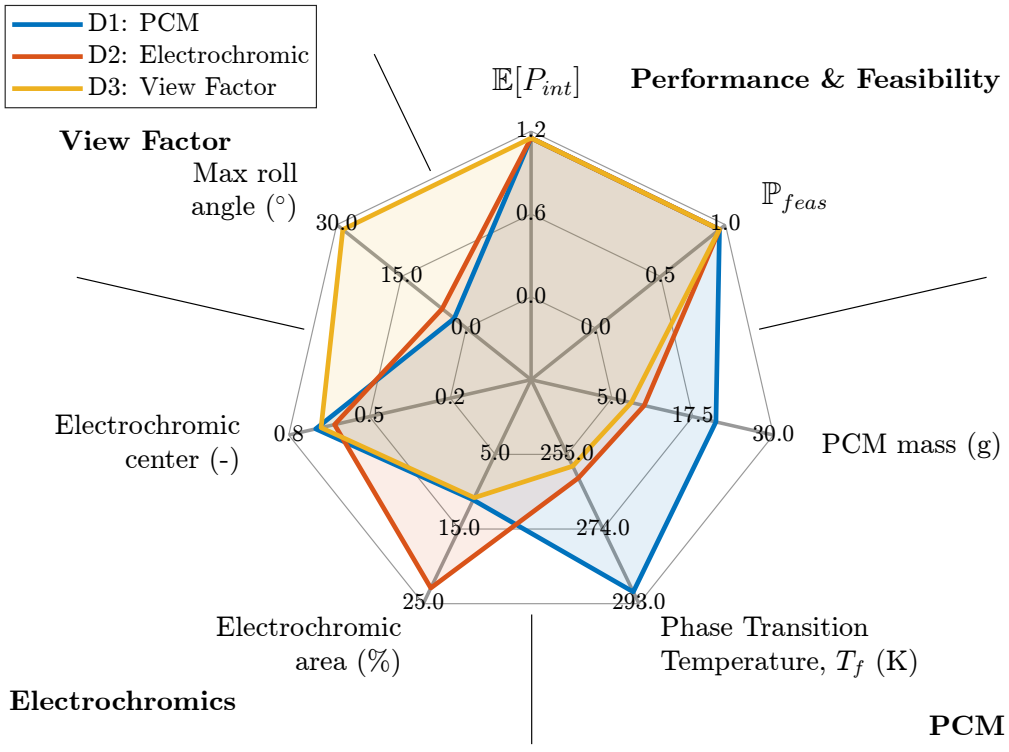

Figure 4-23: A comparison of the relative level of utilization of the responsive and adaptive mitigations for three isoperforming and isofeasible designs

The operation under uncertainty is summarized in Figure 4-24, which shows the temperature constraint spaces (repeated from §§ 4.5.1 to 4.5.3). The sizes, shapes, and locations of the uncertain outcomes is indicative of the dominant mechanism of uncertainty mitigation. Design 1 is responsively robust, therefore there is still high variance in the outcomes. However, the location of the nominal and mean outcomes reveals the responsive margin added. Design 2 is very thermally adaptive with electrochromic areas. The adaptive emissivity is able to regulate heat flows to reduce variance in temperature. This has the smallest variance of all cases. Design 3 gains adaptability through reorientation of the thermal view factors. All three design outcome distributions exhibit some re-shaping of the distribution to better fit within the design space. In particular designs 1 and 3 curve the principal axis of variance near the minimum temperature constraint so that the tails of the distribution still partially lie in the feasible space.

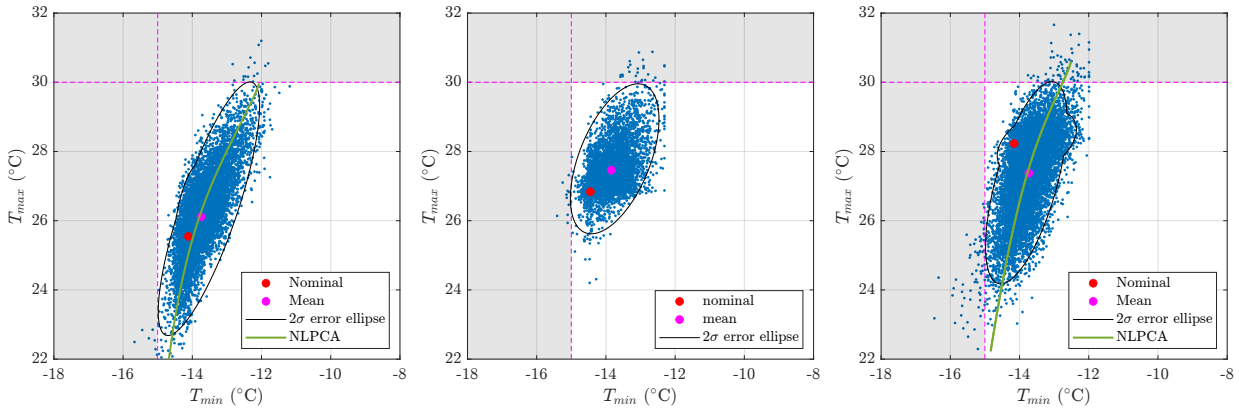

(a) Design 1: PCM-dominant

(b) Design 2: electrochromic-dominant

(c) Design 3: View factor-dominant

Figure 4-24: A comparison of temperature constraint spaces for designs 1, 2, 3

Though three individual designs were identified, they exist out of an infinite set of designs that are both isoperforming and isofeasible. In other words, there exists an infinite number of combinations (continuously variable relative usage) of the three mitigations. Constraints related to the application can be used to evaluate where in this infinite set the design should lie.

The performance and feasibility estimates thus far are predicated on the assumption that the uncertainty model is accurate. In practice, there may be some uncertainty in the uncertainty model itself. In the next section impacts of parametric errors in the uncertainty model are assessed.

4.6 Modeled Uncertainty Error

The prior optimizations design for a threshold level of feasibility under a specified uncertainty model. Therefore the performance and feasibility guarantees apply for the modeled uncertainty distribution. In this example, the feasibility guarantees are explored when there is parametric uncertainty in the uncertainty model.

The variances of the uncertain local Earth black body temperature and Earth albedo are based on measured data from NOAA and CERES missions. However, in general, there is always some uncertainty in any model. As an example, in this scenario, the feasibility of designs is explored when there is a change in the modeled uncertainty variance. For several designs, the estimated feasibility is examined under the original modeled variance, for a 2x variance, and for a 3x variance. In particular, designs will be evaluated based on their resilience to parametric uncertainty in the model.

Recall the static robust design from § 4.3.2. Nominal performance was sacrificed in order to create margins against the active thermal constraints. However, the feasibility guarantee was specifically tailored to *just* meet the 2-σ feasibility guarantee under the modeled uncertainty distributions. Therefore, as the variance in the uncertain parameters is increased, it is expected that the incidence of feasible outcomes will suffer. This is shown in Figure 4-25 where three different distributions of extreme temperatures are shown corresponding to the 1x variance (purple), 2x variance (orange), and 3x variance (blue). Since this design specifically tailored only the requisite static margin against the temperature requirements, there is no extra margin for

the increased variance cases. Once the tailored margin has been overwhelmed, there is no other recourse to maintain feasibility. At 3x the original model variance, the incidence of feasibility is 79%, with many temperature requirement violations of both the maximum and minimum temperatures.

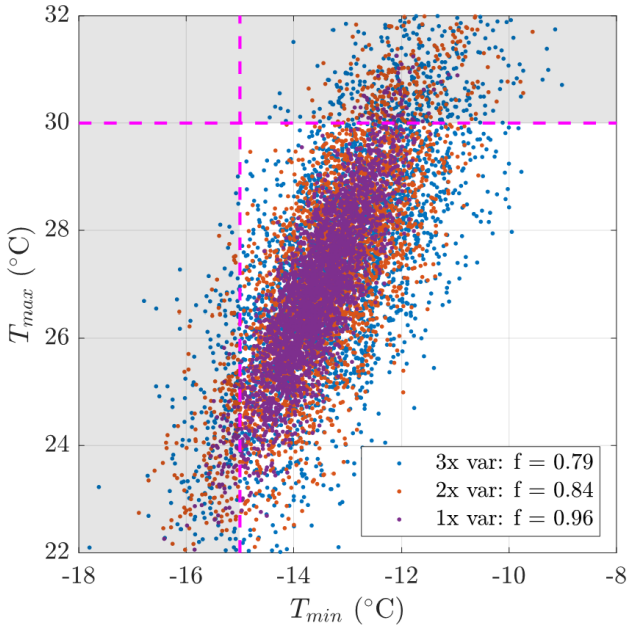

Figure 4-25: Temperature extreme variance of statically tailored robust solution for 3 levels of uncertainty model variance. Feasbility decreases quickly as uncertainty model variance increases.

By contrast, designs that rely on responsiveness and adaptability may offer a more graceful degradation of feasibility under growth of parametric uncertainty. Design 1, the PCM-dominant design, is evaluated under the same three uncertainty variance cases. Note, that for this demonstration, the electrochromic area coverage was increased from 11.1% to 15.7% (tailored for excess adaptability under 1x variance model). The corresponding distributions of temperature extreme outcomes are shown in Figure 4-26. As before, there is a decline in feasibility from the 1x variance case, however, the decline occurs at a much slower rate. Even under the 3x variance case, feasibility still stands at 88%. In Figure 4-26, it is also clear that in the higher variance cases, the majority of constraint violations occur at the maximum

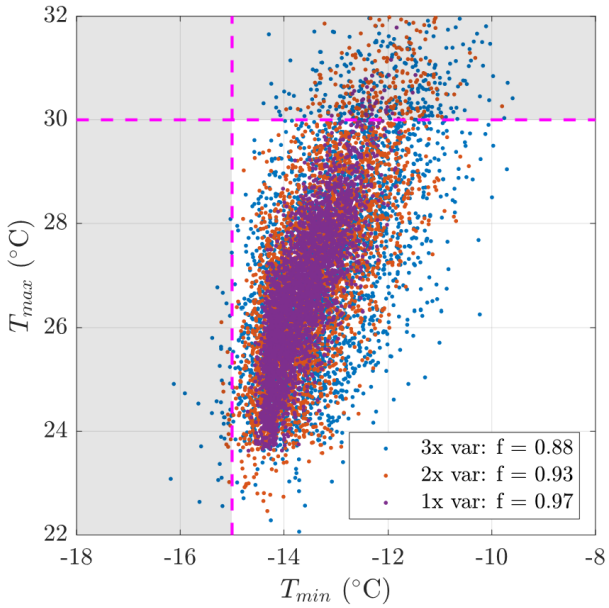

Figure 4-26: Temperature extreme variance of Design 1: PCM-dominant for 3 levels of uncertainty model variance. Degradation of feasibility occurs at slower rate than in static robust design.

temperature constraint. Recall from § 4.5.1 that the electrochromic and PCM mitigations were 'specialized'. PCM melting point was tailored to a relatively high phase transition point, focusing the responsive margin at the maximum temperature constraint. Electrochromic behavior was designed with a nominal center at 0.7, providing much greater dynamic range to decrease emissivity, thereby focusing the effect on mitigation of cases near the minimum temperature constraint. As variance in the uncertainty model is increased, the PCM response has a more limited effect. The tails of the distribution expand beyond the constraint, resulting in more violations. By contrast, the number of constraint violations near the minimum temperature constraint are few. Notably, the slight increase in adaptability (which came at no performance cost; only occupation of area) results in an enhanced ability to mitigate uncertainty.

In practice, there may be many other types of error that could require robustness (i.e., robust robustness or robust responsiveness and adaptability). Presented in this section is a simple parametric error in the uncertainty model. However, further errors

could be non-parametric in nature and could include unmodeled sources of uncertainty or model errors. Further exploration is needed to assess the efficacy of responsiveness and adaptability in the amelioration of such errors. Unlike in the case of parametric uncertainty, there is no guarantee that the existing mitigation techniques will have influence over the non-parametric uncertainties. In that scenario, other recourse would be necessary.

In this chapter, the methodology was applied in detail to a WaferSat design problem. The sensitivity to realistic thermal uncertainties was first highlighted. The sensitivity to uncertainty rendered the nominal optimal design unreliable due to a very low feasibility and the statically robust design sacrificed too much performance in favor of feasibility. The responsive and adaptive methodology was applied using three mitigations: responsive PCM, adaptive electrochromics, and adaptive thermal view factor control. Three isoperforming and isofeasible designs were identified, each utilizing a different combination of the three mitigations. Though three designs were specifically identified, they exist out of an infinite set of potential combinations of the three mitigation techniques explored. This offers multiple options for implementation where the 'costs' of each mitigation are considered, depending on the mission application. Missions where maximizing functional mass (i.e., silicon where electronics may be embedded) may require either Designs 2 or 3 with lower PCM allocation. Missions where surface area usage is critical may avoid solutions like Design 2 with a heavy devotion of external surface area to electrochromics. Missions where pointing of a payload or antennas is critical may preclude the reliance on view factor control as in Design 3. Finally, one of the designs was evaluated for robustness to errors in the uncertainty model. The design was originally designed under a set uncertainty model, but it was shown that it is possible to retailor adaptability to provide a guarantee of feasibility that is better able to tolerate increases in uncertainty.

Chapter 5

DiskSat

In addition to Wafersat, other flat form factor, high aspect ratio satellite concepts exist. One such example is DiskSat, a 1-meter diameter flat satellite in development at the Aerospace Corporation [14, 107]. As a similar high $\mathcal{AR}$ system, DiskSat shares some thermal sensitivity challenges with WaferSat, while offering some new options for thermal mitigations through its increase in mass. In this chapter, optimization with dynamic heat flows through several thermal zones in a DiskSat is presented. Additionally, the continuum between two options offering responsive robustness and adaptability is explored in greater detail.

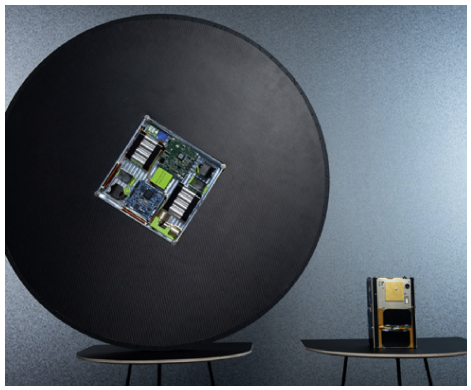

Figure 5-1: A 1 meter diameter DiskSat next to a 1.5 U CubeSat. The internals of a CubeSat are contained in a module in the center of the disk. [108]

5.1 $\mathcal{AR}$ Scaling Revisited

Recall from Chapter 1 that high $\mathcal{AR}$ systems have distinct advantages and disadvantages. For the thermal problem, the high aspect ratio contributes to a large radiative heat exchange surface areas relative to heat capacity. In the nominal nadir-facing attitude, at β angle of zero, the zenith surface is maximally exposed to the sun at times, and the nadir surface always has a maximized view factor to the Earth. At the same time, the large surface areas offer large areas to populate with solar cells, potentially creating a high-powered system.

As noted in § 1.2.2, high $\mathcal{AR}$ results in short thermal equilibration time constants. A DiskSat of 1-meter diameter and 25 mm thickness has an $\mathcal{AR}$ of 40 - lower than that of WaferSat, but still of a short thermal equilibration time constant. Assuming a total mass of 3.5 kg, the temperature response nears equilibration before the end of each orbital phase. An example of the near equilibration is shown in Figure 5-2 which depicts the temperatures over a single orbital period of a 400 km altitude orbit for a 3.5 kg mass (blue) compared to the thermal equilibrium (i.e., a zero-mass equivalent system, orange). Note that the extremes of the 3.5 kg wafer approach the extremes of the equilibrium temperature traces by the end of sunlight and eclipse phases; the 3.5 kg temperature amplitude is 94% of the amplitude of the equilibrium temperatures. DiskSat still lies within the short equilibration, high $\mathcal{AR}$ thermal design regime.

Whereas the thinness and high thermal conductivity of uniform silicon makes thermal gradients in WaferSat small, scaling up to a larger absolute thickness of DiskSat adds the possibility of designing for isolation of temperature sensitive components from the surfaces. In this Chapter, a DiskSat will be modeled as a multi-node system to design for temperature satisfaction of a select portion of the satellite in the presence of uncertainty.

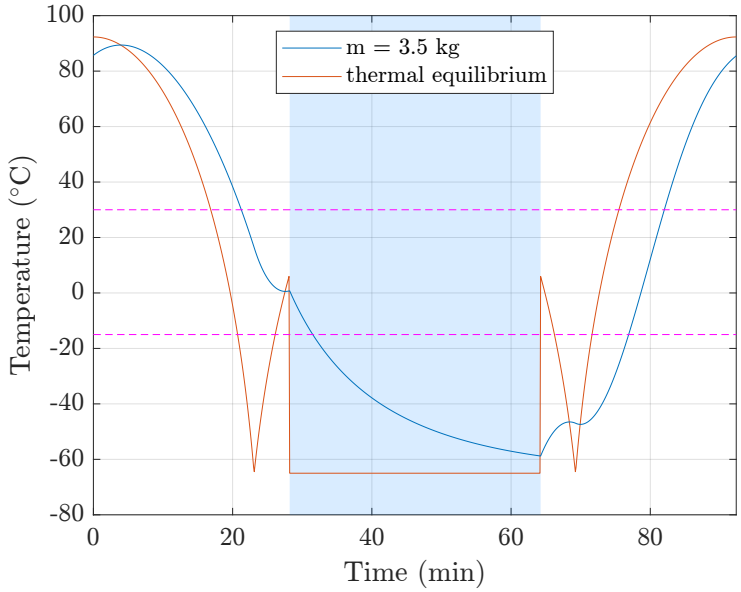

Figure 5-2: Thermal quasi-steady state of 3.5 kg DiskSat compared to thermal equilibrium. Modeled as a single-node in 400 km altitude circular orbit, β angle of 0.

5.2 Defining the Problem

Much like in the WaferSat example, the design optimization for DiskSat will focus on thermal survivability whilst maximizing power performance. This approach helps to realize one of the advantages of high $\mathcal{AR}$ systems: utilization of the large surface area available to generate power far above the norms for the weight-class of the satellite.

5.2.1 Multi-Node Thermal Modeling: Axial 1D Gradient

DiskSat has a diameter of 1 meter, and a thickness of 25 mm. Growth in the absolute thickness as well as the composition with sandwich composite materials may allow for thermal gradients through the thickness. As shown in Figure 5-3, the DiskSat will be modeled using three thermal regions: a zenith facesheet node (blue), a nadir facesheet node (yellow), and a mid-node between the facesheets (orange). It is assumed that all temperature sensitive components will be housed within this mid-node (limited once

again by the battery operational limits per § 4.1.2). The facesheets will be subject to much wider temperature constraints set by the solar cells.

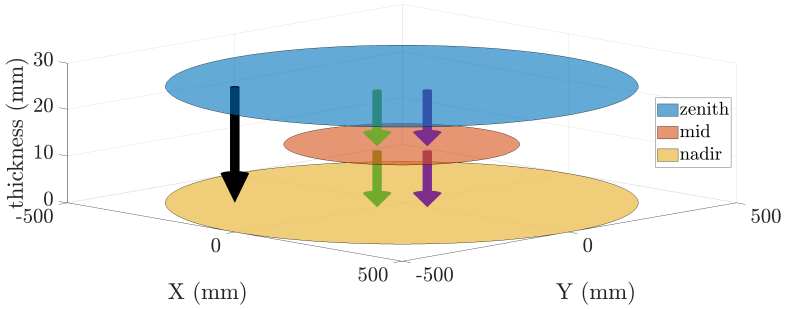

Figure 5-3: Zenith, mid, and nadir nodes. All internal-facing surfaces are coated with electrochromic surface. Arrows represent the following parallel heat paths: high conductive coupling between exterior facesheets (black), low conductive coupling from exterior facesheets to mid-node (green), and internal radiative heat transfer between exterior facesheets and mid-node (purple).

The aluminum facesheets covered with solar arrays and static thermo-optical coatings comprise the zenith and nadir surface nodes. It is assumed that the two facesheets are thermally conductively coupled (through the honeycomb composite structure). It is also assumed that the three nodes are equal in mass. The mid-node is composed of a centrally-located (radially, and longitudinally) disk of surface area equal to half of that of the facesheets. The mid-node is supported by polyimide aerogel posts of height 6.5 mm. To keep thermal conductivity low, the total polyimide post area on each side of the mid-node is equal to 25% of the mid-node area. is supported by polyimide aerogel posts. The remaining internal area between the mid-node and the facesheets is covered with electrochromic coating.

5.2.2 New Parameters for DiskSat

The orbital environment is assumed to be identical to that in the WaferSat problem. The changed parameters of the DiskSat problem are summarized in Table 5.1.

Table 5.1: Constant parameters used throughout the DiskSat problem

Parameter	**Symbol**	**Value**	**Units**
Radius	r_d	500	mm
Total thickness	t_d	25	mm
Total mass	m_d	3.5	kg
facesheet thickness	t_f	1	mm
mid-node thickness	t_m	10	mm
mid-node radius	r_m	393	mm
Zenith node mass	m_z	1.17	kg
Nadir node mass	m_n	1.17	kg
mid-node mass	m_m	1.17	kg
Specific heat capacity of Al	c_p^{al}	903	$\mathrm{J\,kg^{-1}\,K^{-1}}$
Thermal conductivity of Al	k_{al}	167	$\mathrm{W\,m^{-1}\,K^{-1}}$
Thermal conductivity of polyimide aerogel	k_a	0.029	$\mathrm{W\,m^{-1}\,K^{-1}}$
orbit altitude	h	400	km

5.2.3 Internal Facing Electrochromics for Adaptive Heat Flow

In contrast to the WaferSat example where electrochromics were used to compensate for heat flows in and out of the system, electrochromics will be used for the DiskSat problem to redistribute heat among the three nodes: zenith, mid, and nadir. As the temperature sensitive components are assumed to reside solely in the mid-node, the zenith and nadir nodes are not under temperature constraints. As such the electrochromics are used to regulate the thermal radiative coupling of the mid-node to the two surface nodes rather than external heat flows.

The operation of the internal facing electrochromics is shown in Figure 5-4. Shown in Figure 5-4a are the temperatures of all three nodes (left y-axis) and the electrochromic internal face adaptive behavior (purple, right y-axis). The blue and yellow traces represent the external facesheets. High thermal conductance between the two makes for a nearly isothermal set of surfaces in thermal view of the mid-node. The zenith and nadir facesheets are not subject to the temperature requirements in magenta dashed lines. The mid-node in red, is regulated by the electrochromic surfaces shown in purple (right y-axis). Electrochromic values are optimized to minimize

changes in temperature. Note that the directions of heat flow cannot be changed with electrochromics (second law of thermodynamics), however, the magnitudes of heat flow can be regulated - increasing heat flow when a favorable directional gradient exists and isolating when unfavorable. There is greater coupling when the direction of heat flow is favorable and low coupling when unfavorable.

The corresponding net radiative flows of heat due to electrochromic operation between the three nodes is shown in Figure 5-4b. Note that by convention, heat flows from the zenith to nadir direction are positive. The near thermal coupling of the zenith and nadir wafers results in mirrored heat flow traces as the values of emissivity of the electrochromics on the internal surfaces area are identical.

Recall from Chapter 4, that electrochromic operation results in three instantaneous states: saturation low, saturation high, and exact compensation. These three modes are again seen, with different effects in Figure 5-4a. In the internal face configuration, saturation low represents the least radiative coupling (radiative heat flows as low as possible). Saturation high represents the most radiative coupling. In this configuration, exact compensation results in constant temperature of the mid-node. This is seen in two places: the peak mid-node temperatures and just after re-emergence from eclipse. At these two temperature extremes, the internal face emissivities of the mid-node can exactly regulate the heat flows to minimize changes in temperature. Since it is assumed that the temperature requirements do not apply to the external nodes, they are treated as sources and sinks of heat strictly for the regulation of the mid-node. The behavior of prolonging the constant temperature period lengthens the effective time to reach the opposing temperature constraint (the temperature-pause is similar to the effect of PCMs).

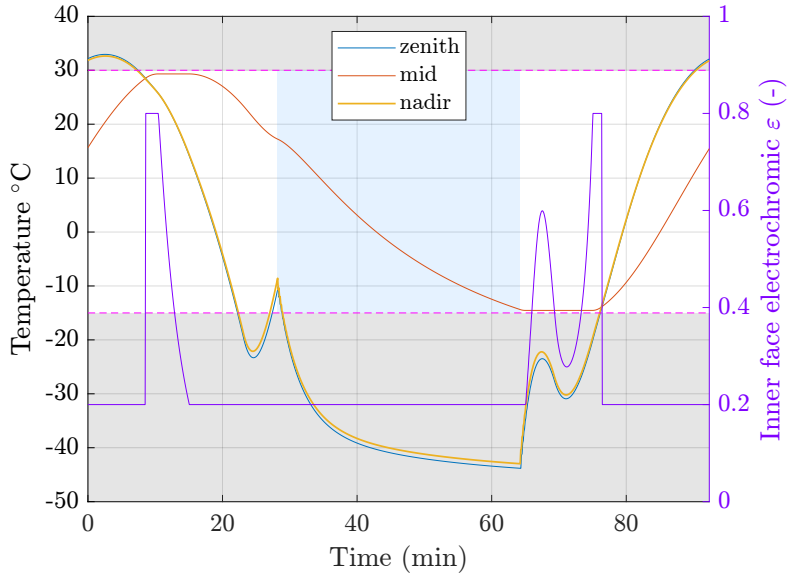

(a) Temperatures of the three DiskSat nodes (left axis) and inner face electrochromic emissivity adaptive response (right axis, purple)

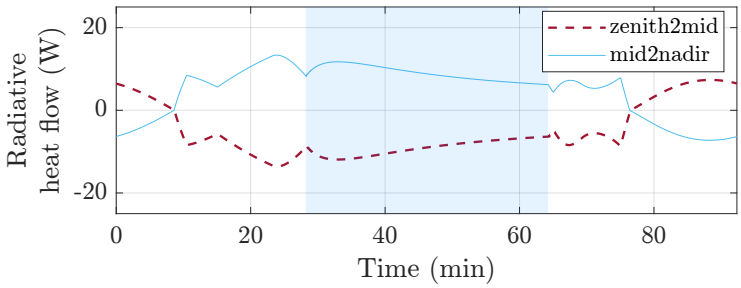

(b) Net radiative heat flows between nodes, regulated by electrochromic emissivities

Figure 5-4: Internal face electrochromic regulation of mid-node temperatures through adaption of radiative heat flows.

5.3 Responsive Robustness vs. Adaptability

As noted in Chapter 4, there are multiple combinations of static robustness, responsive robustness, and adaptability that can equivalently provide the same performance and statistical guarantee under modeled uncertainty. The three designs identified in the WaferSat case represented distinct emphases on one of three mitigations, each representing unique designs. There are, however, an infinite number of designs between with different relative reliance on each of the three mitigations. In this

section, the continuum between the adaptive internal-facing electrochromics and responsive mid-node PCM is explored.

5.3.1 A continuum from most adaptive to most responsive

In the continuum between electrochromic adaptability and PCM responsive robustness, there are two extremes. At one end is a design that achieves the desired performance and feasibility levels entirely through adaptability, and at the other extreme, a design that is correspondingly fully responsively robust. Between these extremes lie the combined designs with varying emphasis or reliance on the two mitigations.

In this DiskSat example, a fully adaptive design would achieve the power performance and feasibility through mitigation of thermal uncertainties purely through the adaptive, electrochromic compensation of heat flows in and out of the middle node. The magnitude of compensatory range is a function of internal face electrochromic fill factor and dynamic range of the electrochromics. However, with the constraints of this problem, a fully adaptive design is not possible. Instead, there is a most adaptive design - mitigating uncertainty mostly with adaptability, and providing responsive margin with a small amount of PCM.

As PCM mass is added to the most adaptive system, responsive robustness increases, lessening the need for adaptive heat flow range, i.e., the maximum magnitude of adaptive heat flow can decrease. To identify solutions along the continuum, the comparative usage of both mitigations is simultaneously varied while maintaining isoperformance and isofeasibility. Results are shown in Figure 5-5, with the PCM mass shown along the x axis and the corresponding required maximum (red) and minimum (blue) electrochromic range of the internal faces. From the most adaptive solution, as more PCM mass is added to the system, the dynamic variables that governing the electrochromics are adaptively retailored to reduce the electrochromic range utilized.

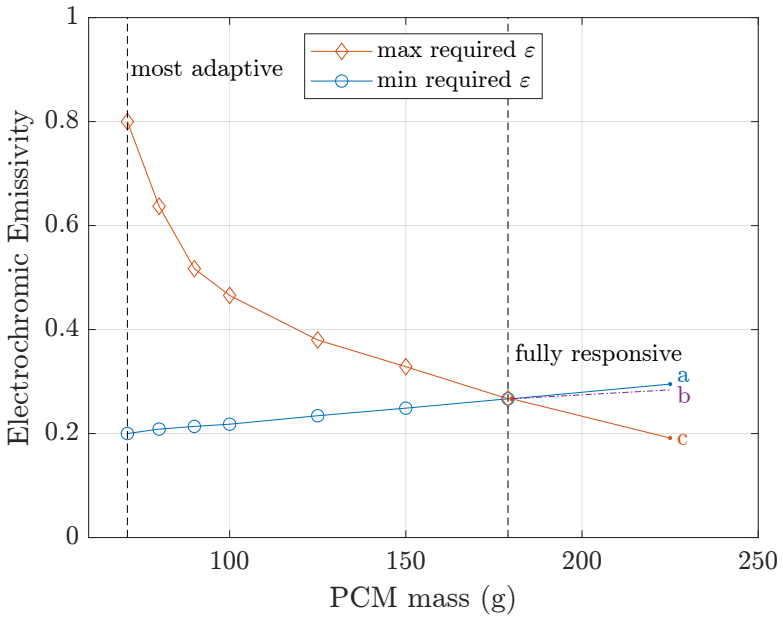

Figure 5-5: Continuum from most adaptive to fully responsive robust. Tailorable excess responsive robust margin cases: (a) cold-limited 2-σ feasible; (b) balanced 2-σ+ feasible; (c) hot-limited 2-σ feasible

In this first example, PCM is added with constant temperature of fusion, $T_f = 7.5°\text{C}$ - selected as the mean of the temperature constraints (roughly corresponding the melting point of Pentadecane). Notably, as more PCM as added, there is asymmetry in the rates of decrease in the minimum and maximum electrochromic limits. In other words, the latent heat storage affords greater responsive margin to the maximum temperature constraint. As such, the need for high emissivity (thermal coupling) between nodes is reduced.

In Figure 5-5, the most responsive design occurs at around 179 g of PCM, where the maximum and minimum required values of electrochromic range meet at $\varepsilon = 0.26$. At this point, there is no requirement for any adaptive adjustment of the internal face emissivities. All internal facing surfaces can assume the constant value of $\varepsilon = 0.26$ and the PCM responsive margin will mitigate the effects of uncertainty for 2σ feasibility. Note, that $\varepsilon = 0.26$ is the only value of static emissivity that is permissible. If more PCM mass is added, there will be excess responsive margin. An example point is shown at the rightmost edge of Figure 5-5, where 225 g of PCM mass is added.

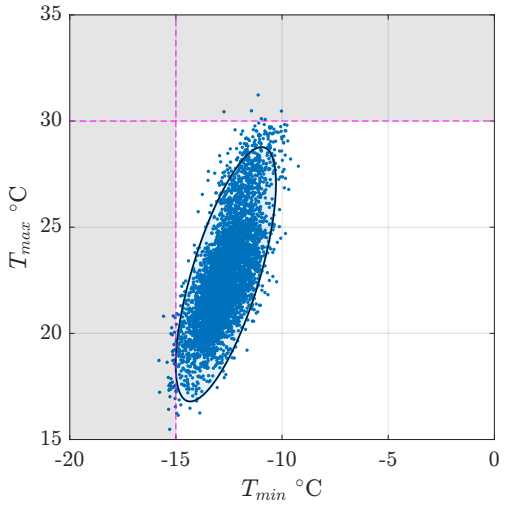

(a) Maximum allowable static internal face emissivity, $\mathbb{P}_{feas} = 0.954$, $\varepsilon_{static}^{high} = 0.295$

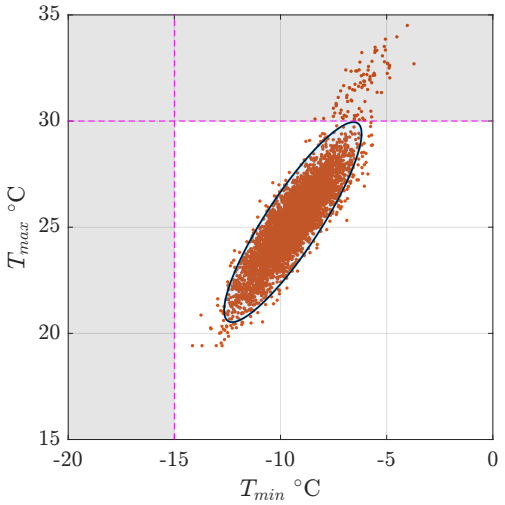

(b) Minimum allowable static internal face emissivity, $\mathbb{P}_{feas} = 0.954$, $\varepsilon_{static}^{low} = 0.191$

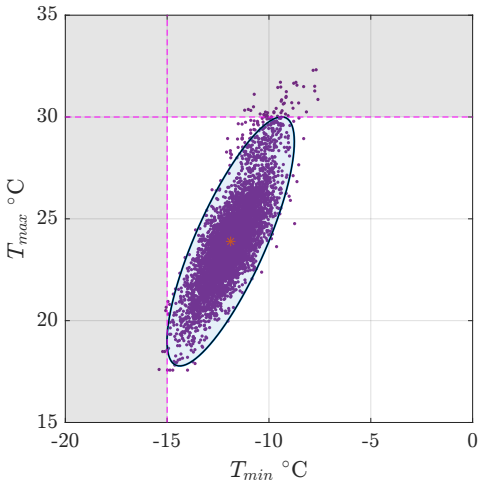

(c) Maximized and balanced constraint satisfaction, $\mathbb{P}_{feas} = 0.983$, $\varepsilon_{static} = 0.284$

Figure 5-6: Comparison of tailored margin in three cases: minimum temperature constraint, maximum temperature constraint, balanced.

With excess PCM, there is now a range of permissible static internal face emissivities that are permissible whilst maintaining $\geq 2\sigma$ feasibility. The limits of the range, correspond to violation of one of the constraints. The maximum value of $\varepsilon_{static}^{high} = 0.295$ represents the cold-limited case, shown in Figure 5-6a. There is still excess margin against the maximum temperature constraint, but the 2σ error ellipse is limited by the minimum temperature constraint. Conversely, the lower static limit, $\varepsilon_{static}^{low} = 0.191$ is

limited by the maximum temperature constraint as shown in Figure 5-6b and there is excess responsive margin against the minimum temperature constraint. There is a third point, shown in purple, which represents the balance point of responsive margin. At this point, where $\varepsilon_{static} = 0.284$, the responsive margin is distributed so as to maximize the error ellipse size and simultaneously meet the temperature requirements. This is shown in Figure 5-6c where the ellipse is tangent to both temperature requirements and the ellipse is maximally sized to provide a feasibility rate of 98.3%. This point represents the optimal retailoring of excess margin under these conditions.

5.3.2 Balancing Adaptive Authority

In the previous continuum, PCM mass was added at a constant melting temperature - arbitrarily selected as the mean of the temperature requirements. As PCM mass was added, the limits on electrochromic range asymmetrically decreased. In order to balance the rate of decrease of reliance on electrochromic adaptability, the phase transition point of the PCM can be retailored as mass is added. A new continuum is shown in Figure 5-7 where the blue and red points again represent the effective limits on the required range of electrochromic emissivity (corresponding to the left axis). The purple plot - which corresponds to the right axis - shows the retailored temperature of fusion T_f as PCM mass is added. In this scenario, as PCM mass is increased, the temperature of fusion decreases. As noted in the operation of PCM in Chapter 4, decreases in the phase transition point can re-allocate the responsive margin to the lower temperature constraint. This focusing of margin on the lower constraint allows for rebalancing of required electrochromic range relief.

In this balanced scenario, the required limits on the electrochromic range decrease at an even rate, meeting at a static value of 0.5. The even decrease in range can allow for a decrease in electrochromic area on the inner surfaces while maintaining equal adaptive authority on the maximum and minimum temperature constraints. Note

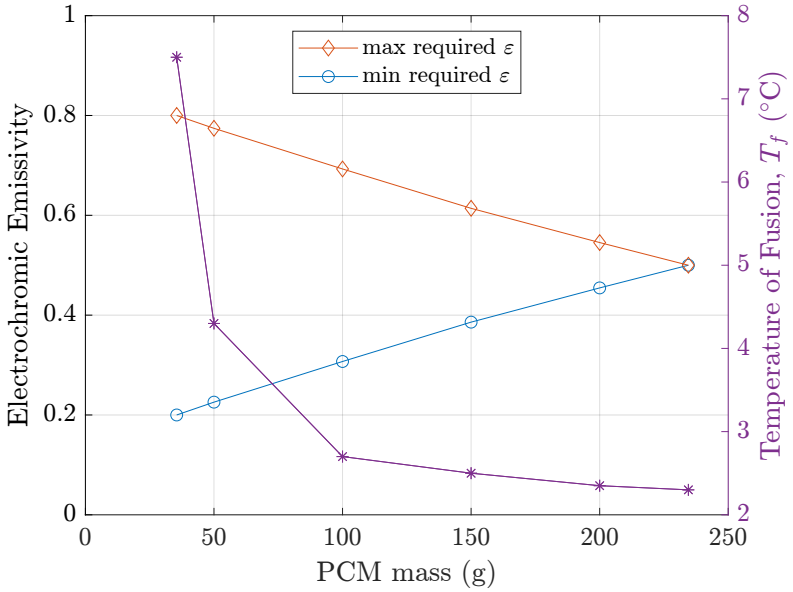

Figure 5-7: Retailoring of PCM temperature of fusion to balance required electrochromic range

however, that the decrease in electrochromic range requires greater mass of PCM. The fully responsive design occurs at a PCM mass of 234 g compared to the 179 g in the constant T_f scenario. The greater PCM mass required to evenly decrease the reliance on electrochromics presents a 'balancing cost'. The new temperature of fusion may now occur at a temperature where the heat gradients are greater, resulting in faster heat flows at constant temperature, and therefore shorter period of phase change. The net result is that each gram of PCM results in a shorter thermal time constant increase. In exchange for responsive margin balancing, the effectiveness of PCM operation is reduced.

The time constant increase due to PCM mass is longest when the temperature of fusion occurs at a period with low rates of net heat flow. Typically, this occurs near the extremes in temperature where the slope is lowest. This however, narrowly focuses the effect of the responsive margin near the corresponding temperature constraint. In cases where PCM is used alone or as the dominant thermal mitigation, the effect should be evenly distributed among the active, performance-limiting constraints. Such was the case in Design 1 of § 4.5.1. As a PCM-dominated design, the temperature

of fusion was at a moderate value in the temperature range, so as to elicit responsive margin at both constraints. However, by comparison in Designs 2 and 3 in §§ 4.5.2 and 4.5.3, the temperature of fusion was very close to the minimum temperature constraint. In these cases, the PCM responsive margin served to augment the effects of other thermal mitigations, narrowly providing margin in a specific location. There was some specialization of effects on specific constraints by specific mitigations.

5.4 Seasonal robustness: variation in β angle

In addition to random thermal uncertainties, a DiskSat may encounter seasonal thermal variance. Notably, the β angle, or the angle between the Earth-Sun vector and its projection onto the orbit plane will vary as a function of time. Thus far, all analyses have assumed a β angle of 0, corresponding to the worst-case thermal conditions with longest eclipse and greatest net solar incidence on the zenith surface when in the nominal nadir-facing orientation.

The variation in β angle is given by,

$$\beta = \arcsin\big(\cos(\Gamma)\sin(\Omega)\sin(i) - \sin(\Gamma)\cos(\epsilon)\cos(\Omega)\sin(i) + \sin(\Gamma)\sin(\epsilon)\cos(\Omega)\sin(i) + \sin(\Gamma)\sin(\epsilon)\cos(i)\big) \quad (5.1)$$

where Γ is the position of the Earth in orbit about the sun relative to a reference point when the β angle is zero, Ω is the longitude of ascending node, i is the orbit inclination, and ϵ is the angle of the Earth ecliptic. The bounding extremes of β angle are limited by the inclination and the angle of the Earth ecliptic,

$$|\beta_{max}| = \epsilon + |i| \quad (5.2)$$

The mid-node extreme temperatures and internal power are shown as a function

of β angle in Figure 5-8. The mid-node extremes are shown in red, corresponding to the left axis. Internal power is shown in purple, corresponding to the right axis. As β angle increases, the maximum mid-node temperatures decrease, with the exception of a few points near 72°. The general decrease in temperatures is the result of a decrease in solar exposure in the warmest points in the orbit (since the DiskSat remains nadir-facing). The mid-node minimum temperatures are slightly more stable; there is a slight decrease in minimum temperature until about 40°. There are two opposing effects: the minimum temperatures are exacerbated by the sharp decrease in maximum temperatures, but also mitigated by the shortening of eclipse. As eclipse nears a length of zero, the amount of internal power sharply increases. This is shown in Figure 5-9, the various sources of power: zenith solar array direct and albedo, nadir solar array direct and albedo for four β angles. As the length of eclipse shortens, the direct illumination of the nadir-side increases, resulting in a dramatic increase in power (noting that the nadir side of the DiskSat has nearly 70% coverage with solar array). As a result, at a β angle of 71°, when eclipse reaches a length of zero, power is greatest and the temperatures of the mid-node increase in both the minimum and maximum states. Beyond this point, the internal power and temperatures sharply

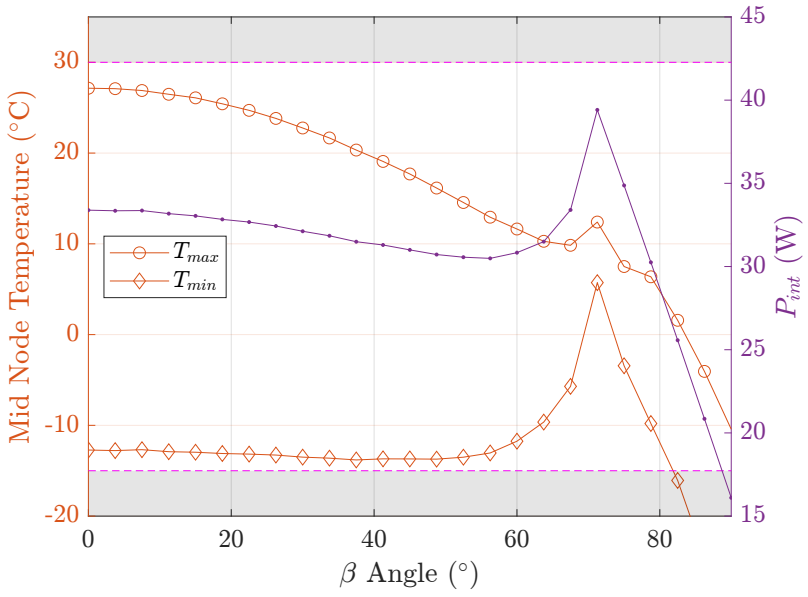

Figure 5-8: Variation of power and mid-node extreme temperatures with β angle

decrease as the DiskSat is then nearly pointed edge-on to the sun.

In particular for smaller β angles, the design exhibits robustness to the seasonal variation in β angle. The optimization was performed for the most constraining thermal conditions at $\beta = 0$. The reliance on solar array area on the nadir surface provides thermal robustness by limiting the emissivity of the zenith surface which is thermally advantageous as the β angle increases and the surface points to free space with limited solar exposure. Furthermore, the large area of nadir solar array also limits the drop off in power is β angle increases through smaller angles. Albedo-reflected sunlight - though much lower in flux - has a slower rate of decrease as β increases. As a result, for relatively low inclination orbits, nominal seasonal power loss is limited. Note that this analysis assumes that the DiskSat remains strictly nadir-facing. With attitude control, there are more options for maintaining or increasing power seasonally as β changes.

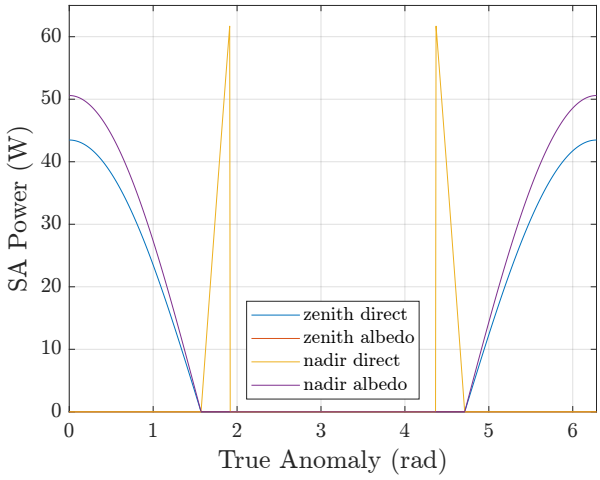

(a) $\beta = 0°$; most of power generated from zenith direct, nadir albedo

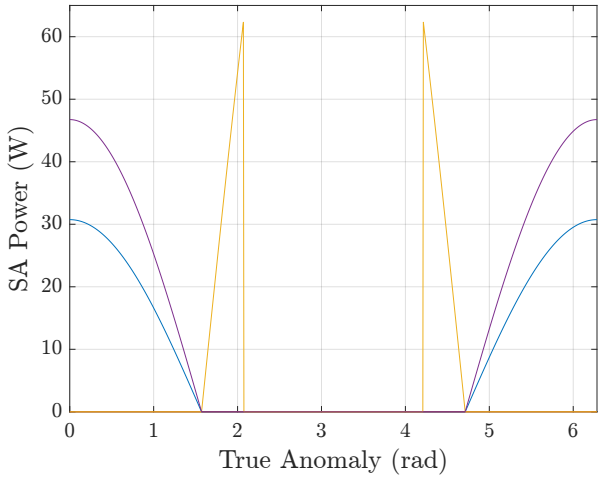

(b) $\beta = 45°$, greater share of power from nadir solar array

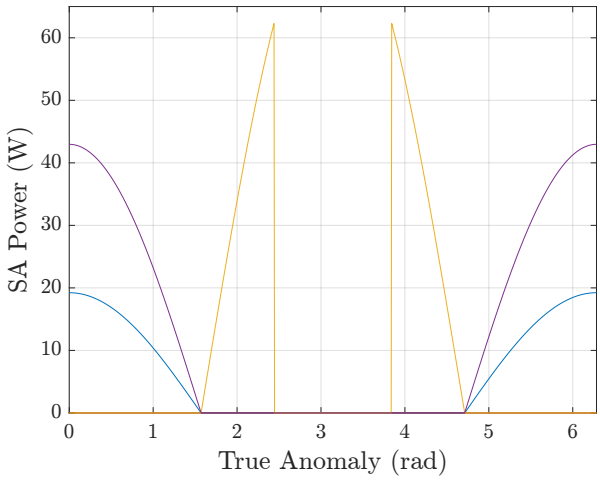

(c) $\beta = 63°$, increasing amount of power from nadir direct illumination, eclipse shortens

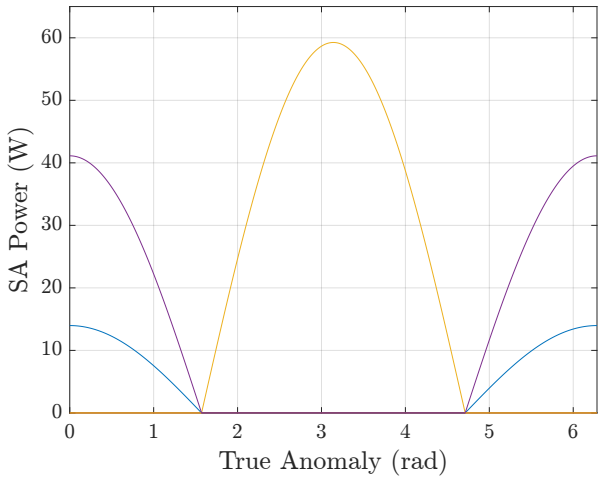

(d) $\beta = 71°$, nadir direct illumination is greatest source of power

Figure 5-9: Power generation for various β angles

Usage of nadir area for solar power generation tends to be favorable thermally for many β angles. The reduced heat flux of the nadir surface (pointed at the Earth) makes it worthwhile despite the reduced effective power generation due to losses from albedo reflectance.

5.5 Analysis of Radial Gradients

Due to the large surface area, it is likely that a DiskSat might have temperature gradients across the surface. The spatial locations of the dissimilar thermo-optical surfaces may result in variation of rates of heat absorption and rejection and therefore gradients across the surface of DiskSat. A method for accounting for these gradients is proposed in order to limit the effects of high thermal flux (high α, high ε) surfaces on the mid-node temperatures.

Thus far, it has been assumed that the net surface heat fluxes are uniform across the surface of the DiskSat, resulting in uniform temperature distributions across the span. To increase fidelity, the model can be expanded to include assumed spatial locations of the different known thermo-optical surfaces and coatings. To simplify this analysis, it is assumed that the DiskSat exhibits azimuthal symmetry. Therefore all gradients are in the radial direction. All temperature sensitive components are assumed to be housed in a mid-node in a region at the center of the DiskSat. Since it is known that the solar array area is high in radiative heat flux (it is high in both emissivity and absorptivity), the solar array area is assumed to be composed in an annular ring at the edge of DiskSat. In this way, the highest flux surfaces are spatially furthest from the temperature sensitive components; i.e., there is a long conductive path length in the radial direction and greatest potential for thermal isolation.

An example of thermo-optical zones is shown in Figure 5-10. All temperature sensitive components - namely the batteries - are located within the blue 'avionics area'. The solar array is denoted by the green annulus along the edge. The gray

region represents the area devoted to static thermo-optical surface coatings (and is statically tailorable).

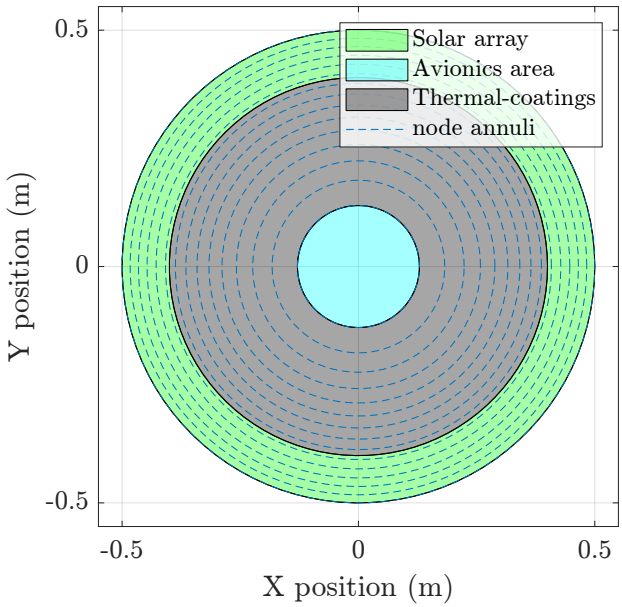

Figure 5-10: Surface of DiskSat with non-homogeneous thermo-optical surfaces. Temperature is evaluated at the annular nodes.

To estimate the thermal gradients, a finite differencing scheme is used, as shown in Equation 5.3. The temperature of the i^{th} node includes conductivity to adjacent nodes for $i \in [1, n]$. At each annular node, the net external heat flow terms (radiation, solar exposure, albedo, EIR, internal conductivity) are functions of local thermo-optical properties. As the nodes are constant-mass annuli, the radial spacing is non-uniform. Spacing is calculated recursively as shown in Equation 5.4, for the total number of nodes, n, and DiskSat facesheet surface area, A_D. An example spacing of node edges is shown with dashed lines in Figure 5-10.

$$\frac{\partial^2 T(r)}{\partial r^2} \approx k_r \left(\frac{T_{i+1} - T_i}{\Delta r} - \frac{T_{i-1} - T_i}{\Delta r} \right) = q_{net} = P_i^{rad}(T_i) + P_i^{sol} + P_i^{alb} + P_i^{eir} + P_i^{con} \tag{5.3}$$

$$r_i = \begin{cases} \left(\frac{A_D}{n\pi}\right)^{0.5} & , \quad i = 1 \\ \left(\frac{A_D}{n\pi} + r_{i-1}^2\right)^{0.5} & , \ 1 < i \leqslant n \end{cases} \tag{5.4}$$

A comparison of the quasi-steady state temperature oscillation of the facesheets over one orbit is shown in Figure 5-11. The temperatures at the outermost disk edge - in the solar array area annulus - is shown in green. The outer edge of the area directly over the avionics is shown in blue. Due to the much higher absorptivity and emissivity of the outer edges, the heat flows are much greater, resulting in much larger temperature variation. Recall also from the earlier DiskSat analysis that the zenith and nadir facesheets are thermally conductively coupled, but isolated from the mid-node where the batteries are located (along with other temperature sensitive components). Note that the extent of the temperature range of the avionics facesheet area is now lower than under the quasi-uniform assumption (shown in Figure 5-4a). In this scenario, the lower temperature oscillation of the avionics area - directly over the mid-node - presents internal surfaces that have a lower heat variance. The mid-node now has a long effective heat path to the most variable heat surfaces, the solar arrays.

Incorporation of radial gradients could allow for a higher fidelity thermal model - particularly by accounting for the distribution of heats for dissimilar surface thermo-optical properties. The finite difference scheme presented may be used, or alternatively, a higher fidelity modeling program using finite element modeling in a full three dimensional model may be used. The increase in fidelity would present some new considerations for optimization as well as new design variables.

If incorporating a higher fidelity multi-node model in the optimization of DiskSat, the design of surfaces would be expanded to include a spatial component. That is, when designing surface coatings, the spatial location on exterior surfaces would be introduced as new design variables. In addition to the tailoring of surface thermo-optimal properties, the location of specific thermo-optical surfaces could be used to

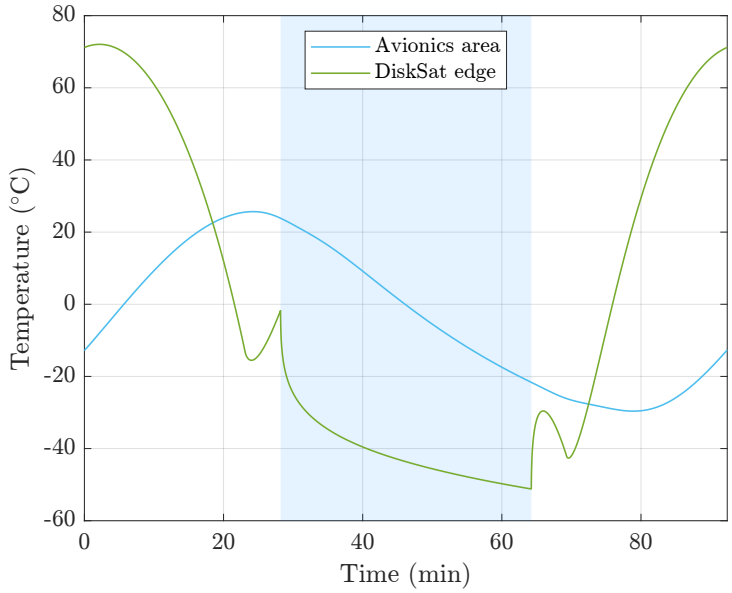

Figure 5-11: Temperatures of facesheets: DiskSat solar array-covered edge node (green), DiskSat center area directly above avionics (blue).

create favorable thermal gradients. The optimization of the spatial design could be approached using the level set method introduced by Cohen [109].

The addition of the spatial design of surfaces and corresponding thermal gradients will result in additional considerations for the optimization. In the radial gradient example, the large gradients will result in deformations due to coefficient of thermal expansion (CTE) mismatches. There may be additional constraints on the optimization to limit any thermal gradients that may cause significant deformation (in the radial gradient scenario: bowl-shaped bowing of DiskSat). This set of structural constraints would be at odds with the thermal spatial objective of creating large gradients from the high heat flux surfaces to the batteries. As a result, the optimization might need to balance these new criteria, increasing the scope of modeling to include other subsystems. The approach to the mitigation of new constraints, however could still follow the presented methodology.

Chapter 6

Conclusion and Future Work

Traditionally, when optimizing systems that are sensitive to uncertainty, the designer suffers a dilemma. Nominal optimal, as tantalizing as it may be, offers no reliability under uncertainty. Statically robust designs can increase feasibility under uncertainty through desensitization and margin, but robustness comes at a cost. Some optimality must be sacrificed in order to allocate finite resources to create margin. This problem is exemplified by high $\not{R}$ systems like WaferSat and DiskSat with their high sensitivity to thermal uncertainty. In this work, a methodology has been presented to design for the combination of responsiveness and adaptability to mitigate uncertainty in operation. By creating a dynamic response to states of uncertainty as they are realized, feasibility can be improved with limited nominal performance sacrifice.

Responsiveness is a passive, fixed-recourse response to uncertainty in operation. The response behavior is defined and constrained by the design of the governing dynamic variables, set in the a priori design phase before operation. As states of uncertainty are realized, a dynamic response - such as the change in phase of a material - provides responsive margin, mitigating the effects of uncertainty. Tailoring of the response ensures that the responsive behavior aids in the mitigation of the uncertainty on hand. Adaptability is an active compensation to states of uncertainty in operation

involving a two stage design process. As with the responsive design, dynamic variables that govern the adaptive behavior are set in the a priori phase. The initial design defines the adaptive behavior - specifically the authority of the adaptability. The adaptive behavior under states of uncertainty must then be optimized to maintain feasibility of active constraints. Changes in uncertainty in-situ can be further mitigated through changes in the adaptation, effectively re-programming the mitigation as-needed. Together, responsiveness and adaptability allow for the mitigation of the perturbing effects of uncertainty with a two-stage optimization. On the outer loop, static and dynamic variable sets are optimized with a maximum performance objective. In the inner loop, candidate designs are evaluated under an ensemble of uncertain states. In the inner loop, the responsive behavior is propagated, and adaptability is optimized to maximize feasibility of the active constraints. Feasibility is passed back to the outer loop to evaluate against desired feasibility criteria. The optimization process results in a design (or set of designs) that provide the maximum performance with desired feasbility under the modeled uncertainty set. The process both designs for responsiveness and adaptability as well as optimizes the adaptive response to individual states of uncertainty.

6.1 Thesis Contributions

The contributions of this thesis are summarized as follows:

1. Created a framework of responsive robust and adaptive mitigation of uncertainty with limited performance sacrifice

2. Developed a two-stage optimization methodology for the prior design for and operational design of responsiveness & adaptability

3. Application to WaferSat: Demonstrated identification of unique designs of equal performance and feasibility

4. Application to DiskSat: Explored tradeoff between responsiveness & adaptability

In Chapter 3, a framework was introduced to design for responsive robustness and adaptability to mitigate the effects of uncertainty. Through continuous compensation for uncertain states of the world as they occur, margin is dynamically allocated, reducing the need for the sacrifice of performance in traditional robust design approaches with static margin. Throughout the chapter, a methodology is developed, building upon traditional robust approaches and expanding to incorporate the responsive and adaptive framework. The methodology culminates in a two-stage optimization process that enables the combined design of modeled responsive and adaptive mitigations. Simplified examples of responsiveness and adaptability are presented.

The methodology is then brought to bear in Chapter 4 in the design of a WaferSat in LEO. The WaferSat is subject to two sources of thermal uncertainty: localized Earth effective black body temperature and albedo variance. The models of uncertainty are modeled as ensembles of uncertain states based on local sliding window measurements from LEO from NOAA and NASA CERES project missions. The sensitivity of WaferSat is demonstrated and three mitigations are introduced. Phase change materials offer a responsive, fixed-recourse through latent heat absorption associated with changes in phase. Electrochromic surface coatings allow for an at-will selection of surface mid-IR emissivity and absorptivity resulting in tuneable radiating surfaces to regulate heat flows. Finally, spacecraft attitude is adjusted to modify thermal view factors and incident heat fluxes. When optimizing, several design families are identified that are both isoperforming and isofeasible under the modeled uncertainty set. Differing constraints on the 'costs' of implementation of each adaptive or responsive mitigation guides the design to a combination more suited to the needs of a specific mission.

In Chapter 5, the continuum between a responsive mitigation and an adaptive mitigation is explored in more detail. DiskSat is modeled as a three node system in which the mid node is constrained in temperature and the zenith and nadir nodes are unconstrained. PCM in the mid node offers responsive margin and a system of internal facing electrochromics allows for adaptive radiation of heat between the

nodes. The design space from most adaptive to most responsive is shown, highlighting the continuous tradeoff between. Modeling of the radial gradients is presented and a path forward for greater fidelity of surface spatial design and three dimensional discretization is suggested.

6.2 Future Work

The work of this thesis presents a methodology for the responsive and adaptive mitigation of uncertainty in operation. The methodology is demonstrated on two high $\mathcal{R}$ systems, but there are many areas for further development. The design of the WaferSat and DiskSat systems focused on the thermal constraints and power performance - both highly sensitive aspects of the high $\mathcal{R}$ design regime. It would be useful to expand the modeling and methodology to design over more spacecraft subsystems jointly. Specifically, the design over more subsystems may offer greater flexibility to dynamically allocate margin among subsystems, and possible change the sets of active constraints. Similarly - as suggested in § 5.5 - as the complexity of the system and integrated modeling grows, higher fidelity methods may be useful to capture more system effects.

As noted in § 4.6, adaptability may offer opportunities to redefine behavior in the event of errors in the predicted, modeled uncertainty used in the optimization. Design under a simple parametric error in the uncertainty models was explored, however, more types of unknown unknowns may exist. Further exploration of responsive and adaptive design is warranted for potential mitigation of non-parametric uncertainty such as unmodeled sources of uncertainty and model error.

In this work, the simulation of effects of uncertainty occurs over several orbits. However, the MC simulation could be extended to model longer term effects such as parts degradation over a mission lifetime. Though this would increase the amount of computation, it could be used to plan for the mitigation of expected degradation

as the mission progresses. One such example is the darkening of solar cell coverglass from ultraviolet exposure over time. If modeled over time, adaptive methods could be devised to mitigate the power generation reduction in the later stages of the mission. Furthermore, other off-nominal scenarios such as random parts failures could also be simulated. Once again, mitigations could be designed and modeled for credible types of failures to maintain operability.

WaferSat and DiskSat were used as examples for application in this work extensively due to their unique high $\mathcal{AR}$ design regime and sensitivity to thermal uncertainty. As relatively small, SWaP-limited systems, improving feasibility without sacrificing significant performance was critical. The methodology could also be applied to systems where the design difficulty is derived from the challenging environment as opposed to the SWaP or $\mathcal{AR}$. Such an example might include larger, deep space satellites, where responsiveness and adaptability may improve survival and operation further from the Sun while reducing overdesign due to large allocations of static margin. Incorporation of more options for both responsive and adaptive mitigation could allow for more comparisons and trades of enhanced feasibility versus implementation considerations.

Finally, it would be particularly useful to demonstrate some of the responsive and adaptive mitigations with hardware in a flight-like test environment for validation. Beyond that, a flight demonstration mission, perhaps on a set of WaferSats in LEO, could show the benefits of responsive and adaptive mitigation of uncertainty while maintaining performance.

Appendix A

Thermal Model Validation Cases

To provide a validation, results from the thesis MATLAB model are compared against published results from literature. In particular, the model is compared to two scenarios that bear similarities to the high $\mathcal{R}$ form factor of WaferSat and DiskSat thermally. The first scenario includes analysis of sun-facing solar cells that are thermally isolated from the rest of the spacecraft. The second case is an analysis of blank silicon wafers in LEO. In addition, all results are compared with a Thermal Desktop model run on the SSL lab computer [1].

A.1 Modeling Thermally Isolated Solar Arrays

A large deployed solar array that is thermally isolated from the rest of the spacecraft provides a valuable analog for the model of a flat, high $\mathcal{R}$ system. Kim, et al., [37], provide a detailed analysis of such a scenario for a sun-tracking orbit configuration over various β angles. This provides a validation case for two elements: the thermal modeling with extraction of electrical power from incident solar irradiance (resulting

[1] Special acknowledgment to UROP Ceylan Ceylan for her assistance in running many scenarios in the Thermal Desktop model.

in less thermal heating) and the temperature variation of a sun-facing, high $\mathcal{R}$), thermally isolated unit. Note that the solar power is assumed to be dissipated on the main spacecraft bus, thermally isolated from the cells. Therefore, the incoming solar irradiance converted to energy effectively leaves the solar array system thermally (unlike in WaferSat or DiskSat where the internal power dissipation occurs in the high $\mathcal{R}$ system).

In [37], the deployed solar array is modeled as a sun-tracking system; i.e., the solar array surface normal is aligned with the solar flux vector. This orbit is shown pictorially in Figure A-1. The reference orbit has a solar β angle of 30°. Note that the solar array is sun-tracking in the sun, but reverts to a solar array backside nadir-facing orientation during eclipse. The model parameters are summarized in Table A.1.

Table A.1: Summary of parameters for solar array thermal modeling from [37]

Model Parameter	**Symbol**	**Value**	**Units**
solar beta angle	β	30	°
solar array efficiency	η_{SA}	0.224	-
solar array absorptivity	α_{SA}	0.920	-
solar array emissivity	ε_{SA}	0.696	-
backside paint absorptivity	α_b	0.39	-
backside paint emissivity	ε_b	0.88	-
Earth albedo	a_E	0.35	-
orbit altitude	h_o	400	km

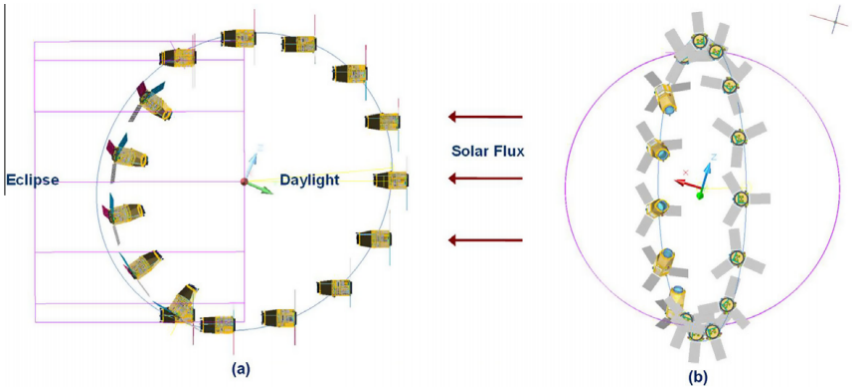

Figure A-1: Visualization of orbit from [37], shown from two viewing angles.

The temperature profile over a single orbit in quasi-steady state from the MATLAB model used in this thesis, and a corresponding Thermal Desktop model are shown in Figure A-2a and are in close agreement. The results from [37] are shown in Figure A-2b. The temperatures from the MATLAB model and the results from [37] also match well. Note, for simplicity, the facesheets are modeled as thermally coupled surfaces, so the thermal gradient through the thickness in the sun is not modeled.

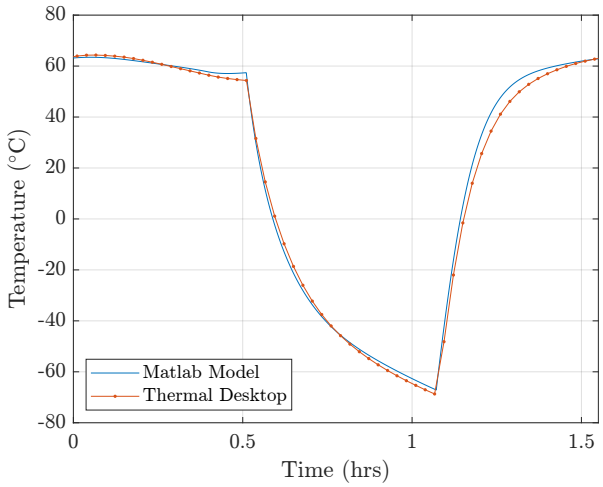

(a) The MATLAB model used in this thesis and a Thermal Desktop model for over one orbit in quasi-steady state.

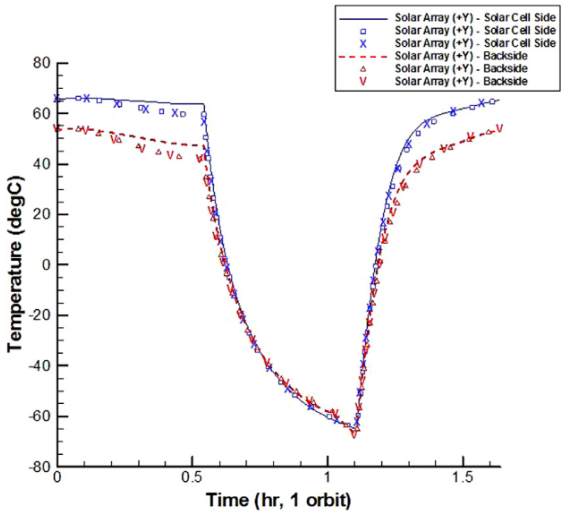

(b) The results from [37] showing the solar array temperatures over one orbit

Figure A-2: A comparison of the modeled results against the literature results. Models are in close agreement.

A.2 Modeling a Silicon Wafer in LEO

The second validation scenario is that of a 4-inch nadir-facing silicon wafer in LEO as modeled in [39]. The modeling scenario is similar to that of WaferSat (with the exception of the diameter). A summary of the relevant modeling parameters is shown in Table A.2.

Table A.2: Summary of parameters for solar array thermal modeling from [39]

Model Parameter	**Symbol**	**Value**	**Units**
solar beta angle	β	0	$^\circ$
solar array efficiency	η_{SA}	0.18	-
zenith side mean absorptivity	α_{SA}	0.8	-
zenith side mean emissivity	ε_{SA}	0.8	-
nadir side mean absorptivity	α_b	0.39	-
nadir side mean emissivity	ε_b	0.88	-
Earth albedo	a_E	0.7	-
orbit altitude	h_o	500	km
Earth effective black body temperature	T_E	288	K
Temperature of free space	T_s	5	K
Black body temperature of sun	T_{sol}	5780	K
wafer diameter	d_{waf}	101.6	mm
wafer thickness	t_{waf}	2	mm

Modeled results from [39] are shown in Figure A-3b. Note that several power distribution schemes were presented; the constant power scheme was chosen for comparison. The corresponding results using the thesis MATLAB model and Thermal Desktop models are shown in Figure A-3. The overall temperature profile is a close match, however, note that the MATLAB and Thermal Desktop models show the non monotonic heating and cooling due to nadir-side illumination. The results from [39] unexpectedly do not exhibit this, instead showing monotonic heating and cooling phases.

Analysis of the modeling of angles shows a modeling error in θ_2, the angle before the wafer enters eclipse shown in Figure A-4 b.

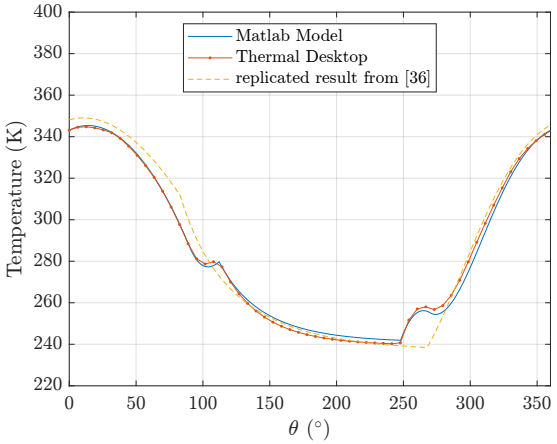

(a) Thesis MATLAB model, Thermal Desktop model, and a replicated result over one orbit in quasi-steady state.

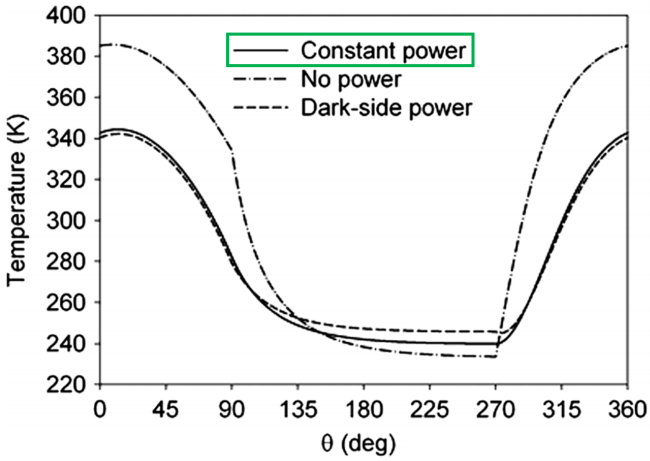

(b) Result from [39]. Constant power case is compared (solid line).

Figure A-3: Comparison of thesis MATLAB model to Thermal Desktop and results of 4 inch Si wafer in LEO from [39]

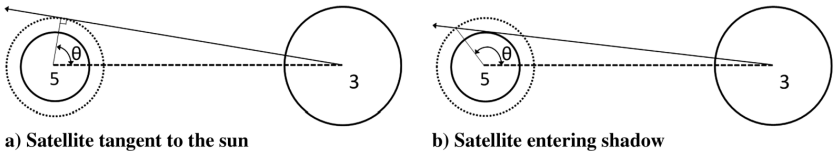

Figure A-4: Angles defining satellite tangency and start of eclipse from [39]

With angle definitions:

$$\theta_1 = \arccos\left(\frac{r_e + h}{b}\right) \tag{A.1}$$

$$\theta_2 = \arccos\left(\frac{r_e}{b}\right) \tag{A.2}$$

and nadir-side solar illumination from θ_1 to θ_2. θ_2 should be:

$$\theta_2 = \arccos\left(\frac{r_e}{b}\right) + \arccos\left(\frac{r_e}{r_e + h}\right) \tag{A.3}$$

This model with the error in θ_2 is reproduced in the dashed trace of Figure A-3a. The distinction in temperature ranges is small and the main difference is the loss of the nadir-side illumination heating transients. However, the result overall provides a good validation of the thesis MATLAB thermal model.

Appendix B

A Deep Space SmallSat

In this appendix, a series of approaches are proposed for the design of a SmallSat in deep space. This is a generalization away from strictly high $\mathcal{R}$ systems in LEO. In this scenario, the design difficulty is drawn not solely from the SWaP constraints, but from the challenge of the thermal environment far from the sun.

Consider a solar-powered 100 kg SmallSat that will travel beyond Earth orbit. Traditionally, the distance to Jupiter ($\sim$ 5.2 AU) serves as the boundary beyond which solar arrays are insufficient to power a spacecraft. Beyond Jupiter, deep space satellites have used radioisotope thermoelectric generators which in addition to providing power, provide a large amount of heat. This is particularly advantageous as the power from the sun is inversely proportional to r^2.

B.1 $\mathcal{AR}$ Scaling Reprise

B.1.1 Thermal Optimality Further from the Sun

In recent years, there has been particular interest in exploring Enceladus, an icy moon of Saturn. The 2022 Planetary Science and Astrobiology Decadal Survey has highlighted Enceladus as a valuable target for exploration for the search for potential life [110]. In this section, a 100 kg Disk-shaped SmallSat will be considered near Enceladus at a distance of 9.5 AU from the sun.

The power output from the sun decreases according to:

$$E_o = E_E \frac{r_E^2}{r_o^2} \tag{B.1}$$

where E_E is the solar flux at mean Earth orbit distance to the sun, r_E and r_o refers to the deep space distance to the sun. As such, the solar power flux at 9.5 AU is a little more than 1% of that at Earth orbit. This creates a particular challenge for any solar powered spacecraft in terms of power generation as well as thermal survival.

As the SmallSat moves further and further from the sun, the amount of heat variability will decrease; this can be approximated as near steady state temperature conditions regardless of the mass of the spacecraft. Consider again variation of $\mathcal{AR}$ for a constant mass, constant volume system. As disk radius increases, thickness increases, and $\mathcal{AR}$ increases. As the disk radius increases, the solar collection area also increases, increasing heating from the only heat source - as small as it may be. To maximize solar heating and minimize thermal radiation losses, it will be assumed that the disk is coated with TiNOX thermal coating with $\varepsilon = 0.05$, $\alpha = 0.90$. It will also be assumed that one flat face surface normal will always be sun-facing.

The estimated steady state temperatures for various disk radii at 9.5 AU are shown in Figure B-1. Notably, as the radius and $\mathcal{AR}$ increase, the steady state temperatures

increase monotonically, suggesting that a solar absorber may be helpful for survival. However, the temperatures seem to asymptotically converge on approximately $-50°$ C, far below the estimated operable range for batteries (but note that solar array area has not been considered yet - the system is currently purely a TiNOX absorber). Analysis of the contributions of cylinder side walls and flat faces to the total surface

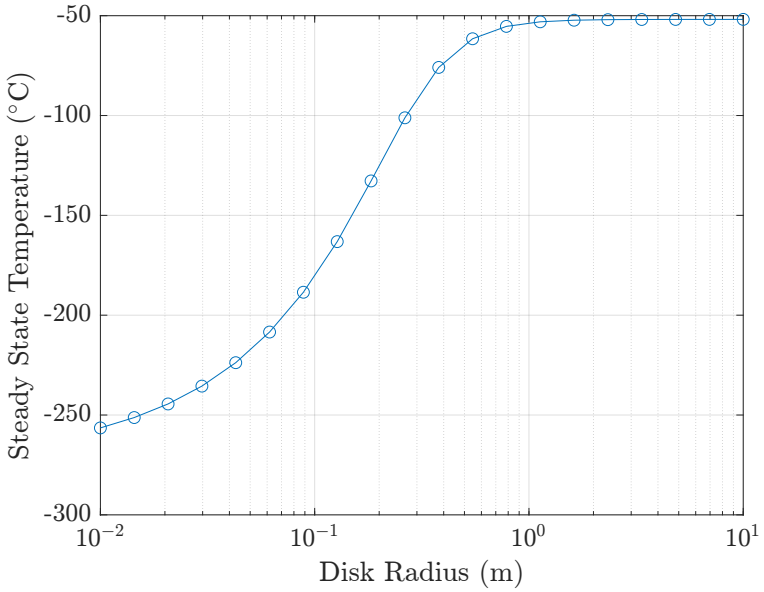

Figure B-1: Steady State temperatures at 9.5 AU vs. disk radius for a fixed volume system.

area help explain the increase in steady state temperature with $Æ$. At low $Æ$ (a thin rod), the side walls dominate the area. Since the axis is aligned with the solar flux, the side walls radiate, but do not absorb sunlight. When $Æ$ is high, and the flat surfaces dominate the surface area, the maximal amount of surface points to the sun, resulting in greater collection of heat from sunlight. This is further shown in Figure B-3 which shows the heat flow conditions at steady state for each disk radius. Solid lines represent absorbed heat and dashed lines represent radiated heat. At low $Æ$, there is limited solar heating and the temperature is governed by large side wall area. At high $Æ$ the solar heat absorption is high, and thermal radiation is dominantly from the flat surfaces. Since these are steady state temperatures, the sum of absorbed heats and radiated heats are equal. High $Æ$ systems at steady state can

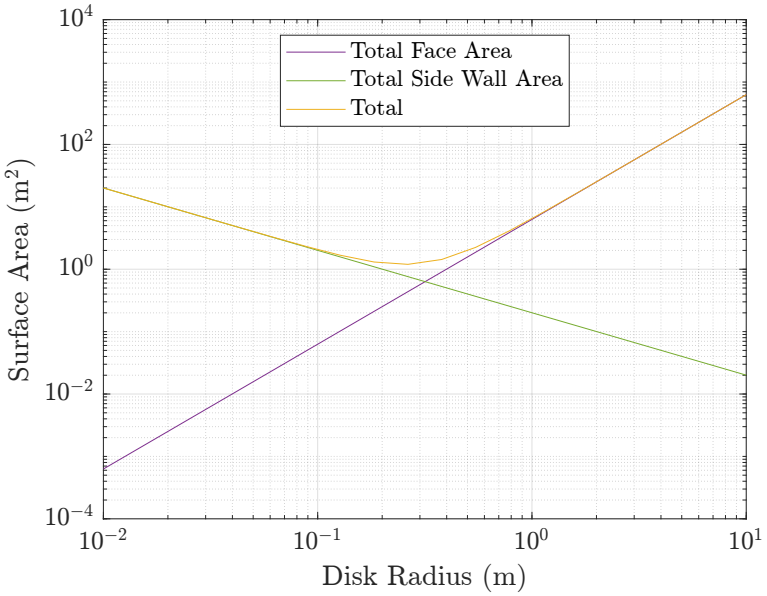

Figure B-2: Surface areas: total surface area and relative contributions of face areas and side wall area

be said to be greater in flux (balanced positive and negative) than low $\mathcal{R}$ systems. There are several regions of Figure B-3. In region a, the radiation is dominated by side walls:

$$S_T \approx S_w \propto r^{-1} \tag{B.2}$$

$$P_{radT} \approx \sigma \varepsilon S_T T_{SS}^4 \propto r^2 \tag{B.3}$$

In region b, there is a combination of contribution of side walls and surfaces to the heat radiation. Is surface area normal to the sun increases, so does the net heat absorbed.

$$S_T \propto r^n \tag{B.4}$$

$$-1 < n < 2 \tag{B.5}$$

In region c, there is asymptotic convergence where the two flat surfaces each account for half of the heat rejection of the system, but solar heating is maximized. The steady state temperatures continue to increase as the heat absorbed increases. In the

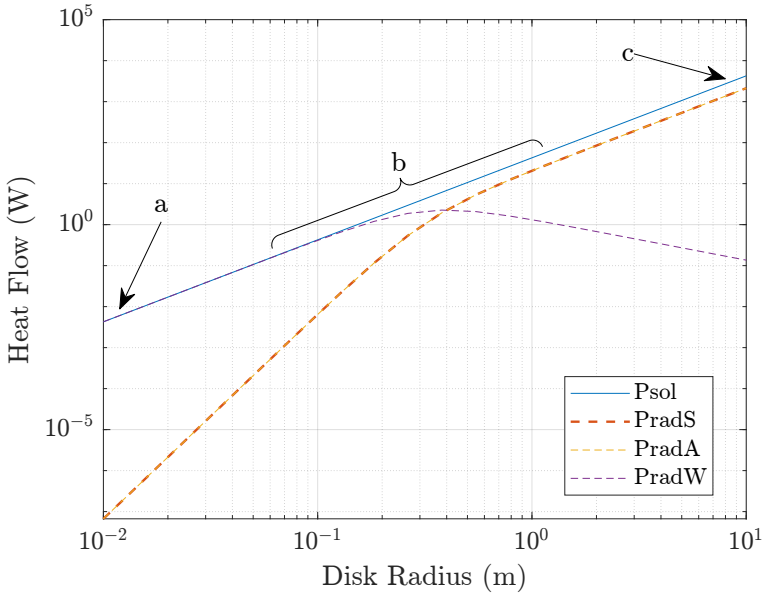

Figure B-3: Heat Flows vs. disk radius. Solid line represents absorbed heats, dashed lines represent radiation.

limit as $\mathcal{R} \to \infty$, the steady state temperature will be at a maximum (and this will approximate a Dyson Sphere at a distance of 9.5 AU). Note however, that the system will nearly converge on the steady state maximum at a radius of 10 m.

$$S_T \approx (S_W + S_A) \propto r^2 \tag{B.6}$$

$$P_{radT} \propto r^2 \tag{B.7}$$

B.1.2 Power Optimality Further from the Sun

In the previous example, it was assumed that the the surface of a disk was only a TiNOX-coated surface with no solar array, and thus no power generation (without an RTG). If some solar array fill factor is assumed, then electrical power will be available (at the expense of increased net emissivities). In the previous example, the SmallSat was assumed to be at a distance of 9.5 AU from the sun with no other bodies nearby. It was observed that the best case steady state temperatures were too low for survival. In this example, a modifying assumption is made to include Encleadus at a distance

of 100 km. The high mean bond albedo of 0.85 will provide an addition source of heating on the backside of the disk.

Contours of mean electrical power for SA physical fill factor on the x axis and the increasing disk radius on the y axis in Figure B-4a. Notably, as $\mathcal{AR}$ is increased and SA fill factor are increased, so too does power. Contours of the steady state temperatures over SA fill factor and disk radius are shown in Figure B-4b. The warmest conditions are present when disk radius is maximized and SA fill factor is reduced (due to the high emissivity of SA coverglass). Note that some technologies exist that could aid in reducing the emissivity of coverglass which could reduce this issue [111, 112]. The

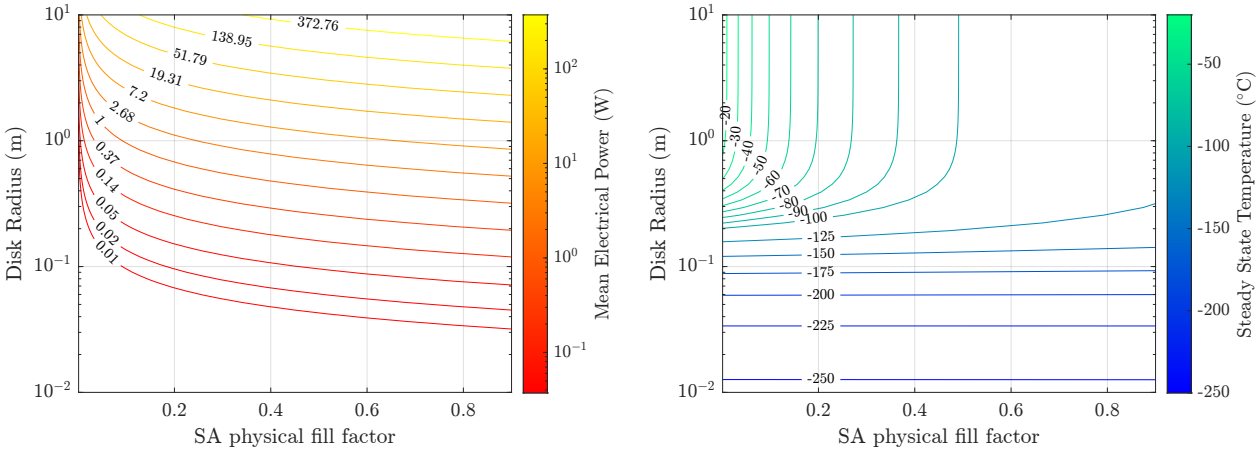

(a) Contours of mean electrical power for disk radius and solar array physical fill factor

(b) Contours of steady state temperature for disk radius and solar array physical fill factor (including corresponding mean electrical power dissipation as heat)

Figure B-4: Mean electrical power contours and steady state temperatures for scaling of disk with various solar array fill factors

same data from Figure B-4 can be plotted as Pareto fronts to show the maximum power capability vs steady state temperatures for several given disk radii. The results for 7 radii are shown in Figure B-5. Note that there is a diminishing return for steady state temperature above a radius of about 2 m. However, increases to $\mathcal{AR}$ beyond that have the benefit of greater mean power capabilities for small steady state temperature decrease.

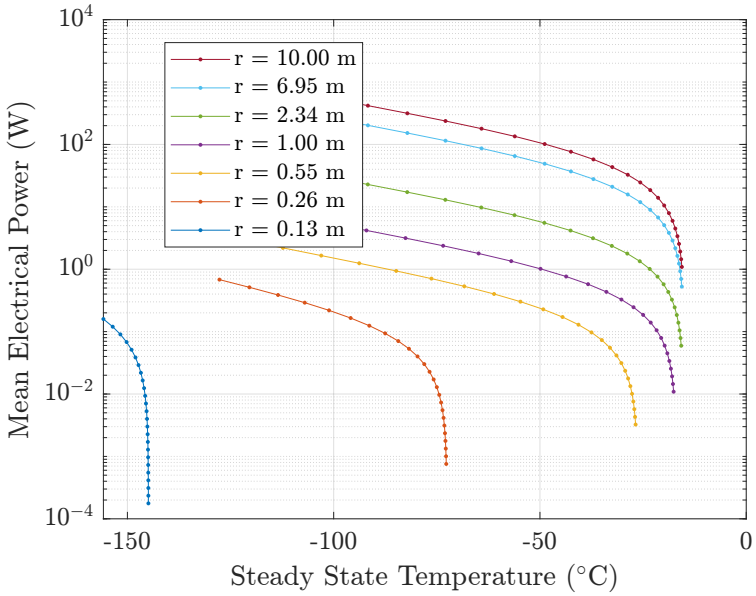

Figure B-5: Pareto fronts of electrical power capability vs. steady state temperature for several disk radii

B.2 Thermally Adapting in Deep Space

Although the thermal extremes tend towards a cold state, thermal adaptability may be of use in deep space missions. Several examples are explored a high-level.

B.2.1 Thermal Variability on a Schedule: Inner vs. Outer Cruise

One scenario where adaptability may be of particular use is for spacecraft that encounter widely variable distances from the sun. Deep space missions often must perform inner cruises to perform flyby maneuvers to reach deep space destinations. As such, they may have need of thermal design for rejection of high heat flows near the sun as well as adaptability for the cold of deep space at the final destination.

Another example might be a mission in a highly elliptical orbit, such as the Ulysses spacecraft [113]. The Ulysses spacecraft varied from a perihelion of $\sim$ 1 AU and

aphelion of $\sim$ 5.2 AU. The thermal system of the Ulysses spacecraft was partially adaptive. It was powered with an RTG, providing an excess of heat and power for survival in deep space. When nearer to the sun, internal power dissipation was diverted to resistors on thermal radiators to reject heat from the system.

If we once again consider the disk SmallSat, survival with solar panels only may be possible in an adaptive configuration. Consider a 1-meter disk radius system with one flat surface normal always sun-facing. The sun-facing and anti sun-facing surfaces can be adaptively tailored to include electrochromic area: $f_e^s = 0.27$, $f_e^s = 0.12$. Additionally, if an ADCS system is included, it will be assumed that the disk can roll away from the sun, to present a lower angle.

Results of an adaptively tailored system are shown in Figure B-6. Steady state temperatures are shown for various solar array physical fill factors. The orange lines represent steady state temperatures at 1 AU, tuned for the hot condition, and the blue line represents steady state temperatures at 5.2 AU, tuned for the worst case cold condition. At 1 AU, the system increases electrochromic emissivity to maximize radiation out of the system and rolls through a large angle to minimally present area to the sun. At 5.2 AU, the system is normal to the sun and with the lowest electrochromic emissivity possible. Note that in this design, it is not desirable to maximize the electrochromic emissivity since the minimum attainable of 0.2 is actually quite high when in deep space. Therefore the dynamic behavior is balanced against the worst case cold and a compromise of small electrochromic areas is identified.

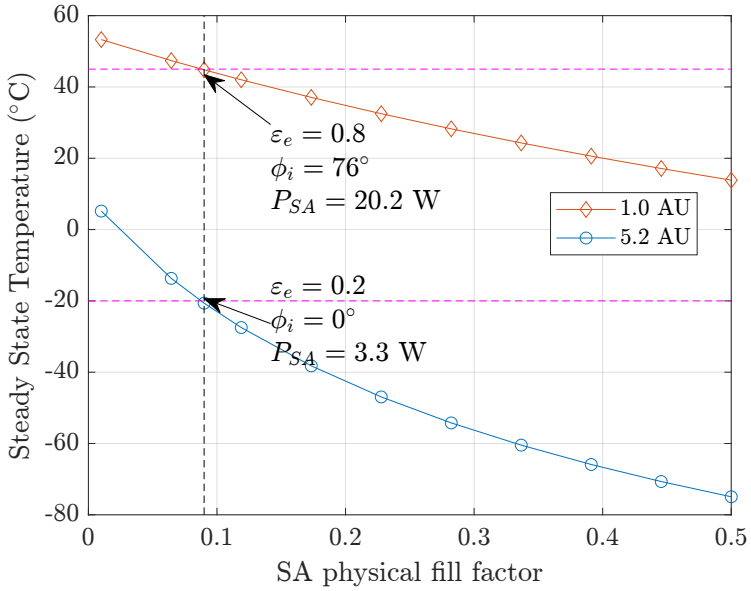

Figure B-6: 1-meter radius disk steady state temperature extremes at perihelion and aphelion with electrochromic and view factor adaptability

B.2.2 Thermal Spatial Zones

The high-level analysis of this appendix has focused on high $\mathcal{R}$, singular body systems. For practical reasons, deep space spacecraft, particularly those with large propellant tanks have deployed appendages and a low $\mathcal{R}$ main bus. This presents opportunities for thermal zoning. For an assumed bus size, using the BCT X-Sat[1] with total surface area of 3.6 meter^2. The steady state temperatures near Enceladus can be approximated as a function of heat capture rate as shown in Figure B-7. The heat capture rate on the x axis estimates the amount of internal power dissipation that is captured as heat. For systems that are better coupled (allowing for heat capture of more internal power dissipation) less internal power is required to maintain a given bus temperature requirement (example in Figure B-7 of $-15°$ C). High volume systems may allow for creation of specific thermal zones, insulated and isolated near the interior of the spacecraft. As an example, a propellant tank near the center of the

[1] https://www.bluecanyontech.com/static/datasheet/BCT_DataSheet_Spacecraft_Microsat.pdf

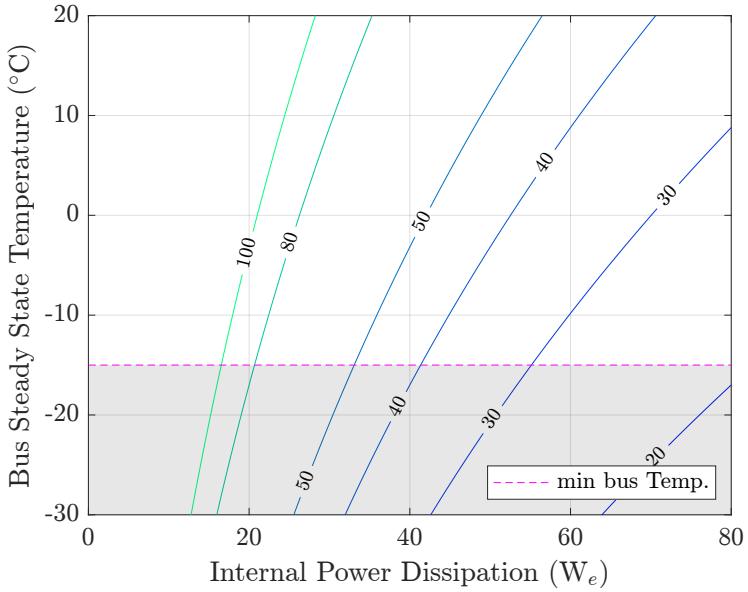

Figure B-7: Bus steady state temperature for given internal power dissipation and contours of percent internal heat capture rate.

spacecraft volume may need to be heated above the bus temperature requirement for operation. For a partially thermally isolated system, the tank temperatures can be expressed as a function of internal local heating powers as shown in Figure B-8. For an assumed propellant density, LMP-103S, the contours show the allowable propellant masses (and associated assumed spherical tank mass and surface area). As the tank increases in size, more local heating is required due to the increase in surface area. This heating could be achieved with dynamic coupling to other internal power dissipating elements in the spacecraft (perhaps a more efficient, adaptive system) or dedicated ohmic heating.

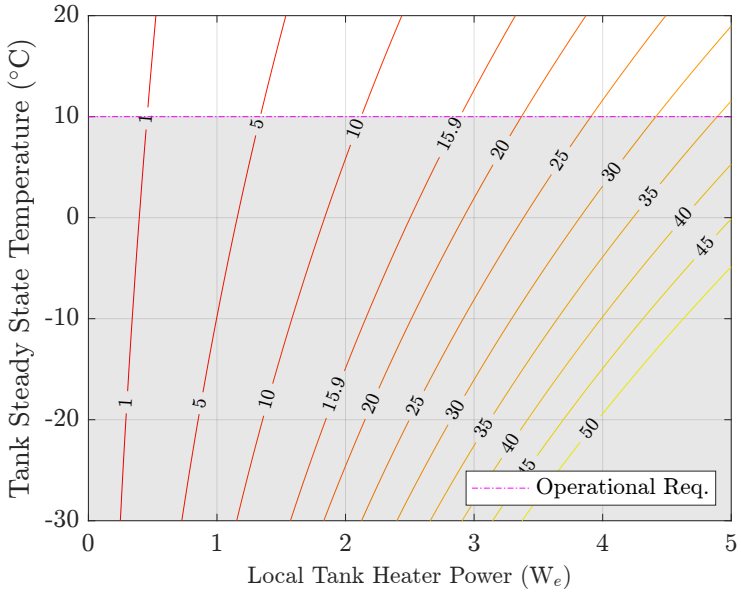

Figure B-8: Propellant tank steady state temperature for local heater power with contours of tank size (propellant mass in kg)

B.2.3 Power Modes and Mission Sequencing

Finally, in addition to spatial separation of the system, it is possible to devise mission sequences and specifically power dissipative modes to provide adaptive behavior for the system. In particular, mission requirements may drive power mode sequences that vary in time, changing the internal heat dissipation. A system that provides for some operational adaptability either in selective coupling/decoupling [82] and heat recapture with varied internal power dissipation levels could increase thermal survivability. Much more work is needed as this will require modeling of many more coupled spacecraft subsystems. Application of responsiveness and adaptability to larger systems allows for many more complex avenues for analysis and the potential to increase operability under varied conditions whilst maintaining performance optimality.

Bibliography

[1] Rioux, N., "ANSI/AIAA guide for estimating spacecraft systems contingencies applied to the NASA GLAST mission," *2006 IEEE Aerospace Conference*, IEEE, 2006, pp. 17–pp.

[2] Thunnissen, D. P., "Method for determining margins in conceptual design," *Journal of spacecraft and rockets*, Vol. 41, No. 1, 2004, pp. 85–92.

[3] Feynman, R. P., "Plenty of Room at the Bottom," 1959.

[4] Gomes, W., Khushu, S., Ingerly, D. B., Stover, P. N., Chowdhury, N. I., O'Mahony, F., Balankutty, A., Dolev, N., Dixon, M. G., Jiang, L., et al., "8.1 Lakefield and Mobility Compute: A 3D Stacked 10nm and 22FFL Hybrid Processor System in 12× 12mm 2, 1mm Package-on-Package," *2020 IEEE International Solid-State Circuits Conference-(ISSCC)*, IEEE, 2020, pp. 144–146.

[5] Polat, H. C., Virgili-Llop, J., and Romano, M., "Survey, statistical analysis and classification of launched cubesat missions with emphasis on the attitude control method," *Journal of small satellites*, Vol. 5, No. 3, 2016, pp. 513–530.

[6] Schoolcraft, J., Klesh, A., and Werne, T., "MarCO: interplanetary mission development on a CubeSat scale," *Space Operations: Contributions from the Global Community*, Springer, 2017, pp. 221–231.

[7] Judy, J. W., "Microelectromechanical systems (MEMS): fabrication, design and applications," *Smart materials and Structures*, Vol. 10, No. 6, 2001, pp. 1115.

[8] Nieto-Peroy, C. and Emami, M. R., "Cubesat mission: from design to operation," *Applied Sciences*, Vol. 9, No. 15, 2019, pp. 3110.

[9] Shea, H., "MEMS for pico-to micro-satellites," *Moems And Miniaturized Systems Viii*, Vol. 7208, International Society for Optics and Photonics, 2009, p. 72080M.

[10] Hadaegh, F. Y., Chung, S.-J., and Manohara, H. M., "On development of 100-gram-class spacecraft for swarm applications," *IEEE Systems Journal*, Vol. 10, No. 2, 2014, pp. 673–684.

[11] Barnhart, D. J., Vladimirova, T., and Sweeting, M. N., "Satellite miniaturization techniques for space sensor networks," *Journal of Spacecraft and Rockets*, Vol. 46, No. 2, 2009, pp. 469–472.

[12] Chung, S.-J. and Hadaegh, F., "Swarms of femtosats for synthetic aperture applications," 2011.

[13] Kovács, R. and Józsa, V., "Thermal analysis of the SMOG-1 PocketQube satellite," *Applied Thermal Engineering*, Vol. 139, 2018, pp. 506–513.

[14] Welle, R., Venturini, C., Hinkley, D., and Gangestad, J., "The DiskSat: A Two-Dimensional Containerized Satellite," 2021.

[15] Irie, T., Yamada, G., and Aomura, S., "Natural frequencies of Mindlin circular plates," 1980.

[16] White, C., Colombo, C., Scanlon, T. J., McInnes, C. R., and Reese, J. M., "Rarefied gas effects on the aerodynamics of high area-to-mass ratio spacecraft in orbit," *Advances in Space Research*, Vol. 51, No. 11, 2013, pp. 2112–2124.

[17] Niccolai, L., Bassetto, M., Quarta, A. A., and Mengali, G., "A review of Smart Dust architecture, dynamics, and mission applications," *Progress in Aerospace Sciences*, Vol. 106, 2019, pp. 1–14.

[18] Senge, R., Bösner, S., Dembczyński, K., Haasenritter, J., Hirsch, O., Donner-Banzhoff, N., and Hüllermeier, E., "Reliable classification: Learning classifiers that distinguish aleatoric and epistemic uncertainty," *Information Sciences*, Vol. 255, 2014, pp. 16–29.

[19] Uebelhart, S. A., *Non-deterministic design and analysis of parameterized optical structures during conceptual design*, Ph.D. thesis, Massachusetts Institute of Technology, 2006.

[20] Lowey, C. E., *Uncertainty-Based Design Optimization and Decision Options for Responsive Maneuvering of Reconfigurable Satellite Constellations*, Ph.D. thesis, Massachusetts Institute of Technology, 2022.

[21] Bertsimas, D. and Sim, M., "The price of robustness," *Operations research*, Vol. 52, No. 1, 2004, pp. 35–53.

[22] Puig-Suari, J., Turner, C., and Ahlgren, W., "Development of the standard CubeSat deployer and a CubeSat class PicoSatellite," *2001 IEEE aerospace conference proceedings (cat. No. 01TH8542)*, Vol. 1, IEEE, 2001, pp. 1–347.

[23] Janson, S. W., Helvajian, H., Hansen, W. W., and Lodmell, J., "Microthrusters for nanosatellites," *Second International Conference on Integrated Micro Nanotechnology for Space Applications*, 1999, pp. 1–17.

[24] Janson, S., Helvajian, H., Amimoto, S., Smit, G., Mayer, D., and Feuerstein, S., "Microtechnology for space systems," *1998 IEEE Aerospace Conference Proceedings (Cat. No. 98TH8339)*, Vol. 1, IEEE, 1998, pp. 409–418.

[25] Helvajian, H., Janson, S. W., and Robinson, E., "Big benefits from tiny technologies: Micro-nanotechnology applications in future space systems," *Advancement of Photonics for Space: A Critical Review*, Vol. 10288, International Society for Optics and Photonics, 1997, p. 1028802.

[26] Barnhart, D. J., Vladimirova, T., and Sweeting, M. N., "Satellite-on-a-Chip development for future distributed space missions," Vol. 42541, 2006, pp. 199–212.

[27] Barnhart, D. J., Vladimirova, T., and Sweeting, M. N., "Very-small-satellite design for distributed space missions," *Journal of Spacecraft and Rockets*, Vol. 44, No. 6, 2007, pp. 1294–1306.

[28] Cutler, J. and Hutchins, G., "OPAL: Smaller, simpler, and just plain luckier," 2000.

[29] Heidt, H., Puig-Suari, J., Moore, A., Nakasuka, S., and Twiggs, R., "CubeSat: A new generation of picosatellite for education and industry low-cost space experimentation," 2000.

[30] Pianka, E. R., "On r-and K-selection," *The american naturalist*, Vol. 104, No. 940, 1970, pp. 592–597.

[31] Hunter Adams, V. and Peck, M., "R-selected spacecraft," *Journal of Spacecraft and Rockets*, Vol. 57, No. 1, 2020, pp. 90–98.

[32] Manchester, Z., Peck, M., and Filo, A., "Kicksat: A crowd-funded mission to demonstrate the world's smallest spacecraft," 2013.

[33] Estevez, D., "Detecting the Sprites from KickSat-2," `https://destevez.net/2019/04/detecting-the-sprites-from-kicksat-2/`.

[34] Brashearsa, T., Lubina, P., Ruperta, N., Stantonb, E., Mehtaa, A., Knowlesa, P., and Hughesc, G. B., "Building the future of wafersat spacecraft for relativistic flight," *Proc. of SPIE Vol*, Vol. 9981, pp. 998104–1.

[35] Brashears, T., Lubin, P., Hughes, G. B., McDonough, K., Arias, S., Lang, A., Motta, C., Meinhold, P., Batliner, P., Griswold, J., et al., "Directed energy interstellar propulsion of wafersats," *Nanophotonics and Macrophotonics for Space Environments IX*, Vol. 9616, International Society for Optics and Photonics, 2015, p. 961609.

[36] Hein, A. M., Burkhardt, Z., and Eubanks, T. M., "AttoSats: ChipSats, other Gram-Scale Spacecraft, and Beyond," *arXiv preprint arXiv:1910.12559*, 2019.

[37] Kim, H. K. and Han, C. Y., "Analytical and numerical approaches of a solar array thermal analysis in a low-earth orbit satellite," *Advances in Space Research*, Vol. 46, No. 11, 2010, pp. 1427–1439.

[38] Adams, V. H., "Theory and Applications of Gram-Scale Spacecraft," 2020.

[39] Bruno, A., Maghsoudi, E., and Martin, M. J., "Simulation of Heat Transfer in Wafer-Integrated Femtosatellites," *Journal of Spacecraft and Rockets*, Vol. 51, No. 2, 2014, pp. 627–631.

[40] Stout, K. D., *Design optimization of thermal paths in spacecraft systems*, Ph.D. thesis, Massachusetts Institute of Technology, 2013.

[41] Archer, G., Saltelli, A., and Sobol, I., "Sensitivity measures, ANOVA-like techniques and the use of bootstrap," *Journal of Statistical Computation and Simulation*, Vol. 58, No. 2, 1997, pp. 99–120.

[42] Eckert, C., Clarkson, P. J., and Zanker, W., "Change and customisation in complex engineering domains," *Research in engineering design*, Vol. 15, No. 1, 2004, pp. 1–21.

[43] Gross, J. and Rudolph, S., "Rule-based spacecraft design space exploration and sensitivity analysis," *Aerospace Science and Technology*, Vol. 59, 2016, pp. 162–171.

[44] Larson, W. J., Wertz, J. R., et al., *Space mission analysis and design*, Vol. 3, Springer, 1992.

[45] Hadigheh, A. G., Mirnia, K., and Terlaky, T., "Active constraint set invariancy sensitivity analysis in linear optimization," *Journal of optimization theory and applications*, Vol. 133, No. 3, 2007, pp. 303–315.

[46] Deb, K. and Gupta, H., "Introducing robustness in multiobjective optimization," *Evolutionary Computation Journal*, Vol. 14, No. 4, 2006, pp. 463–494.

[47] Kasprzyk, J. R., Nataraj, S., Reed, P. M., and Lempert, R. J., "Many objective robust decision making for complex environmental systems undergoing change," *Environmental Modelling & Software*, Vol. 42, 2013, pp. 55–71.

[48] Hadka, D., Herman, J., Reed, P., and Keller, K., "An open source framework for many-objective robust decision making," *Environmental Modelling & Software*, Vol. 74, 2015, pp. 114–129.

[49] Lempert, R., Popper, S., and Bankes, S., "New Methods for Quantitative, Long-Term Policy Analysis," *The RAND Pardee Center*.

[50] Walker, W. E., Lempert, R. J., and Kwakkel, J. H., "Deep uncertainty," *Delft University of Technology*, Vol. 1, No. 2, 2012.

[51] McPhail, C., Maier, H., Kwakkel, J., Giuliani, M., Castelletti, A., and Westra, S., "Robustness metrics: How are they calculated, when should they be used and why do they give different results?" *Earth's Future*, Vol. 6, No. 2, 2018, pp. 169–191.

[52] Quinn, J. D., Reed, P. M., Giuliani, M., and Castelletti, A., "Rival framings: A framework for discovering how problem formulation uncertainties shape risk management trade-offs in water resources systems," *Water Resources Research*, Vol. 53, No. 8, 2017, pp. 7208–7233.

[53] Guenov, M. D., Chen, X., Molina-Cristóbal, A., Riaz, A., van Heerden, A. S., and Padulo, M., "Margin allocation and tradeoff in complex systems design and optimization," *AIAA Journal*, Vol. 56, No. 7, 2018, pp. 2887–2902.

[54] Richard de Neufville, L., Scholtes, S., and Wang, T., "Valuing Real Options by Spreadsheet: Parking Garage Case Example," *ASCE Journal of Infrastructure Systems*.

[55] Myers, S. C., "Finance theory and financial strategy," *Interfaces*, Vol. 14, No. 1, 1984, pp. 126–137.

[56] Wang, T. and De Neufville, R., "Real options "in" projects," *real options conference, Paris, France*, Citeseer, 2005.

[57] De Weck, O. L., De Neufville, R., and Chaize, M., "Staged deployment of communications satellite constellations in low earth orbit," *Journal of Aerospace Computing, Information, and Communication*, Vol. 1, No. 3, 2004, pp. 119–136.

[58] Masterson, R. A., *Dynamic tailoring and tuning for space-based precision optical structures*, Ph.D. thesis, Massachusetts Institute of Technology, 2005.

[59] Masterson, R. and Miller, D., "Dynamic tailoring and tuning of structurally connected TPF interferometer," *Modeling, Systems Engineering, and Project Management for Astronomy II*, Vol. 6271, International Society for Optics and Photonics, 2006, p. 62710U.

[60] de Weck, O., Miller, D., and Mosier, G., "Multivariable isoperformance methodology for precision opto-mechanical systems," *43rd AIAA/ASME/ASCE/AHS/ASC Structures, Structural Dynamics, and Materials Conference*, 2002, p. 1420.

[61] Masterson, R. and Miller, D., "Hardware Tuning for Dynamic Performance Through Isoperformance Tuning," *47th AIAA/ASME/ASCE/AHS/ASC Structures, Structural Dynamics, and Materials Conference 14th AIAA/ASME/AHS Adaptive Structures Conference 7th*, 2006, p. 2277.

[62] Bertsimas, D., Brown, D. B., and Caramanis, C., "Theory and applications of robust optimization," *SIAM review*, Vol. 53, No. 3, 2011, pp. 464–501.

[63] Rahal, S., Papageorgiou, D. J., and Li, Z., "Hybrid strategies using linear and piecewise-linear decision rules for multistage adaptive linear optimization," *European Journal of Operational Research*, Vol. 290, No. 3, 2021, pp. 1014–1030.

[64] Ochoa, H., Hua, J., Mastropietro, A. J., Lee, R., Paris, A., Emis, N., and Williams, B., "Design and Development of the Heat Redistribution System for the Europa Clipper Spacecraft," 47th International Conference on Environmental Systems, 2017.

[65] Hwangbo, H. and KELLY, W., "Transient response of thermal louvers with bimetallic actuators," *15th Thermophysics Conference*, 1980, p. 1539.

[66] Champion, J., Osiander, R., Darrin, M., and Swanson, T., "MEMS louvers for thermal control," 1998.

[67] Osiander, R., Champion, J., Darrin, A., Sniegowski, J., Rodgers, S., Douglas, D., and Swanson, T., "Micromachined louver arrays for spacecraft thermal control radiators," *39th Aerospace Sciences Meeting and Exhibit*, 2001, p. 215.

[68] Farrar, D., Douglas, D. M., Swanson, T., Collins, C., Darrin, A., and Osiander, R., "MEMS shutters for thermal control—Flight validation and lessons learned," *AIP Conference Proceedings*, Vol. 880, American Institute of Physics, 2007, pp. 73–80.

[69] Shimazaki, K., Tachikawa, S., Ohnishi, A., and Nagasaka, Y., "Design of thermal radiative properties of multilayer films on a variable emittance radiator," *SAE transactions*, 2001, pp. 106–114.

[70] Fan, D., Chen, C., Xiao, T., and Li, Q., "Flexible thermochromic foil derived from fine perovskite nanoparticles with excellent energy-saving performance," *International Journal of Energy Research*, Vol. 43, No. 9, 2019, pp. 4546–4553.

[71] Tachikawa, S., Ohnishi, A., Shimakawa, Y., Ochi, A., Okamoto, A., and Nakamura, Y., "Development of a variable emittance radiator based on a perovskite manganese oxide," *Journal of thermophysics and heat transfer*, Vol. 17, No. 2, 2003, pp. 264–268.

[72] Arbizzani, C., Mastragostino, M., and Zanelli, A., "Electrochromic devices: A comparison of several systems," *Solar energy materials and solar cells*, Vol. 39, No. 2-4, 1995, pp. 213–222.

[73] Demiryont, H., "Electrochromic heat modulator successfully tested in space," *SPIE Newsroom*, 2008.

[74] Paris, A. and Anderson, K., "Electrochromic radiators for microspacecraft thermal control," 2005.

[75] Demiryont, H., Shannon III, K. C., and Sheets, J., "Emissivity modulating electrochromic device," *Space Exploration Technologies II*, Vol. 7331, International Society for Optics and Photonics, 2009, p. 73310I.

[76] Demiryont, H., "Emissivity-modulating electrochromic device for satellite thermal control," *SPIE News-room, doi*, Vol. 10, No. 2.1200802, 2008, pp. 1011.

[77] Butcher, M., "Spacecraft thermal design: particular problems with small satellites," *Proceedings of the Institution of Mechanical Engineers, Part G: Journal of Aerospace Engineering*, Vol. 213, No. 4, 1999, pp. 245–253.

[78] Barth, A. L., Walker, A., Putman, P., and Ma, O., "Determining an Optimal Attitude Profile for Thermal Management of a Remote Sensing Cubesat," *ASCEND 2021*, 2021, p. 4101.

[79] Lyra, J. C. and Stultz, J. W., "The variable radioisotope heater unit for the Cassini spacecraft," *SAE transactions*, 1994, pp. 539–547.

[80] Hickey, G. S., Braun, D., Wen, L.-C., and Eisen, H. J., "Integrated lightweight structure and thermal insulation for Mars rover," *SAE transactions*, 1995, pp. 656–666.

[81] Hickey, G. S., Braun, D., Wen, L.-C., and Eisen, H. J., "Integrated thermal control and qualification of the Mars rover," *SAE transactions*, 1996, pp. 824–832.

[82] Bugby, D. C., Rivera, J. G., Mauro, S. L., and Farmer, J. T., "Extended Stroke and Miniaturized Reverse-Operation DTE Thermal Switches," 2021.

[83] Anderson, L., Kirk, M., Mattos, B., Swenson, C., Fish, C., Nunes, M., and Wright, R., "Active Thermal Control for the Multispectral Earth Sensors (ACMES) Mission," 2022.

[84] Anderson, L., Mork, J., Swenson, C., Zwolinski, B., Mastropietro, A., Sauder, J., McKinley, I., and Mok, M., "CubeSat active thermal control in support of advanced payloads: the active thermal architecture project," *CubeSats and SmallSats for Remote Sensing V*, Vol. 11832, SPIE, 2021, p. 1183203.

[85] De Weck, O. L. and Jones, M. B., "Isoperformance: Analysis and design of complex systems with desired outcomes," *Systems engineering*, Vol. 9, No. 1, 2006, pp. 45–61.

[86] Miki, M., Hiroyasu, T., and Ono, K., "Simulated annealing with advanced adaptive neighborhood," *Second international workshop on Intelligent systems design and application*, 2002, pp. 113–118.

[87] Marques, J., Cunha, M., and Savić, D. A., "Multi-objective optimization of water distribution systems based on a real options approach," *Environmental Modelling & Software*, Vol. 63, 2015, pp. 1–13.

[88] Dubey, R., *Performance Evaluation of a Lithium-Ion Pouch Battery Cell in Simulated Space Environment for a Pico-Satellite Concept (PicoSat)*, Master's thesis, Massachusetts Institute of Technology, 2022.

[89] Wertz, J. R., Everett, D. F., and Puschell, J. J., *Space mission engineering: the new SMAD*, Microcosm Press, 2018.

[90] Kreitinger, N. A., "Temperature Effects on Electrospray Performance," Tech. rep., AIR FORCE RESEARCH LAB EDWARDS AFB CA PROPULSION DIR/SPACE AND MISSILE ..., 2011.

[91] Martinez, I., "Radiative View Factors," `http://imartinez.etsiae.upm.es/~isidoro/tc3/Radiation%20View%20factors.pdf`, 2023.

[92] Howell, J. R., "A Catalog of Radiation Heat Transfer Configuration Factors," `http://www.thermalradiation.net/tablecon.html#B4`, 2022.

[93] Howell, J. R., Menguc, M. P., and Siegel, R., *Thermal Radiation Heat Transfer*, CRC Press, Taylor & Francis Group, 6th ed.

[94] Peyrou-Lauga, R., "Using real Earth albedo and Earth IR flux for spacecraft thermal analysis," 47th International Conference on Environmental Systems, 2017.

[95] Sun, W., Loeb, N. G., Davies, R., Loukachine, K., and Miller, W. F., "Comparison of MISR and CERES top-of-atmosphere albedo," *Geophysical research letters*, Vol. 33, No. 23, 2006.

[96] Barkstrom, B., Harrison, E., Smith, G., Green, R., Kibler, J., Cess, R., and Team, E. S., "Earth radiation budget experiment (ERBE) archival and April 1985 results," *Bulletin of the American Meteorological Society*, Vol. 70, No. 10, 1989, pp. 1254–1262.

[97] Hartmann, D., Ramanathan, V., Berroir, A., and Hunt, G., "Earth radiation budget data and climate research," *Reviews of Geophysics*, Vol. 24, No. 2, 1986, pp. 439–468.

[98] Stephens, G., Campbell, G., and Haar, T. V., "Earth radiation budgets," *Journal of Geophysical Research: Oceans*, Vol. 86, No. C10, 1981, pp. 9739–9760.

[99] Borreguero, A., Valverde, J., Rodríguez, J., Barber, A., Cubillo, J., and Carmona, M., "Synthesis and characterization of microcapsules containing Rubitherm® RT27 obtained by spray drying," *Chemical Engineering Journal*, Vol. 166, No. 1, 2011, pp. 384–390.

[100] Jamekhorshid, A., Sadrameli, S., and Farid, M., "A review of microencapsulation methods of phase change materials (PCMs) as a thermal energy storage (TES) medium," *Renewable and Sustainable Energy Reviews*, Vol. 31, 2014, pp. 531–542.

[101] Tyagi, V., Kaushik, S., Tyagi, S., and Akiyama, T., "Development of phase change materials based microencapsulated technology for buildings: a review," *Renewable and sustainable energy reviews*, Vol. 15, No. 2, 2011, pp. 1373–1391.

[102] Demiryont, H. and Moorehead, D., "Electrochromic emissivity modulator for spacecraft thermal management," *Solar Energy Materials and Solar Cells*, Vol. 93, No. 12, 2009, pp. 2075–2078.

[103] Letin, V., Kagan, M., Nadorov, V., and Zajavlin, V., "Bifacial solar arrays of Russian space crafts," *Conference Record of the Twenty-Eighth IEEE Photovoltaic Specialists Conference-2000 (Cat. No. 00CH37036)*, IEEE, 2000, pp. 1067–1070.

[104] Marion, B., "Measured and satellite-derived albedo data for estimating bifacial photovoltaic system performance," *Solar Energy*, Vol. 215, 2021, pp. 321–327.

[105] Landis, G. A., "Reinventing the solar power satellite," *53rd International Astronautical Congress*, No. IAC-02-R. 1.07, 2004.

[106] Delleur, A. M. and Kerslake, T. W., "Electrical performance of the international space station US photovoltaic array during bifacial illumination," *IECEC'02. 2002 37th Intersociety Energy Conversion Engineering Conference, 2002.*, IEEE, 2002, pp. 39–44.

[107] Welle, R., Venturini, C., Hinkley, D., Gangestad, J., Grasso, S., Muszynski, A., Hunter, R., Frost, C., Mayer, D., and Baker, C., "DiskSat: Demonstration Mission for a Two-Dimensional Satellite Architecture," 2022.

[108] AerospaceCorporation, "DiskSat: A New Form Factor for Small Satellites," `https://aerospace.org/fact-sheet/disksat-new-form-factor-small-satellites`.

[109] Cohen, B. S., March, A. I., Willcox, K. E., and Miller, D. W., "A level set-based topology optimization approach for thermally radiating structures," *Structural and Multidisciplinary Optimization*, Vol. 65, No. 6, 2022, pp. 167.

[110] National Academies of Sciences, E., Medicine, et al., "Origins, Worlds, and Life: A Decadal Strategy for Planetary Science and Astrobiology 2023-2032," 2022.

[111] Hamberg, I., Hjortsberg, A., and Granqvist, C., "High quality transparent heat reflectors of reactively evaporated indium tin oxide," *Applied Physics Letters*, Vol. 40, No. 5, 1982, pp. 362–364.

[112] Alonso-Álvarez, D., Llin, L. F., Mellor, A., Paul, D. J., and Ekins-Daukes, N. J., "ITO and AZO films for low emissivity coatings in hybrid photovoltaic-thermal applications," *Solar Energy*, Vol. 155, 2017, pp. 82–92.

[113] Wenzel, K., Marsden, R., Page, D., and Smith, E., "The ULYSSES mission," *Astronomy and astrophysics supplement series*, Vol. 92, 1992, pp. 207.

[114] Smith, K., "Advantages of Modularity and Commonality in a Spacecraft Architecture," *Earth & Space 2006: Engineering, Construction, and Operations in Challenging Environment*, 2006, pp. 1–6.

[115] Yendler, B., Meginnis, A., and Reif, A., "Thermal Management for High Power Cubesats," 2020.

[116] Masterson, R. and Miller, D., "Dynamic tailoring and tuning for precision optical space structures," *45th AIAA/ASME/ASCE/AHS/ASC Structures, Structural Dynamics & Materials Conference*, 2004, p. 1600.

[117] Marques, J., Cunha, M., and Savić, D., "Using real options in the optimal design of water distribution networks," *Journal of Water Resources Planning and Management*, Vol. 141, No. 2, 2015, pp. 04014052.

[118] Balling, R. J. and Sobieszczanski-Sobieski, J., "Optimization of coupled systems-a critical overview of approaches," *AIAA journal*, Vol. 34, No. 1, 1996, pp. 6–17.

[119] Pasqual, M. C. and de Weck, O. L., "Multilayer network model for analysis and management of change propagation," *Research in Engineering Design*, Vol. 23, No. 4, 2012, pp. 305–328.

[120] Janson, S. W., "Aerospace applications of MEMS," *MEMS/MOEMS Components and Their Applications II*, Vol. 5717, International Society for Optics and Photonics, 2005, pp. 1–13.

[121] Anderson, K., Zay, B., McQueeney, T., and Chandrasekher, P., "Electrochromic radiators for microspacecraft thermal control," 2005.

[122] Fan, D., Li, Q., and Xuan, Y., "Tailoring the solar absorptivity of thermochromic material La0. 7Ca0. 2Sr0. 1MnO3," *Journal of Quantitative Spectroscopy and Radiative Transfer*, Vol. 112, No. 18, 2011, pp. 2794–2800.

[123] de Weck, O., Agte, J., Sobieszczanski-Sobieski, J., Arendsen, P., Morris, A., and Spieck, M., "State-of-the-art and future trends in multidisciplinary design optimization," *48th Aiaa/Asme/Asce/Ahs/Asc Structures, Structural Dynamics, and Materials Conference*, 2007, p. 1905.

[124] Nakamura, Y. and Okamoto, A., "ln-Orbit Thermal Performance of a Smart Radiation Device," 2007.

[125] Birur, G. C., Siebes, G., Swanson, T. D., and Powers, E. I., "Spacecraft thermal control," 2001.

[126] Givargis, T. and Vahid, F., "Platune: A tuning framework for system-on-a-chip platforms," *IEEE Transactions on Computer-Aided Design of Integrated Circuits and Systems*, Vol. 21, No. 11, 2002, pp. 1317–1327.

[127] Gillette, R., "Selectively emissive materials for solar heat absorbers," *Solar Energy*, Vol. 4, No. 4, 1960, pp. 24–32.

[128] Frink, M. E., Jarecke, P. J., Folkman, M. A., and Wright Jr, R. E., "Far-IR spectral response measurements of the Clouds and the Earth's Radiant Energy System (CERES) sensors using a Fourier transform spectrometer and pyro-electric reference detector," *Sensor Systems for the Early Earth Observing System Platforms*, Vol. 1939, SPIE, 1993, pp. 82–91.

[129] Ben-Tal, A., El Ghaoui, L., and Nemirovski, A., *Robust optimization*, Vol. 28, Princeton university press, 2009.

[130] Yiyi, H., Taylor, P. C., Rose, F. G., Rutan, D. A., Shupe, M. D., Webster, M. A., and Smith, M. M., "Toward a more realistic representation of surface albedo in NASA CERES-derived surface radiative fluxes," *Elementa*, Vol. 10, No. 1, 2022.

[131] Corrado, M. N., *Active Thermal Augmentation and Ultra Dense MEMS-Based Electrospray Thrusters*, Ph.D. thesis, Massachusetts Institute of Technology, 2022.

[132] Siegel, N. W., *Silicon wafer integration of ion electrospray thrusters*, Ph.D. thesis, Massachusetts Institute of Technology, 2020.

[133] Rawal, S. P., Barnett, D. M., and Martin, D. E., "Thermal management for multifunctional structures," *IEEE transactions on Advanced Packaging*, Vol. 22, No. 3, 1999, pp. 379–383.

[134] Crisp, D., Pollock, H. R., Rosenberg, R., Chapsky, L., Lee, R. A., Oyafuso, F. A., Frankenberg, C., O'Dell, C. W., Bruegge, C. J., Doran, G. B., et al., "The on-orbit performance of the Orbiting Carbon Observatory-2 (OCO-2) instrument and its radiometrically calibrated products," *Atmospheric Measurement Techniques*, Vol. 10, No. 1, 2017, pp. 59–81.

[135] Anderson, L., Swenson, C., Davidson, R., Mastropietro, A. J., Maghsoudi, E., Luong, S., Cappucci, S., and Mckinley, I., "CubeSat active thermal management in support of cooled electro-optical instrumentation for advanced atmospheric observing missions," *CubeSats and NanoSats for Remote Sensing II*, Vol. 10769, SPIE, 2018, pp. 49–63.

[136] Karpati, G., Hyde, T., Peabody, H., and Garrison, M., "Resource management and contingencies in aerospace concurrent engineering," *AIAA SPACE 2012 conference & exposition*, 2012, p. 5273.

[137] Lempert, R. J., "Shaping the next one hundred years: new methods for quantitative, long-term policy analysis," 2003.

This page intentionally left blank.